



Universität Hamburg
Fakultät für Mathematik,
Informatik und Naturwissenschaften
Fachbereich Physik



Control of airborne nanoparticles

Dissertation
zur Erlangung des Doktorgrades
an der Fakultät für Mathematik, Informatik und
Naturwissenschaften
Fachbereich Physik
der Universität Hamburg

vorgelegt von
Nils Roth

Hamburg
2020

Gutachter der Dissertation:

Prof. Dr. Jochen Küpper
Dr. Daniel Horke

Zusammensetzung der Prüfungskommission:

Prof. Dr. Jochen Küpper
Dr. Daniel Horke
Prof. Dr. Henry Chapman
Prof. Dr. Henning Moritz
Prof. Dr. Daniela Pfannkuche

Vorsitzende/r der Prüfungskommission:

Prof. Dr. Daniela Pfannkuche

Datum der Disputation:

25.09.2020

Vorsitzender Fach-Promotionsausschusses PHYSIK:

Prof. Dr. Günter Hans Walter Sigl

Leiter des Fachbereichs PHYSIK:

Prof. Dr. Wolfgang Hansen

Dekan der Fakultät MIN:

Prof. Dr. Heinrich Graener

Summary

Single-particle diffractive imaging at x-ray free-electron lasers is a promising technique for reconstructing the three dimensional structure of biomolecules such as proteins or viruses, avoiding drawbacks of conventional diffractive imaging methods, such as the need of crystalline sample. In order to achieve atomic resolution a huge amount of diffraction patterns of identical particles, ideally in gas phase are needed. Currently such experiments are limited, amongst other things, by the sample delivery set-up, typically aerosol injectors, not providing the densities necessary, to have on average a single particle in the x-ray focus. Within this dissertation, several improvements either of the delivery set-up itself, or of the characterization scheme used to optimize aerosol injectors are presented. A new simulation framework for the computation of particle trajectories through aerosol injection set-ups was developed to not only be limited by empirically derived values for specific conditions, e. g., room temperature, but to be general applicable to particles in rarefied gases. These simulations are able to reliably describe density measurements of a current aerodynamic lens stack injector. Also they are able to reproduce data measured for injection devices, developed and build within the scope of this work. These new injectors are an aerodynamic lens stack tailor made for the needs of single-particle diffractive imaging experiments with a quick release mount allowing for fast adoption of the geometry and a buffer gas cell using helium at a temperature of 4 K and providing shock frozen sample. In addition a method to measure pressure maps at the tip of an aerosol injector within a vacuum chamber was developed and demonstrated.

Zusammenfassung

Die Nutzung der Röntgenstrahlung von freien-elektronen Lasern verspricht die drei-dimensionalen Struktur von einzelnen Biomolekülen, wie Proteinen oder Viren zu bestimmen. Um dabei atomare Auflösung erreichen zu können sind sehr viele Beugungsbildern identischer Teilchen notwendig. Durch experimente an einzelnen Teilchen können dabei die üblichen Nachteile, wie die Notwendigkeit von kristallinen Strukturen umgangen werden. Aktuell limitiert dabei noch Probenaufbau, typischerweise ein Aerosolinjektors der verantwortlich dafür ist die Probe in Form eines Molekülstrahls bereit zu stellen, die Effizienz dieser Experimente. Der Molekülstrahl weist nicht die ausreichende Teilchendichte auf, die notwendig wäre um im Schnitt ein einzelnes Teilchen im Fokus des Röntgenstrahles zu haben. Im Zuge dieser Dissertation werden mehrere Verbesserungen, entweder an dem Probenaufbau selbst, oder an dem Charakterisierungsschema, das genutzt wird um diesen Aufbau zu Optimieren, vorgestellt. Ein neues Simulationskonzept für die Berechnung von Teilchentrajektorien durch Aerosolinjektoren wurde aufgesetzt. Dabei sind die Simulationen nicht mehr auf empirisch bestimmte Werte angewiesen und somit auch nicht mehr in der Anwendbarkeit auf bestimmte Konditionen, wie zum Beispiel Raumtemperatur, beschränkt. Diese Simulation sind in der Lage Messungen von einem aktuellen Aerodynamischen Linsen System zu beschreiben. Zudem können sie Messdaten reproduzieren, die für Injektoren aufgenommen wurden, die im Rahmen dieser Arbeit entwickelt und gebaut wurden. Einer dieser neuen Injektoren is ein Aerodynamisches Linsen System angepasst an die Bedürfnisse von Röntgenbeugungsexperimenten. Es verfügt über einen Schnellverschluss und erlaubt schnell die Geometrie zu wechseln. Der zweite Injektor is eine Puffergaszelle die mit Helium bei Temperaturen von 4 K arbeitet und schockgefrorene Probem bereitstellt. Zudem wurde eine Methode konzipiert und demonstriert um Drücke an unterschiedlichen Positionen an der Spitze eines Aerosolinjektors zu messen.

Contents

Acronyms	III
1 Introduction	1
1.1 Outline of this thesis	2
2 Fundamental concepts	5
2.1 Experimental methods	5
2.1.1 Particle beam generation	5
2.1.2 Characterization of the injection system in the laboratory	8
2.1.3 Generic setup	9
2.2 Simulation methods	11
2.2.1 Simulating carrier gas flow fields	11
2.2.2 Simulating particle trajectories	12
3 Characterizing gas flow from aerosol particle injectors	17
3.1 Introduction	17
3.2 Experimental Method	18
3.3 Results and Discussion	21
3.4 Conclusion	24
4 Optimizing aerodynamic lenses for single particle imaging	25
4.1 Introduction	25
4.2 Methods	27
4.2.1 Numerical Simulation	27
4.2.2 Experimental Setup	29
4.2.3 Theoretical description of the experimental setup	29
4.3 Results & Discussion	30
4.3.1 Validation against literature simulations	30
4.3.2 Particle Beam Characterization	30
4.3.3 Radial distribution analysis	36
4.4 Conclusion	40
5 Aerodynamic lenses at FLASH	41
5.1 Introduction	41
5.2 Methods	41
5.2.1 Experimental setup at FLASH	41
5.2.2 Aerodynamic lens stack	42
5.2.3 Trajectory simulation	42
5.2.4 Pattern classification	43
5.3 Results & Discussion	44
5.4 Conclusion	46
6 Controlled beams of shockfrozen, isolated, biological and artificial nanoparticles	49
6.1 Introduction	49
6.2 Methods	51
6.2.1 Experimental details	51
6.2.2 Simulation details	51

6.3	Results and discussion	53
6.4	Conclusion and outlook	62
7	Microscopic force for aerosol transport	65
7.1	Introduction	65
7.2	Modeling the particle transport in an aerosol injector for single-particle diffractive imaging (SPI) Experiments	67
7.2.1	Drag force in an aerosol injector for SPI experiments	67
7.2.2	Temperature changes of the aerosol	68
7.2.3	Brownian Motion	69
7.3	Benchmarking the new force	70
7.3.1	Comparison to Stokes' drag force	70
7.3.2	Comparison to Newton's law of cooling	70
7.3.3	Comparison to experimental Results	71
7.4	Conclusion	72
8	Conclusion	75
	Bibliography	77
	Acknowledgments	91
	Eidesstattliche Versicherung	93

Acronyms

1D one dimensional.

2D two dimensional.

3D three dimensional.

ADL aerodynamic lens.

ALS aerodynamic lens stack.

BGC buffer-gas cell.

CEM cryo-electron microscopy.

CpGV *Cydia pomonella* granulovirus.

FLASH Free-electron LAser in Hamburg.

FWHM full width at half maximum.

GDVN gas dynamic virtual nozzle.

PS polystyrene spheres.

SFX serial femtosecond crystallography.

SPI single-particle diffractive imaging.

XFEL x-ray free-electron laser.

1 Introduction

What is life? [1, 2] How does life work? These questions were raised by humanity countless times and are part of one of the greatest riddles that science wants to unravel. Not only are the answers to these questions important to us because of our natural desire for a purpose of life, but the hope that understanding mechanisms of life enables us to control or at least influence these, e. g., in order to save ecosystems or cure diseases. While some of the fundamental ingredients, such as atoms and electrons, can be described by physical theories, namely, quantum mechanics, most of the phenomena we connect to life consist of so many of these fundamental ingredients that their interplay gets rather complex. So complex that a full theoretical description is still inaccessible in these days and age.

One strategy that already proved successful for tackling this complex mechanics, is to observe many of them in order to draw conclusions and to develop a simplified model that is able to predict these complex behaviours. Observation in this context means to track the objects of interest in space and time. It is desired to increase the resolution of the observation so that we are able to close the gap between the fundamental theories and macroscopic models. An observation at the time and length scales of atoms is called a molecular movie [3]. The challenge that remains is to develop the experimental tool with such a spatial and temporal resolution that tracking the position and the dynamics of atoms and electrons in a molecule is possible.

The most natural way for humans to observe is to see, to detect photons that scattered from the object of interest. The spatial resolution that can be achieved with electromagnetic radiation, such as light, can be defined by the Abbe diffraction limit. This limit is proportional to the wavelength. For the desired spatial resolution of ~ 0.1 nm, which corresponds to the length of a covalent bond, this requires photons in the energy range of hard x-rays. The desired temporal resolution hardly depends on the kind of dynamics that are of interest. For proteins this could be, e. g., the folding and unfolding process taking place in the time scale of μs [?] to s. Of course combining the observations of these microscopic movement patterns with the motion of single atoms (fs time scale) or of electrons (as time scale) is the ultimate goal. With the advent of the x-ray free-electron laser (XFEL) and its photon energies up to 25 keV and a pulse duration down to the fs range a x-ray source that suits the requirements for these experiments got accessible. The short x-ray pulse durations come in handy. The intense x-ray pulse interacts with the sample and causes radiation damage, perturbing the native structure of the sample. Any structural change of the sample during the x-ray pulse is undesired and reduces the spatial resolution, since the first photons in the pulse diffract from an object with a different structure compared to the last photons of the same x-ray pulse. The pulse duration of XFEL sources is short enough so that the displacement of the atoms during the pulse is smaller than the achievable spatial resolution [4, 5].

The collection of a series of two-dimensional diffraction patterns from randomly oriented objects allows the reconstruction of the full three-dimensional structure. This has been implemented quite successfully in serial femtosecond crystallography (SFX) [6]. But this technique requires crystals or nano-crystals of sample. For some samples such as membrane proteins it is up to now difficult or impossible to form these crystals. Also the crystalline environment offers challenges when moving towards dynamics, e. g., the collective excitation of all molecules in the crystal. SPI promises to overcome these limitations by using individual sample particles. The signal expected from a single particle is much lower without the enhancing effect of the crystal. The reduced signal from single scattering events introduces several challenges for SPI experiments. A lot more

diffraction patterns compared to SFX are necessary in order to achieve the same spatial resolution [7, 8]. As every intercepted particle is destroyed by the intense x-ray pulse [9], a new particle has to be delivered into every x-ray pulse. For SFX common delivery methods are based on liquid jets [10]. The background in the diffraction signal that emerges from the liquid eliminates this method for SPI experiments. Aerosolized beams [11], which offer significant lower background levels [10, 12], is the sample delivery method of choice for SPI of particles in the range of a few nm to a few hundred nm. The repetition rate of the x-ray as well as the measurement time accessible is limited by the current XFEL sources available. Hence, in order to collect the amount of diffraction patterns needed for reconstruction, the particle density in the x-ray focus has to be high enough to ensure preferably a single particle in the focal volume at any given time.

The most widespread aerosol injectors for SPI experiments are aerodynamic lens stack (ALS)s [11, 13]. However, other aerosol injectors, e. g., convergent nozzles, have also been demonstrated [12, 14]. Using current aerosol injectors, hit fractions, i. e., the fraction of x-ray pulses that hit at least one particle, up to 79 % could be achieved [13]. However, this contains pulses interacting with multiple particles, faint hits far from the x-ray maximum intensity, as well as hits from background particles. This leads to 'practical' hit rates, i. e., usable diffraction patterns containing a bright image from a single isolated target particle, of below 5 % and, hence, long measurement times and excessive sample consumption. Furthermore, these current studies have been undertaken with x-ray-focal-spot sizes on the order of a few micrometers. Even so sub 3 nm resolution was recently achieved for gold nanoparticles [?], given the XFEL set-ups, this comparatively soft focusing of the XFEL pulse does not yield the photon numbers required for measurable SPI diffraction signal to high scattering angles from small biomolecules, such as proteins [15]. This requires nanofocused x-ray beams with focal spot sizes on the order of 100 nm, where the hit-rate achievable with current aerosol injectors is typically below 0.05 %.

Hence, optimizing current and developing new sample delivery methods based on aerosol particle beams is a key task to make SPI experiments on proteins feasible for being a core method for frequent structure determination and a potential recording of a molecular movie. Optimization requires iterating multiple times through the steps of adapting current injectors and measuring their performance. Each single step is time consuming and the parameter space for optimization is huge. Relying only on empirical insights from experiments would not allow for an efficient optimization. Simulations of aerosol injectors, when being able to accurately predict experimental results would allow for performing the iterative optimization *in silico* within a fraction of the time. The needed experimental work would be reduced to a simple validation of the simulated optimized result and the actual SPI experiment itself. Even in case the predictions are not accurate enough to completely refrain from experimental optimization, they would significantly reduce the parameter space. Hence, simulations are crucial in order to make optimizations of the injectors for specific samples feasible at all.

1.1 Outline of this thesis

The chapter 2 provides the fundamental concepts used during the experiments and simulations. One challenge in setting up a simulation is to specify the correct boundary conditions. In case of simulating the gas expansion from inside of an aerosol injector into the vacuum it is in particular difficult to set the correct pressure boundary. In chapter 3 a new experimental technique is reported that enables measuring these pressures at the tip of an aerosol injector by imaging the emitted light from a laser induced plasma of

the background gas. First results of simulating an existing ALS for SPI experiments in chapter 4 successfully benchmark the simulations against experimental data. Furthermore they generate insights into the mechanics and utilization of aerodynamic lenses that triggered the design of a new ALS tailor-made for the needs of SPI. This new ALS and its first application at a beam time at Free-electron LAsER in Hamburg (FLASH) is described in chapter 5.

Controlling the sample particles is not limited to their translational degrees of freedom. Aerosols at room temperature naturally undergo structural variations, such as conformational changes. The dataset taken during an experiment not only has to be analyzed for structures in terms of spatial orientations but conformations as well. For a given measurement time at a XFEL facility this will limit the achievable resolution. A beam of shock-frozen, isolated nanoparticles not only addresses this problem. In addition it is a better target for even further control techniques, e. g., by external electric fields. First experimental results from a new cryogenic aerosol source are further described in chapter 6 and compared to simulations. The Simulations based on Stokes' drag force are limited to nitrogen at room temperature as used gas for reliable results. For better description of injectors at cryogenic temperatures a new model for describing the force of a rarefied gas on a particle is reported in chapter 7. The approach is based on Epstein's formulation and is not limited to further specific conditions, such as the temperature or the gas type. This model will allow for optimizing aerosol injectors in an even larger parameter space, e. g., cryogenic temperatures. First simulation results are compared to experimental data from the new cryogenic aerosol source.

2 Fundamental concepts

2.1 Experimental methods

It is crucial to understand the current experimental designs and methods for creation of a high density beam of isolated single particles and the tools that are available for characterizing these beams in the laboratory.

2.1.1 Particle beam generation

The sample of interest for SPI experiments, such as proteins or viruses, usually comes in solution, either water or a specific buffer. Hence, the first task when creating a stream of aerosols is to aerosolize the sample (see Section 2.1.1). Since the aerosolization takes place under near atmospheric conditions and the final experiment is carried out in vacuum a differential pumping stage (see Section 2.1.1) is needed. Finally the particles need to be transported into the interaction volume of the measurement device. For SPI experiments this is the focus region of the XFEL beam. The goal here is to ensure particle densities high enough, so that a single particle is in this interaction volume for every x-ray pulse. For ions electrical fields could be used to achieve the needed control [16], but in order to not be restricted to charged particles, hydrodynamic forces are used to manipulate the translational degrees of freedom of the single particles. The most widespread aerosol injectors for SPI experiments are ALS [11, 13], which are explained in more detail in Section 2.1.1. However, other aerosol injectors, e. g., convergent nozzles, have also been demonstrated [12, 14, 17].

Aerosolization

Different methods for bringing sample from solution into gas phase exists, e. g., electrospray [18], nebulizer [19], or a gas-focused liquid jet, such as a gas dynamic virtual nozzle (GDVN) [10]. The conceptual idea of these methods is to create droplets of the solvent containing ideally single particles of the sample per drop. Throughout the scope of this work a GDVN was used. Figure 2.1 shows a schematic of this device. The liquid sample is pushed through a capillary with a diameter of a few ten μm . The capillary itself is located within another capillary. High pressurized gas is flowing through the outer capillary. Both capillaries are converging towards their tip and the so achieved decrease diameter additionally accelerates the gas. The gas applies a force on the liquid, at the liquid gas interface, essentially pulling and accelerating it, while expanding out of the GDVN. This forms a so called liquid jet with a diameter down to $\sim 1 \mu\text{m}$. The jet breaks up after a few hundred μm to mm creating droplets with diameters down to a few hundred nm. The probability of such a droplet containing a single sample particle depends on the concentration of the sample and the droplet size. The remaining solution around the sample evaporates leaving behind the sample as aerosol. Any buffer, such as salt, or other impurities within the droplet will not evaporate, creating an unwanted layer around the sample particle. The thickness of the layer depends on the amount of liquid evaporated. So smaller initial droplet sizes allow for cleaner aerosolized sample. The initial droplet size depends on the jet diameter, which depends amongst others on the liquid flow rate and the diameter of the capillary. A smaller capillary and liquid flow rate leads to smaller initial droplet sizes. Using smaller capillary diameters increases the chance for clogging, currently limiting this technique, to be a suitable for samples down to the 100 nm size range. For smaller samples the technique of electrospraying seems to be more promising.

This relies electrostatic forces for jet formation, which are potentially much higher than the aerodynamic forces. Additionally charge induced coulomb fission in the droplets removes remaining solvent around the sample without increasing the impurity or buffer concentration like evaporation [20].

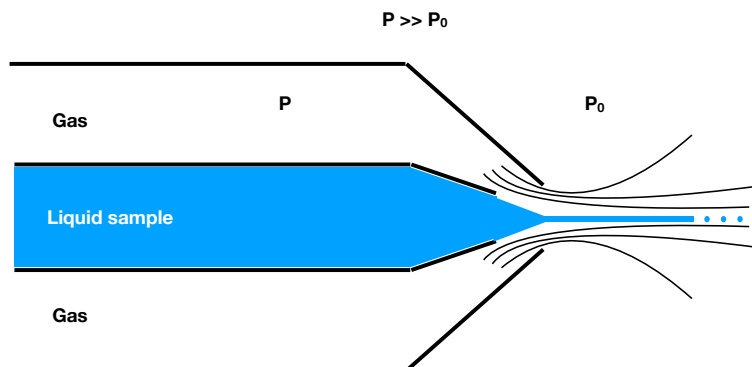


Figure 2.1: Schematic drawing of a GDVN.

Differential pumping

Current aerosolization methods take place under close to atmospheric pressure conditions. For SPI experiments it is necessary to have pressures in the order of 10^{-6} mbar or lower, to fulfil technical limitations of typical beamline endstations and detectors. The reduced gas load can be achieved by limiting the leaking of the gas from the aerosolization chamber to the detection chamber via a small orifice on the cost of very small sample flux. To ensure the highest possible sample flux, while keeping the gas flux low, a nozzle skimmer assembly is used. Figure 2.2 shows a sketch of such an assembly with typical dimensions. Upstream of the nozzle the pressure is on the order of 100 mbar. Downstream of the skimmer the pressure is around 1 mbar. Between nozzle and skimmer a pre-vacuum pump removes as much gas from the system as possible. In the nozzle the gas and hence the aerosolized sample gets accelerated. The pressure difference before and after the nozzle are great enough for the gas flow to reach velocities greater than the speed of sound. Such a super sonic expansion creates shock waves. The region between the nozzle tip and the first occurring shock wave is called the zone of silence [21]. Within this zone the gas expands freely with a high divergence. Contrary, the sample continues on a almost straight trajectory due to its high moment of inertia. The skimmer is placed at a distance to the nozzle within this zone of silence, protecting the sample from the shock wave and while ideally all sample particles transmit through the skimmer only a fraction of the gas molecules do. By changing the nozzle skimmer distance or their inner diameters the conditions for different samples or amount of gas removed can be tuned.

Particle beam compression

The goal of the injection system is to transport the provided sample into the interaction region, namely, the focus of the XFEL beam. As particles distribute stochastically in the resulting aerosol beam, the probability for them to be within the interaction volume depends on the local particle density, necessitating highly compressed or focused particle streams. Robinson predicted in 1956 that in real, irrotational and incompressible gas flow

past an obstacle, the density of small particles within the flow can increase while passing the obstacle [22]. This mathematical description was later extended and used, supported by numerical simulations, to describe particles flowing in a tube through an orifice [23]. Under the right conditions, in what is now known as an aerodynamic lens (ADL), the particles concentrate at the center of the tube, as illustrated in Figure 4.1.

A detailed numerical characterization of an individual ADL was presented in 2002 [24], which was later extended to an entire ALS [25]. Figure 2.3 shows a sketch of such an ALS. Numerical simulations for an ALS to focus particles with diameters below 30 nm [26]

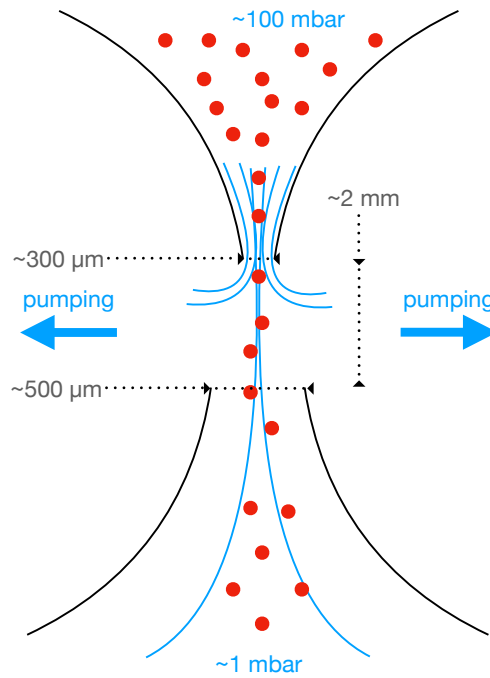


Figure 2.2: Schematic drawing of the nozzle-skimmer set-up for differential pumping with typical dimensions and pressures. Sample particles are depicted as red circles and the gas flow as blue lines.

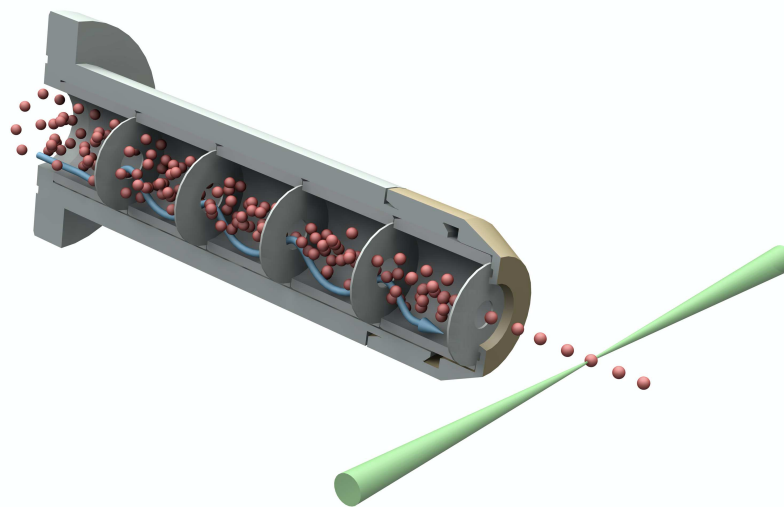


Figure 2.3: Schematic drawing of an ALS. The particles are depicted as red spheres, the gas flow as blue arrow and the probing laser as green cone.

led to a simple design tool that predicts the required lens dimensions to focus a specified range of particle sizes at given flow conditions [27]. Based on this, further numerical simulations have adapted ALS to specific needs [28, 29]. Although ALS have been used for, e. g., ultrafast electron imaging experiments on nanoparticles [30], they are predominantly used in aerosol mass spectrometry [31]. Here, the main goal is to contract a large range of particle sizes and ensure a high transmission. As previously mentioned, for specific needs of SPI experiments, the highest possible compression, hence, particle density is needed. This necessitates, that each ADL in the ALS is optimized for the current sample used in the experiment. Thus, for every different sample a completely new ALS geometry is necessary. Even for the same sample, not always the same geometry leads to highest particle densities for different flow conditions, that might arise from varying aerosolisation properties. Optimizing the ALS involves changing its geometry and measuring the resulting particle beam characteristics iteratively. Changing the geometry involves dis- and reassembling parts of the the injection set-up. Doing so during the actual experiment at a XFEL beam line is not feasible, due to the limited amount of time. Hence, an efficient characterization set-up in the laboratory is crucial.

2.1.2 Characterization of the injection system in the laboratory

When characterizing an aerosol injector for SPI experiments, there are two performance indicators, the transmission and the achieved particle beam density. The transmission is the ratio of particles transmitted through the injection system to the total amount of particles, that entered the injection system. Usually the concentration of your sample in solution is limited either by the production process or by the fact, that higher concentrations would lead to aggregation of sample. Hence, for achieving highest particle densities it is necessary to have a high transmission. A high transmission is also beneficial for injection efficiency and keeping the sample consumption at a minimum. Since the concentration and injection rate of the liquid sample is known, for measuring the transmission of the injection system, including the differential pumping stage, it is only necessary to count the particles leaving the aerosol injector. For defining the particle beam density this is not enough. Aerosol injectors create focused particle beams leading to varied densities dependent on the position in three dimensional (3D) space. Hence, for measuring the achieved particle beam density it is necessary to count the particles with spatial resolution. Both, counting the particles and tracking them in space, can be achieved by using light

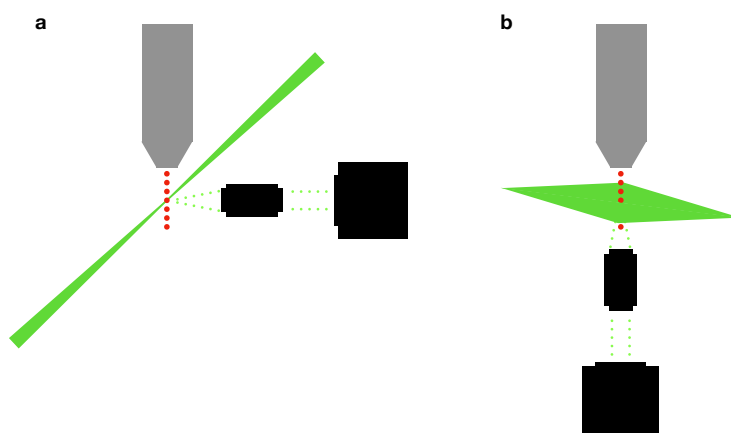


Figure 2.4: Schematic drawing of a side-view particle imaging (a) and a on axis light sheet imaging (b) set-up.

scattering and either direct side-view particle imaging schemes [14] (Figure 2.4a)) or on axis light sheet imaging [32] (Figure 2.4b)). A light source is directed at the particle beam in both cases. The light is scattered by the particles and collected by an objective camera assembly orthogonal or on axis to the particle beam. For this measurement only the position of the particle is of interest not its structure. Hence, light with a wavelength in the visible range can be used. Identifying individual particles on the camera image is only possible when the motion of the particle is 'frozen' during exposure [33, 34]. For side-view imaging a short pulsed laser is necessary. Expecting particle velocities in the order of 100 m/s and desired resolutions on the order of 1 μm results in necessary pulse durations below 10 ns. Assuming an axis symmetric particle beam the images of particles projected onto the camera plane can be used to reconstruct a 3D particle beam [35]. In case of on axis light sheet imaging a continuous wave laser beam is focused only in one direction and collimated in the other. This is creating a sheet of light with the collimated axis being orthogonal to the particle beam. In this case the exposure is pulsed by the particles flying through the light sheet. An advantage of this method is, that the duration of the exposure decreases with increasing speed of the particles and the observed motion is only dependent on the ratio of transversal to tangential velocity. Assuming a 10 μm thick sheet and again a desired resolution of 1 μm this would lead to precise measurements of particle beams with an opening angle below $\sim 11^\circ$. In both cases the particle appears as a single nearly round object on the camera image. Hence, centroiding techniques allow for sub pixel resolution [36–38]. The amount of scattering visible on the camera image per particle depends on the numerical aperture of the objective, the efficiency of the camera, the amount of photons interacting with the particle, the size of the particle and the scattering angle. The scattering intensity of particles with sizes comparable to the used wavelength can be theoretically predicted using Mie scattering. For smaller particles the simpler Rayleigh scattering theory predicts a dependency of the scattering intensity on the particle diameter with the power of six [39]. Nowadays cameras with an efficiency close to one are available and, together with high numerical aperture objectives, do not leave a lot of room for improvement on this side of the set-up. Thus, the used laser beam source defines the limit of particle size, that still can be imaged. Here a pulsed laser source is beneficial usually being able to provide a lot more photons per pulse compared to a continuous wave source during the same amount of time. Also the possibility to focus the beam in two dimensions compared to one for the light sheet imaging gives the side-view approach an advantage for smaller particles in the size range of a few ten nm and smaller, while limiting the field of view. A detailed description of such a set-up can be found in [14].

2.1.3 Generic setup

Figure 2.5 shows a schematic drawing of a generic sample injection set-up for SPI experiments. Details of the exact set-up used in the experiments can be found in the later chapters. SPI experiments need a high local density of isolated sample particles in the focal region of the x-ray. Biological sample, such as proteins and viruses, natively exist in solution under atmospheric pressures. An experimental set-up transferring the sample from its native surrounding into a high density aerosol beam can be realized using a GDVN for aerosolizing the sample, a nozzle skimmer assembly for transferring the sample from near atmospheric pressures into vacuum and an ALS for increasing the local density. With decreasing sample size several challenges arise, such as the impurity layer around particles caused by extensive evaporation of the solution, or insufficient particle densities achieved with the ALS. These challenges necessitate optimization of the experimental set-up, hence

a possibility to efficiently characterize potential new experimental assemblies. Such a characterization can be achieved by light scattering and either direct side-view particle imaging schemes or on axis light sheet imaging.

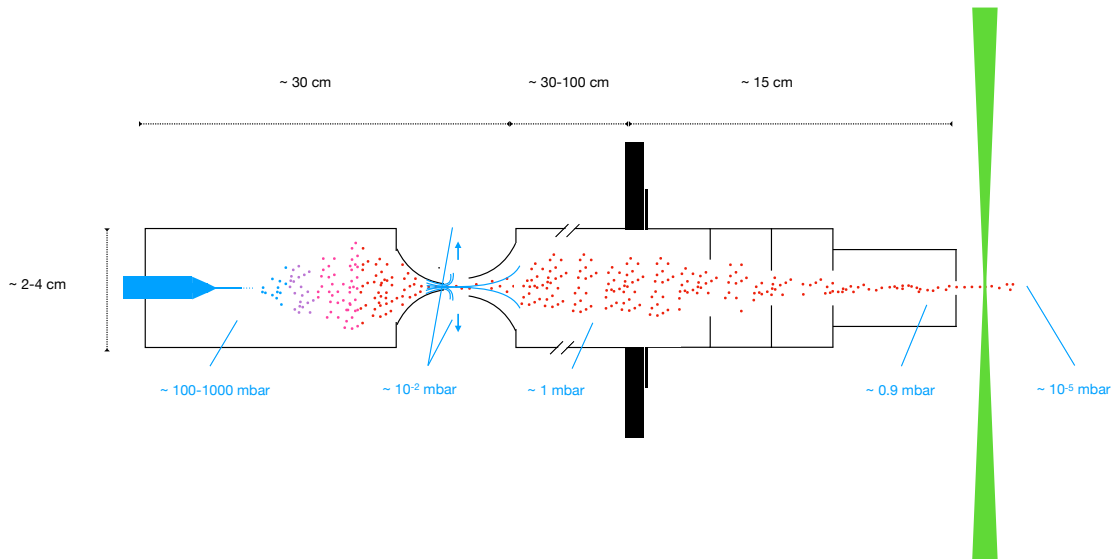


Figure 2.5: Schematic drawing of a generic sample injection set-up for SPI experiments, with rough local pressures and dimensions

2.2 Simulation methods

Preparing an ALS for a SPI experiment necessitates a substantial amount of optimization and characterization. A laboratory characterization set-up helps, but is still time consuming and expensive, taking all the manufacturing of the different ADLs for an extensive geometry scan into account. Hence, another key asset is the ability to do these characterizations and optimizations *in silico*. An aerosol injector consists of a carrier gas and the sample particles moving through the device. Thus, simulating it means simulating the interaction of these three components with each other and themselves. The carrier gas used in an typical aerosol injector is helium at ~ 1 mbar (number density of $\sim 10^{16}$ atoms/cm³), while the density of particles usually does not exceed 10^{10} particles/cm³. So in order to significantly reduce the complexity no interaction between sample particles and no influence of the sample particle on the carrier gas is assumed. This allows for separate calculation of the carrier gas flow field and individual sample particle trajectories.

2.2.1 Simulating carrier gas flow fields

Simulating the movement and interaction of the carrier gas molecules is highly complex simply due to the sheer amount of these gas molecules and their collisions with each other. It is possible to define several regimes for different amounts of collisions a molecule undergoes while travelling a specific distance. The Knudsen number Kn expresses the ratio of the mean free path of a carrier gas molecule to a characteristic length in the geometry. For rarefied gases ($Kn > 1$) it is still feasible to model gas molecule collisions. Typical approaches like the lattice Boltzmann method [40] or direct simulation Monte Carlo solve some form of the Boltzmann equation. In the molecular flow regime ($Kn \gg 1$) the amount of collisions between molecules is even negligible compared to the amount of collisions with the wall. Inside an typical ALS the pressure is usually on the order of 1 mbar, corresponding to a mean free path around 70 μm for helium at room temperature. Compared to the dimensions of apertures (a few mm) this results in $Kn < 0.01$, i. e., there are too many collisions between carrier gas molecules to treat them explicitly. In order to simulate the carrier gas in this regime it is treated as continuum flow described by a set of differential equations, the Navier-Stokes equations. They consist of the continuity equation

$$\frac{\delta\rho}{\delta t} + \nabla \cdot (\rho\mathbf{u}) = 0, \quad (2.1)$$

which represents the conservation of mass with ρ being the density and \mathbf{u} the velocity vector,

$$\rho \frac{\delta\mathbf{u}}{\delta t} + \rho (\mathbf{u} \cdot \nabla) \mathbf{u} = -\nabla p + \nabla \cdot \tau + \mathbf{F}, \quad (2.2)$$

which represents the conservation of momentum with p being the pressure, τ the viscous stress tensor and \mathbf{F} the volume force vector, and

$$\rho C_p \left(\frac{\delta T}{\delta t} + (\mathbf{u} \cdot \nabla) T \right) = -(\nabla \cdot \mathbf{q}) + \tau : \mathbf{S} - \left. \frac{T\delta\rho}{\rho\delta T} \right|_p \left(\frac{\delta p}{\delta t} + (\mathbf{u} \cdot \nabla) p \right) + Q, \quad (2.3)$$

which represents the conservation of energy, C_p the specific heat at constant pressure, T the temperature, \mathbf{q} the heat flux vector, Q the heat source and \mathbf{S} the strain-rate tensor. Solving this equations for the geometry of an ALS can be achieved by using the finite-elements method. Using this method a few additional considerations are necessary. Two other dimensionless quantities classifying the flow are the Reynolds number Re and Mach

number Mi . Re is defined as the ratio of inertial to viscous forces and states how turbulent or laminar a flow is. In principle the mathematical description of a laminar flow and a turbulent flow is identical and both are covered with the Navier-Stokes equations, but the mesh size needed to resolve all the turbulent features can easily increase the computational costs to impractical values. Dividing the flow properties into an average and a fluctuating part allows for approximating these turbulences without the need of an increased number of mesh elements. For simulations of an ALS Re usually does not exceed 10 making these considerations unnecessary. Mi is defined as the ratio of the velocity of the flow to the speed of sound in the fluid. For $Mi > 0.3$ effects due to the compressibility of the fluid, such as pressure waves and cooling of the fluid, start to occur. Again, the effects of high Mi are already mathematically covered by the Navier-Stokes equations. However the numerical simulation approach, finite-elements method, necessitates the use of stabilization methods, which add artificial diffusion in order to avoid numerical instabilities, e. g., oscillations in the solution. This washes out the position and velocity of the potentially occurring pressure waves and needs to be considered, when designing an ALS with such high flow velocities.

2.2.2 Simulating particle trajectories

Once the flow field of the carrier gas is calculated it is possible to calculate the trajectory of a sample particle through the ALS. The Knudsen number $Kn = \frac{\lambda}{d_p}$, which is the ratio of the mean free path of the fluid λ to the diameter of the particle d_p , characterizes the flow regimes. Depending on the flow regime there are several different theories of describing the force that an aerosol undergoes when moving through a gas.

Drag force in the continuum flow regime

The continuum regime is the flow limit for $Kn \ll 1$. In this regime, under the assumption of laminar flow and the particle being a rigid sphere, the drag force can be calculated by Stokes' famous drag equation, given as

$$\mathbf{F}_{St} = -6\pi\mu R\mathbf{U}, \quad (2.4)$$

with the dynamic viscosity of the fluid μ , the radius of the particle sphere R and the velocity difference vector between fluid and particle \mathbf{U} .

Drag force in the molecular flow regime

In a rarefied gas, $Kn \gg 1$, the regime is called molecular flow. For this regime the boundary conditions assumed by Stokes do not hold any more [41] and an empirical correction factor was introduced to the drag force called Cunningham correction factor C as

$$C = 1 + Kn(a + b \cdot \exp(-c/Kn)) \quad (2.5)$$

and

$$\mathbf{F}_C = \frac{\mathbf{F}_{St}}{C} \quad (2.6)$$

with a, b and c being empirical parameters [42]. These parameters were determined several times by fitting the drag force to experimental data, mostly from Milikan's oil droplet experiments [43, 44]. However, this description has known limitations. The smallest oil droplet size Milikan measured is ≈ 300 nm, hence, there is no experimental data

that validates this description for smaller particles. On the other hand the parameters in C would need to vary with gas type and temperature [45] and, as mentioned before, constants are only valid for the exact conditions in Milikan's experiment, namely, air at room temperature. For varied temperatures it is possible to use a temperature dependent correction factor [46], that is derived from kinetic theory considerations and related to experimental data, but only validated from 200 to 1000 K.

Models based on kinetic gas Theory

Another approach to model the force of a rarefied fluid on a particle is to use the kinetic theory of gases. In the molecular flow limit the mean free path of the gas is much larger than the diameter of the particle. Hence, it is a valid assumption that the presence of the particle does not change the regional gas flow, e. g., the velocity distribution of the gas molecules.

In 1924 Epstein published his description of the resistance a sphere experiences when moving through a gas [47] and a lot of modern approaches are extensions to his initial work. Assuming a Maxwell distribution the number of gas molecules having velocity components between v_x, v_y, v_z and $v_x + dv_x, v_y + dv_y, v_z + dv_z$ is given by

$$N_{v_x, v_y, v_z} dv_x dv_y dv_z = N \left(\frac{h}{\pi} \right)^{\frac{3}{2}} e^{-h(v_x^2 + v_y^2 + v_z^2)} dv_x dv_y dv_z, \quad (2.7)$$

with

$$h = \frac{m}{2kT}, \quad (2.8)$$

where N is the Number of molecules per unit Volume, m is the mass of the gas molecule, k is the Boltzmann constant and T is the gas temperature. In the point of view of a particle in the gas moving with velocity components $U_x = \alpha U$, $U_y = \beta U$ and $U_z = \gamma U$ the velocity distribution becomes

$$N_{v_x, v_y, v_z} = N \left(\frac{h}{\pi} \right)^{\frac{3}{2}} e^{-h((v_x + \alpha U)^2 + (v_y + \beta U)^2 + (v_z + \gamma U)^2)}. \quad (2.9)$$

For small U this is in first order

$$N_{v_x, v_y, v_z} = N \left(\frac{h}{\pi} \right)^{\frac{3}{2}} \left(1 - 2hU (\alpha v_x + \beta v_y + \gamma v_z) \right) e^{-\beta v^2}. \quad (2.10)$$

In order to calculate the amount of molecules that will strike the particle we assume a surface element dS of the particle normal to the x direction. The volume that contains all the molecules with velocity $v_x + dv_x$ that will hit the surface in unit time is given by $v_x dS$ and the amount of molecules in this volume by

$$n_{v_x, v_y, v_z} dv_x dv_y dv_z dS = v_x N_{v_x, v_y, v_z} dv_x dv_y dv_z dS. \quad (2.11)$$

The amount of momentum transferred to the particle by an individual gas molecule impinging and sticking to the particle in a given direction is given by $m(\alpha' v_x + \beta' v_y + \gamma' v_z)$.

Hence, the total amount of momentum transferred to dS is

$$\begin{aligned} & m \int_{-\infty}^0 dv_x \int_{-\infty}^{\infty} dv_y \int_{-\infty}^{\infty} dv_z \left(\alpha' v_x + \beta' v_y + \gamma' v_z \right) n_{v_x, v_y, v_z} dS \\ & = -Nm \left(\frac{\alpha'}{4h} + \frac{U}{\sqrt{\pi h}} \left(\alpha \alpha' + \frac{1}{2} \beta \beta' + \frac{1}{2} \gamma \gamma' \right) \right) dS. \end{aligned} \quad (2.12)$$

If the particle is a sphere with radius R and the z -axis is defined to be normal to the plane through x and the direction of U and the angle between these two is θ , then $\alpha = \cos(\theta)$, $\beta = \sin(\theta)$ and $\gamma = 0$. Furthermore, for the momentum transferred in the direction of U $\alpha' = \cos(\theta)$, $\beta' = \sin(\theta)$ and $\gamma = 0$. Integrating over all the surface elements $dS = R^2 \sin(\theta) d\theta d\phi$ the total amount of momentum transferred in the direction of U by gas molecules impinging the particle in unit time is

$$F_{\text{Ep, i}} = \frac{8}{3} \sqrt{\frac{\pi}{h}} NmR^2 U. \quad (2.13)$$

For the momentum transfer from gas molecules emerged from the surface of the particle Epstein calculated several cases [47], with only two of them being relevant, namely specular reflection and diffuse reflection with accommodation. For specular reflection the x component of U α is changing sign, while everything else stays the same. Performing the integration the momentum transferred by the reflecting gas molecules averages to zero and the total force in case of specular reflection is

$$F_{\text{Ep, spec}} = F_{\text{Ep, i}} + F_{\text{Ep, r}} = \frac{8}{3} \sqrt{\frac{\pi}{h}} NmR^2 U. \quad (2.14)$$

The second relevant case is that were the molecule is not reflected, but emerges from the surface diffuse. At the same time the molecule emerges with a Maxwell distribution according to the temperature it gained during accommodation on the given surface element of the particle. This velocity depends on whether the particle can be treated as perfect thermal conductor or insulator with corresponding forces

$$F_{\text{Ep, diff, ins}} = \left(1 + \frac{9\pi}{64} \right) \frac{8}{3} \sqrt{\frac{\pi}{h}} NmR^2 U. \quad (2.15)$$

and

$$F_{\text{Ep, diff, con}} = \left(1 + \frac{\pi}{8} \right) \frac{8}{3} \sqrt{\frac{\pi}{h}} NmR^2 U. \quad (2.16)$$

The experimental data measured by Milikan can be reproduced by assuming 10 % of specular reflections and 90 % of diffuse reflections and the particle to be a perfect conductor, while for smaller particles (around few nm) [48] the process of specular reflection gets dominant.

Advanced models

The assumptions that Epstein made clearly identify the limitations of the theory. First of all it is only applicable in regimes of very high Knudsen number. Second it is only valid for small relative velocities of the particle to the fluid. And third it gets inaccurate if the particle reaches molecular size, because then the treatment as rigid sphere fails and long range interactions, e. g., van der Waals interactions and, when the particle is charged, the

ion-induced dipole interactions, have to be taken into account [45]. Epstein's model was advanced in several ways [45, 49] to molecular sized particles based on Chapman-Enskog theory and kinetic theory of gases or by accounting for quantum effects [50]. While still sticking to first order approximations, which are known to be inaccurate for high relative velocities, light gas types, e. g., Helium, and low temperatures [51]. Another short coming of Epstein's work is the empirical nature of the ratio between specular and diffuse reflection and some tried to get an analytical expression for that [52] or used molecular dynamics simulations [53–55]. Additional advances are treating non isothermal fluids [56, 57] and lift forces due to the rotation of the particle or the velocity gradient in the flow field [58–60].

Brownian motion

All the above forces are calculated by averaging over all collisions the particle undergoes with the carrier gas. While this is correct for predicting the mean force on the particle, for its actual trajectory the Brownian motion of the particle needs to be taken into account. For a numerical description of the Brownian motion using the Langevin equation [61] the force on the particle is split into one part that is proportional to U and one part that is a random force F_b which is assumed to be white noise, consisting of an amplitude and a random number with zero mean and unit variance r . The fluctuation-dissipation theorem defines the amplitude of the random force to be

$$\langle F_b(t_1)F_b(t_2) \rangle = 2kT\mu\delta(t_1 - t_2), \quad (2.17)$$

with $\mu = F_{\text{drag}}/U$. Using a numerical representation of the delta function this leads to

$$F_b = r\sqrt{\frac{2kT\mu}{\Delta t}}. \quad (2.18)$$

Simulations can be a useful tool to assist in the development and optimization process of aerosol injectors. The simulations highly depend on the flow and pressure regime of interest. For simulating the trajectories of sample particles through an injector for SPI experiments on few ten to hundred nanometer sized particles, the simulation of the gas and the simulation of individual sample particles can be done separately. The gas flow can be simulated solving the Navier-Stokes equations using the finite-element method. Throughout this work COMSOL Multiphysics [62] was used as finite-elements solver. For the trajectories of sample particles through the gas solving Stokes' drag equation with empirical corrections for rarefied gases is a popular choice. The applicability of these corrections is limited to experimental conditions similar to the experiments used to obtain these. Epstein's model of the drag force in gases provides a more general approach. For high relative velocities between particles and the gas flow, particles sizes below 10 nm or a temperature difference between particles and gas further advances of these model is necessary. All particle trajectory calculations were preformed using a self build Python simulation framework, that allows the usage of pre calculated velocity fields for the flow and flexible switching of the used force model. This simulation framework was later extended to the Python framework called CMInject, allowing the combination of several pre calculated fields, different forces and even two dimensional (2D) and 3D fields.

3 Characterizing gas flow from aerosol particle injectors¹

A novel methodology for measuring gas flow from small orifices or nozzles into vacuum is presented. It utilizes a high-intensity femtosecond laser pulse to create a plasma within the gas plume produced by the nozzle, which is imaged by a microscope. Calibration of the imaging system allows for the extraction of absolute number densities. We show detection down to helium densities of $4 \times 10^{16} \text{ cm}^{-3}$ with a spatial resolution of a few micrometer. The technique is used to characterize the gas flow from a convergent-nozzle aerosol injector [17] as used in single-particle diffractive imaging experiments at free-electron laser sources. Based on the measured gas-density profile we estimate the scattering background signal under typical operating conditions of single-particle imaging experiments and estimate that fewer than 50 photons per shot can be expected on the detector.

3.1 Introduction

The advances of XFELs, which provide intense and short pulses of coherent x-rays, open up new possibilities for imaging of aerosolized particles, and even individual molecules, with atomic spatial resolution [11, 15, 63, 64]. As experiments can be conducted completely in the gas phase and do not require sample immobilization, e. g., cryogenic freezing, XFELs furthermore provide unprecedented capabilities for capturing ultrafast dynamics of isolated systems with femtosecond temporal and picometer spatial resolution [15, 65–67]. This is enabled by the short and intense x-ray pulses available at these facilities, which typically provide pulses with $\sim 1 \text{ mJ}$ pulse energy, $\sim 10 \text{ fs}$ pulse duration, and $\sim 100 \text{ pm}$ wavelength. This allows the imaging methodology to outrun radiation damage effects in the *diffraction before destruction* mechanism [4, 5, 68, 69]. Combining many diffraction patterns from reproducible isolated aerosol targets imaged at different orientations should allow one to reconstruct the three-dimensional, atomically resolved structure [7, 70]. In recent years full 3D reconstruction has been demonstrated and the achieved resolution continuously improved [13, 71–73].

The advent of these new possibilities for imaging isolated systems *in vacuo* has prompted the development and improvement of techniques for injecting samples into the interaction region. Using GDVNs [10] for producing focused liquid jets enabled the SFX methodology [74, 75], allowing the reconstruction of sub-nanometer-resolution structures from micrometer sized crystals [74, 76]. Aerodynamic lenses [11, 23] and convergent-nozzle injectors [17] are widely used injection techniques to produce focused or collimated streams of nano- or micrometer sized particles. They fundamentally rely on a gas flow that interacts with the particles of interest and, through shear and drag forces, produces the desired stream of particles. Typically, helium is used for its relatively small x-ray scattering cross-section. However, since the helium gas density at the interaction point is still many orders of magnitude higher than the sample density, scattering from the focusing gas can make a significant contribution to the recorded background scattering [12, 63, 77]. In order to account for this background and to make quantitative predictions and background

¹This chapter is based on the publication: D. A. Horke, N. Roth, L. Worbs, and J. Küpper, “Characterizing gas flow from aerosol particle injectors,” *J. Appl. Phys.* **121**, 123106 (2017). I contributed to the development of the idea for this experimental technique, performed early proof of principle measurements and contributed to the set-up of the experiment reported in this publication.

calibrations, therefore, requires knowledge of the gas density at the interaction point, typically located a few hundred micrometers below the injector tip [17].

Here, we present a methodology that allows the spatially resolved measurement of gas densities down to $\sim 4 \times 10^{16} \text{ cm}^{-3}$ with high spatial and, potentially, temporal resolution. This is achieved by using a high-intensity femtosecond laser pulse to create a plasma within the gas stream, which is then imaged by a microscope objective and camera. The observed intensity of the plasma depends on the local gas pressure in the laser focus. By calibrating the plasma formation and imaging system to known helium pressures, this method allows us to create spatial maps of the gas flow from an injector tip. Compared to previous methods [78, 79], this approach provides a higher sensitivity, allowing the detection of one order of magnitude lower gas pressures, and it does not rely on interferometric measurements prone to mechanical instabilities. In particular, we characterize a convergent nozzle injector [17] under typical operation conditions for XFEL single-particle diffractive imaging experiments. Based on the measured gas-density distribution, the x-ray scattering signal expected from this helium background at typical operating parameters of currently available XFEL endstations is calculated.

3.2 Experimental Method

To assess the local gas density at the tip of an aerosol injector the gas stream was crossed with a focused Ti:Sapphire femtosecond laser beam of sufficient intensity to produce a plasma inside the gas stream. The bright visible glow of this plasma was recorded on a camera. The intensity depended on the laser intensity and the gas density in the interaction volume. By calibrating the imaging system at known gas densities, this allowed us to build up a high-resolution spatial map of local gas densities produced by the injector tip.

A simple sketch of the vacuum and imaging system is shown in Figure 3.1 a. The vacuum system consisted of two differentially pumped chambers, connected only through the injector tip. The upper chamber, i. e., upstream of the injector, contained a capacitive pressure gauge (Pfeiffer Vacuum CMR361) with an absolute accuracy of 0.2% independent of gas type, a high-precision leak valve connected to a high-purity helium supply and a connection to a roughing pump, with the pumping speed controllable through a needle valve. This setup allowed us to maintain a constant pressure during operation of the injector by matching the helium flow into the upper chamber to the gas transmission through the injector aperture. This chamber mimicked the typical nebulization chamber in single-particle imaging experiments. The injector tip, with an 30° convergence angle and an $111 \mu\text{m}$ orifice [17], was mounted on a 6 mm outer diameter stainless steel tube at the bottom of this upper chamber. It was located within the main vacuum chamber as shown in Figure 3.1 a. This chamber was evacuated by a turbomolecular pump (Pfeiffer Vacuum HiPace 80) and the pressure was monitored through a full-range pressure gauge (Pfeiffer Vacuum PKR361).

The laser passed through the interaction chamber perpendicular to both, the gas-stream and the imaging axis, as indicated by the red cross in Figure 3.1. It consisted of pulses from an amplified Ti:Sapphire laser system (Spectra Physics Spitfire ACE) centered around 800 nm, running at 1 kHz repetition rate, and producing 40 fs pulses with 0.7 mJ per pulse used in the current experiment. The laser beam (waist $\omega \approx 5 \text{ mm}$) was focused into the interaction region with a $f = 300 \text{ mm}$ plano-convex lens, producing a focal spot size of $50 \mu\text{m}$ (4σ) with a nominal Rayleigh range of $z_R \approx 2.5 \text{ mm}$ and a peak intensity of $8.9 \times 10^{14} \text{ W/cm}^2$. The focusing lens was placed on a 3D translation stage to allow translation of the laser focus in space to ensure overlap with the gas stream within the

Rayleigh range and to allow probing of the local gas densities at different distances from the injector nozzle.

The laser-matter interaction was imaged through a standard vacuum viewport with a $10\times$ long-working-distance microscope objective (Edmund Optics 59-877) that produced an image on a high-sensitivity CMOS camera (Thorlabs DCC3240M, 10 bit monochrome, $5.3\ \mu\text{m}$ pixel size). Residual stray infrared light from the femtosecond laser was blocked using two shortpass filters (Thorlabs FESH0700, $\text{OD} > 5$ for $\lambda > 700\ \text{nm}$) mounted between the objective and the camera and stray light was reduced by mechanically enclosing the optical path. The entire imaging system (objective, filters, camera) was mounted on a three-dimensional translation stage.

The imaging system was calibrated by recording the plasma-glow intensity when flooding the chamber to a known helium pressure.

For calibration of the observed plasma-glow intensity in the image against a known density of helium gas, the injector tip and mounting was removed from the chamber and the entire chamber flooded with helium gas at known, constant pressures in the range from 0.8 to 4.1 mbar, measured by the capacitive gauge. During these measurements the turbomolecular pump is switched off and the chamber is pumped by the roughing pump, ensuring a constant replenishment of the helium. An example image of a produced plasma is shown in the inset of Figure 3.2.

To calibrate the recorded image intensity with respect to the chamber pressure, we record 20 images at a given pressure, and repeat this for different camera exposure times,

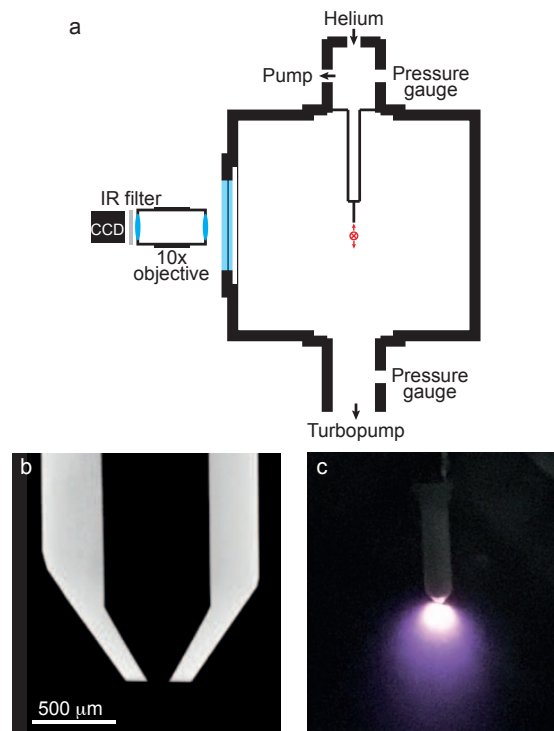


Figure 3.1: a) Sketch of the experimental setup and imaging system. The laser propagates out of the plane of the page (indicated by the red cross) and can be translated in height using a motorized translation stage. b) X-ray tomogram of a convergent injector tip, cf. reference [17]. c) Picture of the operating injector in the vacuum chamber, showing the produced plasma during helium injection (recorded with a standard mobile phone camera).

each chosen such that no saturation occurs and the plasma is clearly visible. All other camera settings are kept constant during all measurements. A dark image (laser off) is taken for each exposure time and subtracted from the measurements. We then take the average of the background-corrected frames at a fixed exposure time and scale the intensity accordingly by dividing every pixel intensity by the known exposure time, increasing the effective dynamic range of our measurements. For calibration purposes we only consider the brightest central region of the produced plasma and take the average intensity of those brightest 100×50 pixels. The resulting calibration curve, i. e., the average intensity per pixel per millisecond exposure time ($I/\text{pix}/\text{ms}$) as a function of pressure, is shown in Figure 3.2. These calibration measurements are fit to a power law $I = A \times P^x + c$, shown as red line in Figure 3.2, to produce a continuous colorscale for subsequent measurements. Furthermore, the measured helium pressures can be converted into number densities; assuming ideal-gas behavior and room temperature, 1 mbar corresponds to $2.4 \times 10^{16} \text{ cm}^{-3}$.

To collect data from the injector produced plasma, the injector tip was installed in the center of the chamber and the upper chamber was pressurized with helium as discussed above. The horizontal laser-injector overlap, i. e., along the imaging axis, was optimized to produce the brightest plasma. Then the vertical position of the laser was adjusted by translating the focusing lens, such that it passed just below the injector tip. The laser focus was translated downwards in steps of $12.5 \mu\text{m}$ and at every point 20 frames were collected on the camera. The exposure time was adjusted such that the plasma was clearly visible but no saturation occurs. During the subsequent data analysis the images collected at the same position were averaged and scaled by exposure time.

A pressure map was then produced by comparing all images taken with identical upstream pressures and keeping for every pixel the maximum intensity value occurring in one of the images. This “maximum-intensity-stack” approach was chosen as the images cannot simply be averaged due to the long-lived nature of the plasma glow. This effect is clearly visible in the photograph in Figure 3.1 c. As the gas is moving rapidly away from the nozzle – due to choked-flow conditions the speed is probably close to 1000 m/s – glowing plasma is observed even several millimeters below the laser excitation. Simply

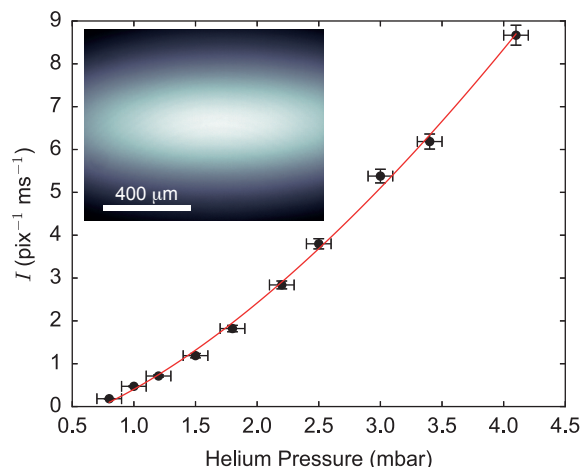


Figure 3.2: Calibration curve showing the the average intensity per pixel per millisecond exposure time of the most intense region of the plasma as a function of chamber pressure. The red line indicates a power law fit used to create a continuous pressure scale. Shown inset is an background subtracted image showing the plasma produced at 4.1 mbar of helium.

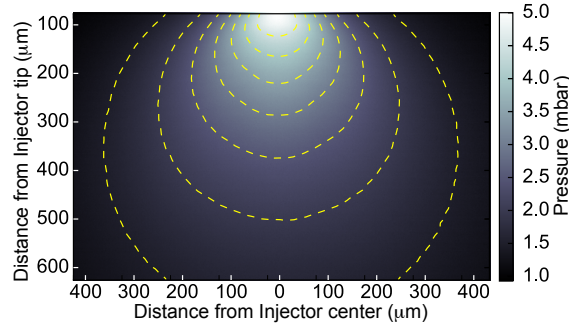


Figure 3.3: Pressure map recorded below the tip of a convergent injector nozzle for an upstream pressure of 800 mbar helium. Dashed yellow lines indicate isobars from 1.5 to 4.5 mbar in 0.5 mbar intervals.

averaging all images collected at different positions would therefore have overexposed the lower part of the image (since there is intensity in this part of the image even if the excitation happens far above). Following the combination of images, the pressure for every pixel was retrieved by comparison with the calibration measurements. The plotted isobars were obtained from the experimental data after applying a two-dimensional Gaussian filter with a width $\sigma = 4.3 \mu\text{m}$.

3.3 Results and Discussion

The measured pressure distribution from a convergent nozzle tip operated with 800 mbar of upstream helium is shown in Figure 3.3. Similar measurements for upstream pressures of 300 mbar and 500 mbar are shown in Figure 3.4. During the measurement the pressure in the main chamber was maintained below 2×10^{-2} mbar, ensuring choked-flow-conditions through the orifice. The topmost measurement was taken around $80 \mu\text{m}$ below the tip; moving the laser further up leads to clipping of the beam, and potentially damage, on the ceramic tip. At distances $\gtrsim 600 \mu\text{m}$ below the tip the pressure had fallen such that no plasma was observed. The gas pressure was found to decrease strongly with increasing distance from the injector tip, as expected. Due to the acceleration of gas inside the orifice, initially some propensity for the helium to continue along the axial direction is observed, rather than radially isotropic diffusion, resulting in the non-spherical pressure distribution measured. Under typical operating conditions for single-particle diffractive imaging experiments, the interaction region, that is, the crossing point of the x-ray beam with the particle stream, is located $\sim 300 \mu\text{m}$ below the injector tip. At this position the pressure has already dropped considerably and, for the measurements of 800 mbar upstream pressure, shown in Figure 3.3, is on the order of 3 mbar.

To quantify the spatial resolution in the produced images we differentiate between the resolution within the imaging plane, i. e., within the plane of laser illumination, and the resolution parallel to the camera surface. The latter is limited only by the imaging system employed. For the current setup a single pixel corresponds to $0.86 \mu\text{m}$ (as calibrated with a microscope reticle), however we estimate the resolution in this plane to be on the order of $2 \mu\text{m}$ due to aberrations and mechanical instabilities. In the direction perpendicular to the imaging plane, the resolution is not only limited by the depth of focus of the imaging system, but also by the focal spot size of the illuminating laser, which is around $50 \mu\text{m}$ (4σ) for the data shown. This is, however, still significantly smaller than the orifice size of the injector, allowing us to image essentially the central slice through the (radially symmetric)

pressure distribution.

Helium pressure profiles along both the axial and radial directions are shown in Figure 3.5, where the measured pressure has been converted into an absolute number density assuming ideal gas behavior. Figure 3.5 a shows the axial density distribution along the center line of the injector as a function of distance from the tip, for different upstream pressures. The pressure decreases rapidly with distance from the injector, and exhibits approximately a $1/r^3$ dependence, which is shown by the dashed lines in Figure 3.5 a, as would be expected for an isotropic radial diffusion in 3D. For the production of focused nanoparticle beams the pressure upstream of the injector is typically in the range of 200–500 mbar, while the particle focus – and hence interaction point – is located a few hundred micrometer downstream the nozzle [17]. Therefore, the corresponding number densities at the interaction point are typically on the order of $5 \times 10^{16} \text{ cm}^{-3}$. Radial profiles of the helium number density are shown in Figure 3.5 b, measured at various distances below the injector tip for an upstream pressure of 800 mbar; profiles for further upstream pressures are shown in Figure 3.6. These distributions were fit to Lorentzian functions and the good agreement shows, that the helium gas-flow has a uniform angular distribution. These results demonstrate that the initially narrow gas plume spreads out radially, leading to a rapid decrease in the absolute density along the center line.

To assess the total scattering signal that can be expected from helium in XFEL based

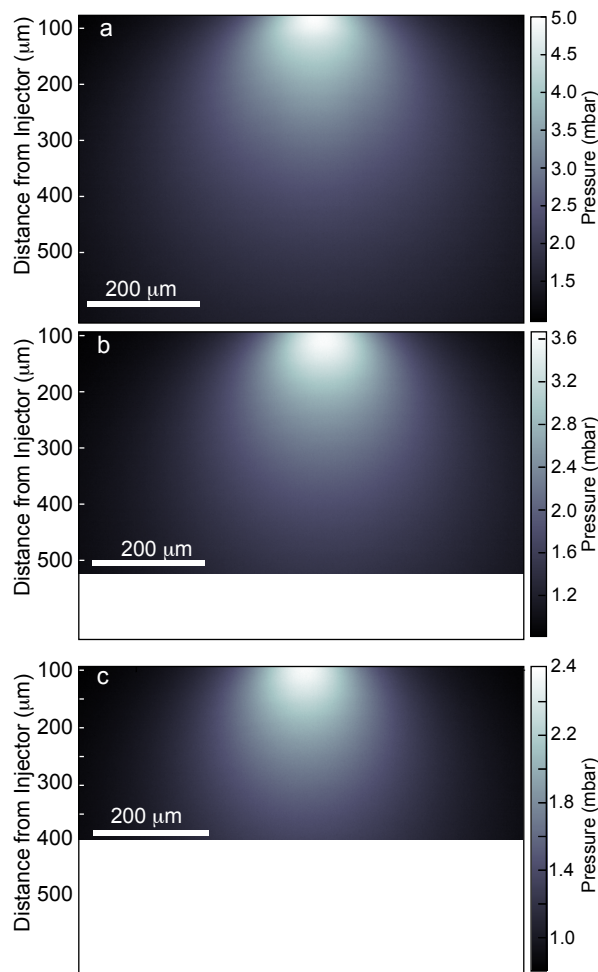


Figure 3.4: Spatial distribution of gas-flow from the injector tip with a) 800 mbar, b) 500 mbar, and c) 300 mbar upstream pressure; note the distinct intensity scales.

diffraction experiments, one has to take into account not only the interaction point itself, but due to the large Rayleigh length of the XFEL beam, typically several millimeters, one

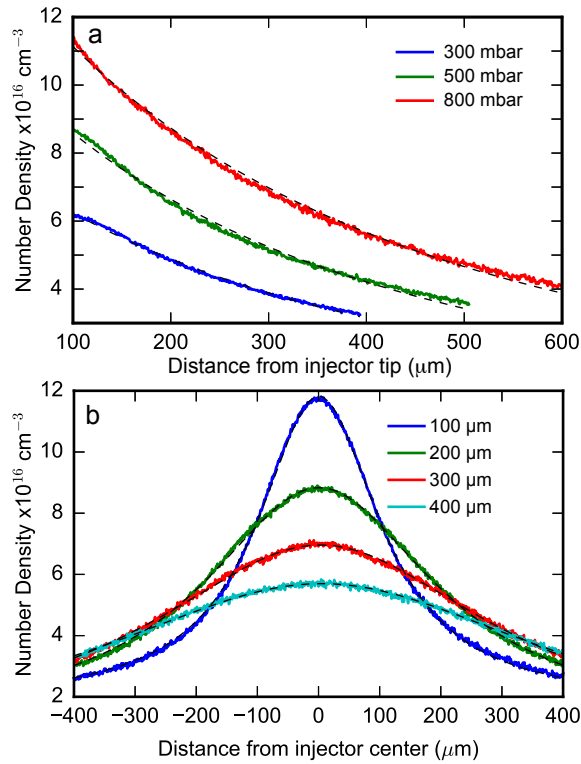


Figure 3.5: Gas density profiles. (a) Axial profile of the number density along the center of the injector as a function of distance from the tip, shown for three different upstream helium pressures. Dashed lines correspond to a $1/r^3$ fit. (b) Radial profiles of the number density across the generated plume for 800 mbar upstream pressure, at three different distances from the injector tip. Dashed lines correspond to a Lorentzian profile fit.

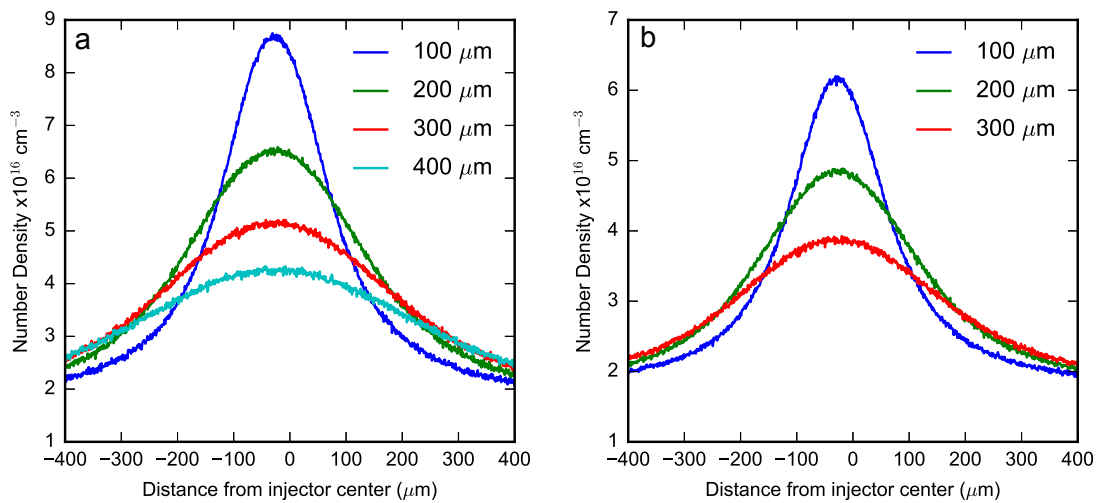


Figure 3.6: Radial pressure distribution at specified heights below the injector tip for a) 500 mbar and b) 300 mbar upstream pressure.

should take into account the full extend of the helium “cloud” along the x-ray beam, the extend of which is visible from the radial profiles in Figure 3.5 b. From our spatially resolved measurements we can assess the average helium density encountered by the XFEL pulse as it travels through the helium cloud, and for 500 mbar upstream pressure this is $\sim 3.6 \times 10^{16} \text{ cm}^{-3}$, corresponding to the average helium density 300 μm below the injector tip as measured within our field of view. Considering the known helium cross sections for elastic (Rayleigh) and inelastic (Compton) scattering, and typical operating conditions for the CXI endstation at the Linear Coherent Light Source (LCLS), e. g., 10 keV photon energy and 10^{11} photons per pulse, we expect a total of ~ 500 scattered x-ray photons per shot due to the helium background gas. Considering an isotropic scattering distribution and a detector opening angle of 60° , this corresponds to ~ 40 photons per shot on the detector. We furthermore note that the majority of these photons ($> 70\%$) originate from inelastic scattering processes, and can thus potentially be discriminated against by an energy-resolving detector [80].

3.4 Conclusion

We present a robust and sensitive approach for measuring the spatial distribution of gas flows from nozzles into vacuum. Calibration at known pressures allows the determination of absolute pressures and number densities with high spatial resolution. With the current setup the minimum detectable density is on the order of 10^{16} cm^{-3} , around one order of magnitude smaller than with interferometric approaches [78, 79]. The spatial resolution within the imaging plane is around 2 μm , perpendicular to the imaging plane it is limited by the laser spot size of 50 μm (4σ). We also note that this methodology can be further extended to measurements in the time domain, due to the inherently pulsed nature of the laser illumination.

We used this approach to assess the gas flow from a convergent nozzle injector [17] typically used for single-particle diffractive imaging experiments. We found that at typical operating conditions the gas density in the interaction region is on the order $5 \times 10^{16} \text{ cm}^{-3}$. By evaluating the average gas density encountered by an x-ray pulse as it travels through the gas plume we estimate that fewer than 500 photons will be scattered. This number could be further reduced by increasing the distance between the injector tip and the interaction region, which could be facilitated through the use of shallower convergence angles within the injector [17]. Further approaches to reduce the incoherent scattering from helium could incorporate inhomogeneous electric fields to deflect particles of interest out of the helium plume [81, 82], as has been demonstrated for single molecule scattering experiments at LCLS utilizing supersonic molecular beams [63].

4 Optimizing aerodynamic lenses for single particle imaging¹

A numerical simulation infrastructure capable of calculating the flow of gas and the trajectories of particles through an aerodynamic lens injector is presented. The simulations increase the fundamental understanding and predict optimized injection geometries and parameters. Our simulation results were compared to previous reports and also validated against experimental data for 500 nm polystyrene spheres from an aerosol-beam-characterization setup. The simulations yielded a detailed understanding of the radial phase-space distribution and highlighted weaknesses of current aerosol injectors for single-particle diffractive imaging. With the aid of these simulations we developed new experimental implementations to overcome current limitations.

4.1 Introduction

SPI is one of the key applications enabled by the advent of XFELs [11, 71]. Short-duration XFEL pulses were predicted to allow the collection of diffraction patterns from radiation-sensitive samples without resolution limitations due to radiation damage [4, 5], although some open questions remain [5, 68, 69]. A series of two-dimensional diffraction patterns of randomly oriented isolated particles can be used to reconstruct the full three-dimensional structure, without the need for large highly ordered crystalline samples [71, 73, 83].

As every intercepted particle is destroyed by the intense x-ray pulse [9], a new and preferably identical sample particle has to be delivered into every pulse. This can be achieved with aerosolized particle beams, which, furthermore, offer significantly reduced background levels compared to liquid jet based delivery methods [10, 12]. The most widespread aerosol injectors for SPI experiments are ALS [11, 13]. However, other aerosol injectors, e. g., convergent nozzles, have also been demonstrated [12, 14, 17]. One of the limiting factors for SPI is the collection of a sufficient number of strong diffraction patterns [7, 8]. Overcoming this limitation requires the delivery of high-density particle streams in order to maximize the number of x-ray pulses intersecting a particle and producing a measurable diffraction pattern. Using current aerosol injectors, hit fractions, i. e., the fraction of x-ray pulses that hit at least one particle, up to 79 % could be achieved [13]. However, this contains pulses interacting with multiple particles, faint hits far from the x-ray maximum intensity, as well as hits from background particles. This leads to hit rates, i. e., usable diffraction patterns containing a bright image from a single isolated target particle, of below 5 % and, hence, long measurement times and excessive sample consumption. Furthermore, these current studies have been undertaken with x-ray-focal-spot sizes on the order of a few micrometers. This comparatively soft focusing of the XFEL pulse does not yield the photon intensity required for measurable SPI diffraction signal to high scattering angles or from small samples [15]. This requires nanofocused x-ray beams with focal spot sizes on the order of 100 nm, where the hit-rate achievable with current aerosol injectors is typically below 0.05 %.

As particles distribute stochastically in the aerosol beam, the probability for them to be within the x-ray interaction volume depends on the local particle density, necessitating

¹This chapter is based on the publication: N. Roth, S. Awel, D. A. Horke, and J. Küpper, "Optimizing aerodynamic lenses for single-particle imaging," *J. Aerosol. Sci.* **124**, 17 (2018). I set up the simulation framework, performed the simulations, analyzed the simulated and measured data and wrote and discussed the manuscript.

highly collimated or focused particle streams. Robinson predicted in 1956 that in real, irrotational and incompressible gas flow past an obstacle, the density of small particles within the flow can increase while passing the obstacle [22]. This mathematical description was later extended and used, supported by numerical simulations, to describe particles flowing in a tube through an orifice [23]. Under the right conditions, in what is now known as an ADL, the particles concentrate at the center of the tube, as illustrated in Figure 4.1.

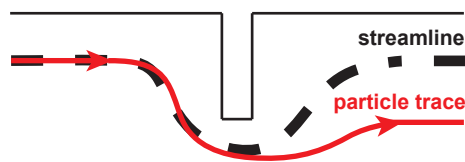


Figure 4.1: Schematic of particles being contracted toward the centerline by a gas stream through an orifice. The orifice is cylindrical symmetric around the dashed line. The trajectories of particles past the orifice vary from the streamlines due to particle inertia, leading to an aerodynamic lensing effect.

A detailed numerical characterization of an individual ADL was presented in 2002 [24], which was later extended to an entire ALS [25]. Numerical simulations for an ALS to focus particles with diameters below 30 nm [26] led to a simple design tool that predicts the required lens dimensions to focus a specified range of particle sizes at given flow conditions [27]. Based on this, further numerical simulations have adapted ALS to specific needs [28, 29]. Although ALS have been used for, e. g., ultrafast electron imaging experiments on nanoparticles [30], they are predominantly used in aerosol mass spectrometry [31]. Here, the main goal is to contract a large range of particle sizes and ensure a high transmission. The “Uppsala” ALS, a widely used standard injector for SPI [13], was designed based on the same principle. Therefore, it can deliver collimated particle beams for a large range of particle sizes (0.1–3 μm) without changing the apparatus. However, the possibility to optimize for a specific particle size is limited, and the pressure before the ALS is the only tunable parameter.

These design principles differ from the requirements of SPI experiments, where highly collimated beams of only one particular particle size are needed, and even desirable in order to increase sample purity. Additionally, the final particle beam diameter should be matched to the x-ray focal size. To enable the transmission of a wide range of particle sizes requires the use of several orifices within the ALS. This increases the complexity of the setup and the individual orifices are designed for different particle sizes, making some of them counterproductive for producing a high-density beam of a well-defined particle size.

Here, we present a detailed numerical simulation environment to understand and to quantitatively model the underlying fundamental processes occurring within an ALS and to further optimize these systems to meet the requirements of SPI experiments. In particular, we aim to design an ALS optimized for focusing a single particle size to the smallest possible beam diameter, while keeping the experimental setup simple and easily adaptable for different samples.

4.2 Methods

4.2.1 Numerical Simulation

Optimizing the geometry of an ADL requires investigating a large parameter space, such as dimensions of orifices and transport tubes, making experimental characterization and optimization impractical. Instead, we implemented numerical simulations to predict the behavior of particles within the ADL. Furthermore, these simulations allow the extraction of phase-space distributions of particles at any position within the device. Within all simulations we assumed that, (i) particles in the flow field have no influence on the flow field itself and (ii) particles do not interact with each other. This implies that the flow field and particle trajectories can be calculated separately, and that each particle can be simulated independently. These assumptions significantly reduce computational cost, and are easily justified considering the typical pressures in an ALS. The helium (or carrier gas) pressure is ~ 1 mbar (number density of $\sim 10^{16}$ atoms/cm³), while the density of particles usually does not exceed 10^{10} particles/cm³.

For an accurate description of the ALS and produced particle beams, the phase-space distribution of particles at the inlet of the injector is a crucial parameter. This distribution is typically defined by either the aerosol source or, more commonly, by a differential pumping stage used to reduce the gas-load and to control the pressure upstream of the ALS. A common arrangement for such a pumping stage is a set of two skimmers, oriented with the tips facing each other, as described in detail in subsection 4.2.2 and shown schematically in Figure 4.2. Since there is no experimental data available for the phase-space distribution of particles before they enter the ALS, the initial particle conditions are evaluated through simulations of the flow through the skimmers.

Flow field

We simulated the flow field of the carrier gas using a finite-element solver [62] to solve the Navier-Stokes equations. The geometry and flow were assumed to be axisymmetric about the central axis, and the flow solved in two dimensions (r, z). The flow was treated compressible and viscous, and the calculation iterated until converged to a steady-state solution. Additional properties of the flow field are indicated by three dimensionless quantities, the Reynolds number Re , the Knudsen number Kn , and the Mach number M . Re is defined as the ratio of inertial to viscous forces. Typically, Reynolds numbers in an ALS are below 10, indicating that no instabilities are present in the flow field, which we thus solve assuming laminar flow. Kn is defined as the ratio of the mean free path to a characteristic length. Inside the ALS the pressure is usually on the order of 1 mbar, corresponding to a mean free path around 70 μm for helium at room temperature. Compared to the dimensions of apertures (a few mm) this results in $Kn < 0.01$ and there are enough collisions with the background gas to treat the flow as continuum and the Navier-Stokes equations hold. Upstream of the ALS, before and throughout the two skimmer setup, the pressure is even higher, hence $Kn \ll 0.01$. In the vacuum chamber, on the other hand, at helium pressures of 10^{-2} mbar or less, the mean free path is around 10 mm, hence $Kn > 0.01$, and the continuum flow model breaks down. With such a large mean free path particles rarely collide with the background gas, such that there is no momentum exchange with the flow field anymore. In between these regimes there is a transition region which is difficult to model. However, this transition between regimes occurs rapidly after particles exit the tip of the injector, and here we assumed a sudden stop of the continuum flow regime and an immediate change to the molecular flow regime. In the latter, particles were assumed to propagate collision-less and with constant velocity.

The ratio of the velocity of the flow to the speed of sound in the fluid is the Mach number, Mi . For $Mi > 0.3$ effects due to the compressibility of the fluid start to occur, such as pressure waves and cooling of the fluid. Here, such high Mi are reached between the two skimmers and downstream of the injector tip. Pressure waves are still properly described by the Navier-Stokes equations. However, our numerical simulation approach, finite element methods, necessitates the use of stabilization methods, which add artificial diffusion in order to avoid numerical instabilities, e. g., oscillations in the solution. While these might wash out the position and velocity of the potentially occurring pressure waves, the position of the second skimmer is closer to the first skimmer exit than the calculated distance of the Mach disc, where these pressure waves are supposed to be located. In Addition, downstream of the injector tip and between the two skimmers particles are fast and have a high inertia. Hence, the effect of the spiky features caused by high Mi are assumed to have a limited influence on the overall particle trajectories, especially at the injector tip, where the continuum flow breaks. Nevertheless an accurate treatment of the flow including thermodynamic coupling might be able to further improve the simulation results.

Particle traces

Particle trajectories were simulated, within a given steady-state flow field, with a homebuilt `python` code that uses a real-valued variable-coefficient ordinary-differential-equation solver. The code interpolates the given pressure and velocity fields and calculates the forces, described by Stokes' law, acting on a particle of given size at each time step. Additional corrections can arise depending on the particle's Reynolds (Re_p) and Knudsen (Ki_p) numbers. These are defined identical to the fluid case, but with the characteristic length given by the particle diameter. Re_p is very small inside the lens ($Re_p < 1$) and can be neglected. Ki_p , however, cannot be ignored as at low gas densities the mean free path is larger than the particle diameter, leading to a decreased drag force due to the reduced number of collisions. This is taken into account by the Cunningham slip-correction factor C_c [84], which gives the drag force as

$$F_{\text{drag}} = \frac{3\pi\mu d_p(\mathbf{U} - \mathbf{u})}{C_c} \quad (4.1)$$

$$\text{with } C_c = 1 + Ki_p(c_1 + c_2 \cdot e^{c_3/Ki_p}) \quad (4.2)$$

Here, \mathbf{U} is the local velocity of the flow field, \mathbf{u} the particle velocity and d_p the particle diameter. The empirical coefficients $c_1 = 1.2310$, $c_2 = 0.4695$ and $c_3 = -1.1783$ are taken from the literature [84]. This model describes the interaction of a particle with a continuum flow field. In reality, however, the particles interact *via* single collisions with the carrier gas. This leads to diffusion and an additional random walk of the particles around their trajectory. This is numerically described by a Brownian-motion force F_b , which is added to the drag force [85]

$$F_b = m_p \mathbf{G} \sqrt{\frac{\pi S_0}{\Delta t}} \quad \text{with} \quad S_0 = \frac{216\mu kT}{\pi^2 d_p^5 \rho_p^2 C_c'} \quad (4.3)$$

where \mathbf{G} is a vector of zero mean, unit variance, independent Gaussian random numbers, Δt the time step size of the solver, k the Boltzmann constant, T the temperature of the carrier gas, m_p the particle mass, d_p the particle diameter and ρ_p the particle density. Since the flow field was treated axisymmetrically, the Brownian force was restricted to have axial

and radial components. Particle trajectories are calculated until they reach the boundary of the flow field. This happens either when they are successfully transmitted to the end of the flow field downstream of the geometry or when they touch the wall of the geometry and are considered lost due to impaction.

4.2.2 Experimental Setup

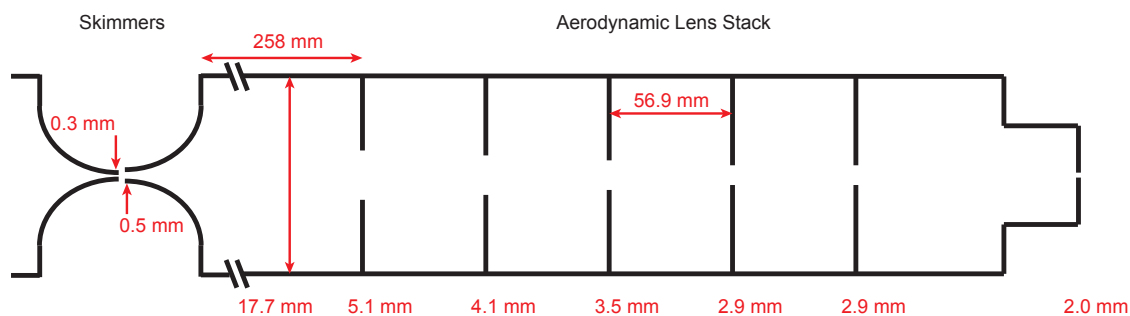


Figure 4.2: Sketch (not to scale) of the double skimmer setup and the ALS injector with its 6 orifices. The dimensions given below the orifices refer to the inner diameter.

To validate our simulations and the ability to predict ALS behavior, we benchmarked them against experimental data. The experimental setup and data analysis has been described in detail previously [14]. Briefly, we used a GDVN to aerosolize an aqueous solution of 500 nm sized polystyrene spheres (Thermo Fisher Scientific) into a nebulization chamber [10, 86]. Particles then passed a set of two skimmers, with inner diameters of 0.3 mm and 0.5 mm, respectively, placed 2 mm apart, as sketched in Figure 4.2. Evacuating the volume between the skimmers allows control over the pressure before the ALS while minimizing particle losses. After the ALS particles were illuminated with a Nd:YLF laser (Spectra Physics Empower ICSHG-30, 527 nm, pulse duration 100 ns, pulse energy 20 mJ) and scattered light collected on a translatable high-frame-rate CMOS camera (Photron SA4) using a $5\times$ infinity-corrected objective (Mitutoyo, numerical aperture 0.14). The geometric dimensions of the ALS used are specified in Figure 4.2.

4.2.3 Theoretical description of the experimental setup

For the theoretical model, we first calculated flow fields within which particles are then propagated. When trying to simulate the entire apparatus, containing differential-pumping skimmers and the ALS, we encountered convergence problems and no steady solution was found. Therefore, we retreated to evaluate the flow fields for the ALS and the skimmer setup separately, but made sure that they are consistent.

The effect of the skimmers was approximated by simulating the flow field through the upper skimmer, simulating particle trajectories and retaining only particles with a radial position smaller than 250 μm at a position 2 mm downstream of the skimmer tip, representing those that would enter into the second skimmer. The purpose of the upper skimmer is to accelerate particles, such that their momentum is high enough to enter the lower skimmer without being significantly disturbed by the flow field between the skimmers, where excess gasload is evacuated. Boundary conditions constrained the inlet mass flow through the skimmer to 30 mg/min, comparable to experimental conditions. The outlet was defined as a semi-circle at the tip of the skimmer with a 2 mm radius, corresponding to the distance between the skimmers. Along this semicircle the pressure

was constrained to experimentally measured values. Particles were assumed to be spheres with 500 nm diameter and a density of 1050 kg/m^3 (polystyrene), with an initial uniform distribution at the entrance plane of the skimmer. The longitudinal and radial velocities of the particles are set to the flow velocity at their initial position. The recorded final phase-space distributions of transmitted particles are used to define the initial particle phase-space distribution at the ALS.

To simulate the ALS we introduced boundary conditions for the pressure at the inlet and outlet. The former was defined as the entrance plane at the beginning of the ALS tube, and pressures set to experimental values. The outlet was defined as a semi-circle at the tip of the ALS into vacuum with radius 1 mm, corresponding to the radius of the final aperture of the ALS. The pressure along this semicircle was assumed to be 10^{-2} mbar. Reducing this pressures further does not change the dynamics in the flow, since they depend on pressure difference, which is already dominated by the two-orders-of-magnitude higher pressure inside the ALS. With these boundary conditions we calculated a steady flow field for every inlet pressure. The initial phase-space distributions of particles were taken from the skimmer simulations, but with the initial longitudinal position of all particles set to the entrance plane at the beginning of the ALS tube.

We simulated 10^5 particles per upstream pressure. Final particle trajectories contain the axisymmetric two dimensional position of particles throughout and after the ALS. In the experiment, we probed the particle beam orthogonal to the propagation direction by projecting it onto the imaging plane of a camera [14]. Hence, the simulated radial particle beam distribution was projected *in silico* onto a two dimensional imaging plane for comparison.

4.3 Results & Discussion

4.3.1 Validation against literature simulations

We first validated our simulation environment against the simulations by Wang et al. [27]. We replicated the geometry and conditions of the original publication and simulated particle trajectories. Figure 4.3 shows the local gas velocity and pressure as well as the velocity of 1, 10 and 40 nm particles along the centerline of the ALS. Our results show excellent agreement with the previously published simulations, cf. Figure 2b of reference [26], and only deviate slightly in the region outside the actual ALS ($z > 7$ cm). These deviations can be explained by the different outlet boundary conditions.

4.3.2 Particle Beam Characterization

Experimental Results

All measurements were conducted with the setup described in subsection 4.2.2, and the only parameter varied was the pressure upstream of the ALS. The particle stream was imaged 8 mm downstream of the injector tip and data collected for ~ 10 min at each pressure, corresponding to $\sim 10^5$ imaged particles. For comparison with theoretical results, we determined the particle beam width containing 90 % (70 %) of all particles, denoted D_{90} (D_{70}). Measured beam widths are shown in Figure 4.4 a for upstream pressures in the range 0.66 to 2.0 mbar.

The full distributions for three characteristic pressures are shown in Figure 4.4 b–d (black lines). It is evident from the experimental data that the particle beam width decreases with increasing upstream pressure until a critical value, here ~ 1.2 mbar, after which no

dependence on pressure is observed anymore and the produced beam width remains practically constant.

Theoretical Results

In order to simulate the resulting particle beam downstream of the ALS, it is necessary to compute the initial phase-space distribution of particles entering the ALS by simulating the first skimmer as detailed above. An example of a velocity field inside and such a radial phase-space distribution of particles after the first skimmer is shown in Figure 4.5 a and b, respectively. The radial position is cut at $250\ \mu\text{m}$, as only these particles enter into the second skimmer. A large fraction of particles is contained within a small region of phase space at radial velocities between 10 and 15 m/s.

Simulated radial phase-space density distributions of particles through the flow-field shown in Figure 4.6 at various positions within the ALS are displayed in Figure 4.7 for two different upstream pressures. The left hand side of Figure 4.7 corresponds to 0.66 mbar and the right hand side to 2.0 mbar. The top images show the initial distribution (beginning of the injector), while all others contain only successfully transmitted particles, which are shown at three positions; at the beginning of the ALS (c and d), just before the first ADL (e and f), 1 mm after exiting the ALS (g and h) and at the particle focus 10 mm and 5 mm after exiting the ALS, respectively (i and j). Whereas the initial phase-space distributions of particles are nearly identical for the two pressures, the number of particles transmitted and their phase-space distributions throughout and after the ALS are markedly different.

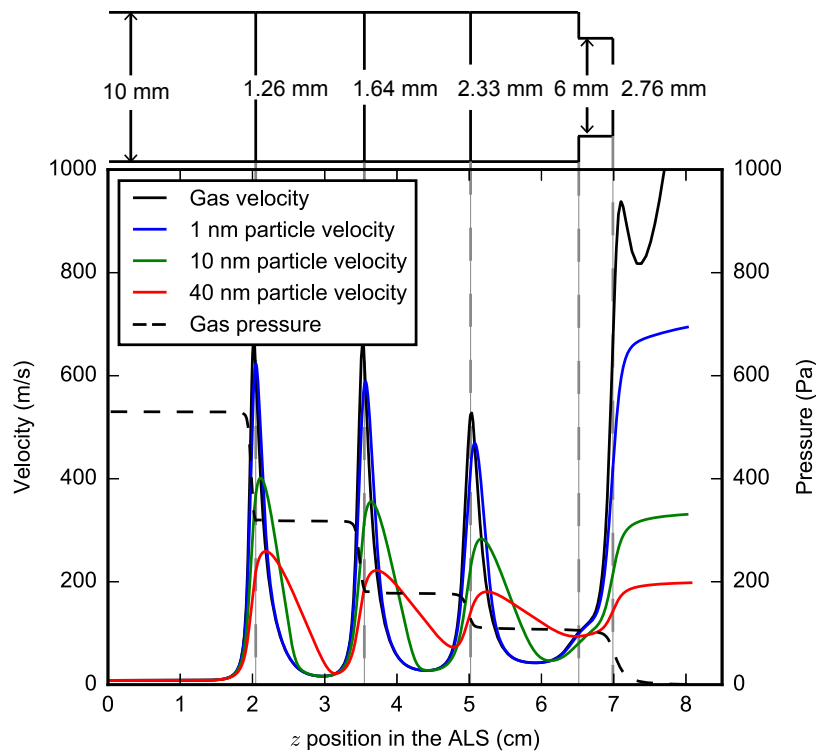


Figure 4.3: Simulation of gas pressure, gas velocity and particle velocity of 1, 10 and 40 nm particles along the centerline of the ALS investigated in [26], and shown at the top of the figure. Our simulation accurately reproduced the results from the original publication [26, Figure 2].

While for high P_u all particles are transmitted, this is not the case at low P_u . Here, the initial phase-space distribution of successful transmitted particles exhibits a cutoff at around 6 m/s absolute radial velocity (Figure 4.7 c). We rationalize this with the pressure scaling of the drag force. Particles at lower pressures, and hence lower drag force, are not slowed down sufficiently in the radial direction, such that they collide with the wall of the ALS tube and are lost. This is not the case at $P_u = 2$ mbar, where all particles are slowed

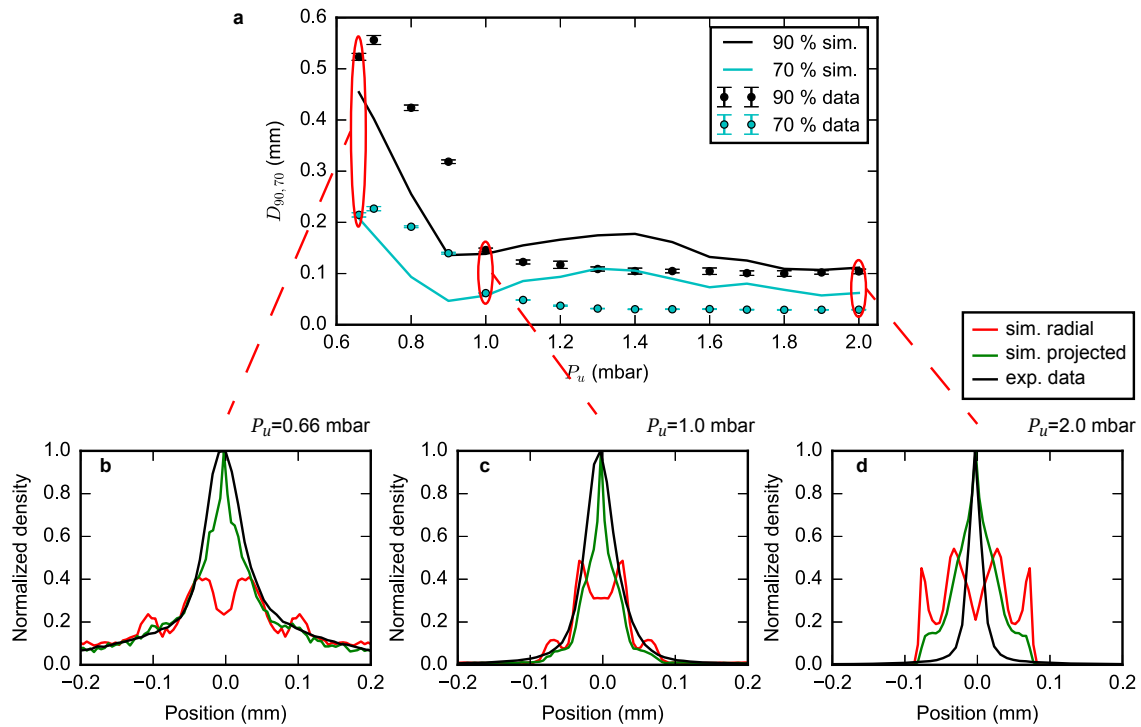


Figure 4.4: Comparison of experimental, i. e., projected, and simulated, i. e., projected *in silico*, beam width for 500 nm particles as a function of inlet pressure P_u . The errorbars represent the statistical standard error (a). Comparison of experimental, i. e., projected (black line), simulated radial (red line), and simulated projected (green line), particle profiles for three distinct upstream pressures of the ALS, 0.66 mbar (b), 1.0 mbar (c) and 2.0 mbar (d).

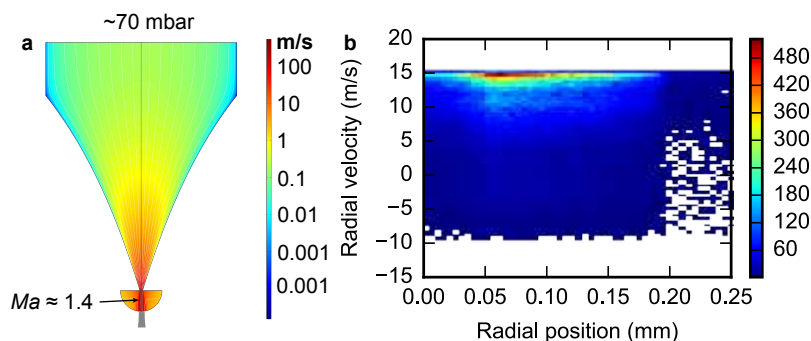


Figure 4.5: Simulated flow field with streamlines inside the upstream skimmer. The logarithmic color scale corresponds to the flow speed. The grey area indicates the position of the lower skimmer. (a). Histogram of the radial position and velocity of particles 2 mm downstream from the skimmer tip (b).

down before they reach the wall and are transmitted. The radial velocity of the particles before the first lens is now essentially zero and most particles lie within ± 0.02 m/s. The phase-space densities in Figure 4.7 e and f show that particle radial positions are spread over the entire ALS tube, and that at higher pressures (f) the majority of particles are at large radii. These particles at large radial positions correspond to those with an initially large radial velocity. In the low pressure case (e) high-radial-velocity particles collided with the wall and were lost. This correlation between initial radial velocity and radial position is, furthermore, evident for the low pressure case (Figure 4.7 c and e), where an initially empty area of velocity space (between 4 and 5 m/s) appears as an empty area in position space (around 7 mm) before the first ADL. Thus the acceptance of the ALS depends on the upstream pressure, i. e., the flow field, and in the low pressure case the transmission and behavior of the ALS depend critically on the radial particle position before the first ADL, hence the initial radial particle velocity. This position-dependent behavior of an ADL will be further investigated in subsection 4.3.3.

In both pressure regimes the distribution of final radial positions (Figure 4.7 g and h) is concentrated toward the centerline in comparison to the distribution before the first lens (Figure 4.7 e and f) and the final radial velocity distribution is narrower, hence, the particle beams are more collimated than the inlet distributions (Figure 4.7 a and b). However, in the high pressure case particles are confined to significantly smaller radii corresponding to $D_{70} = 226$ μm at this position in comparison to $D_{70} = 815$ μm for the low pressure case. The particles radial velocity is predominantly negative after the lens, corresponding to a motion toward the centerline, i. e., the particle beam converges. Particles at higher radial positions have a greater negative radial velocity and, therefore, a higher density of particles will be achieved downstream of the injector. In the 0.66 mbar case the highest density is achieved 10 mm after the injector outlet, while for 2 mbar it is 5 mm downstream of the outlet. The corresponding phase-space distributions are shown in Figure 4.7 i and j. Note that from 1 mm downstream of the injector (the end of the calculated steady-state flow field) onwards the particles are propagated straight without any forces acting on them.

The final phase-space distribution is predominantly defined by the last aperture, as the radial velocity upstream of each ADL is centered around 0, see Figure 4.7 e and f. In order to qualitatively rationalize the observed distributions we consider the radial-position

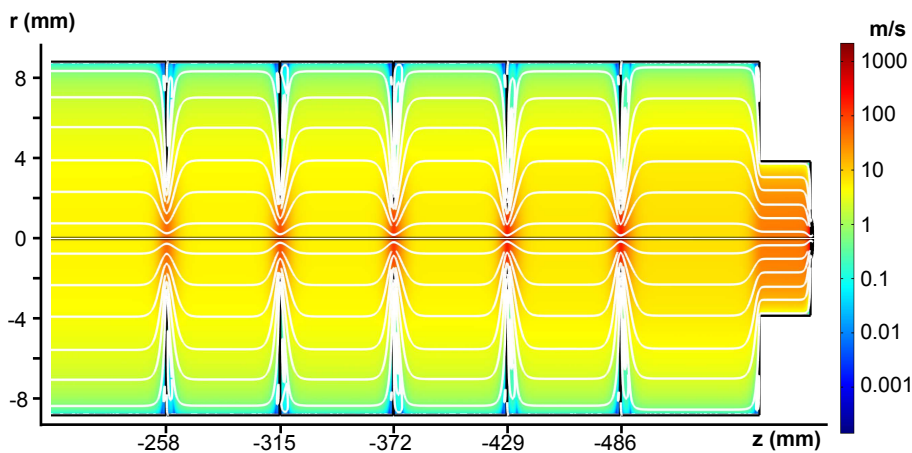


Figure 4.6: Simulated flow field with streamlines inside the ALS injector. The r -axis has been scaled by a factor of 10. The logarithmic color scale corresponds to the flow speed.

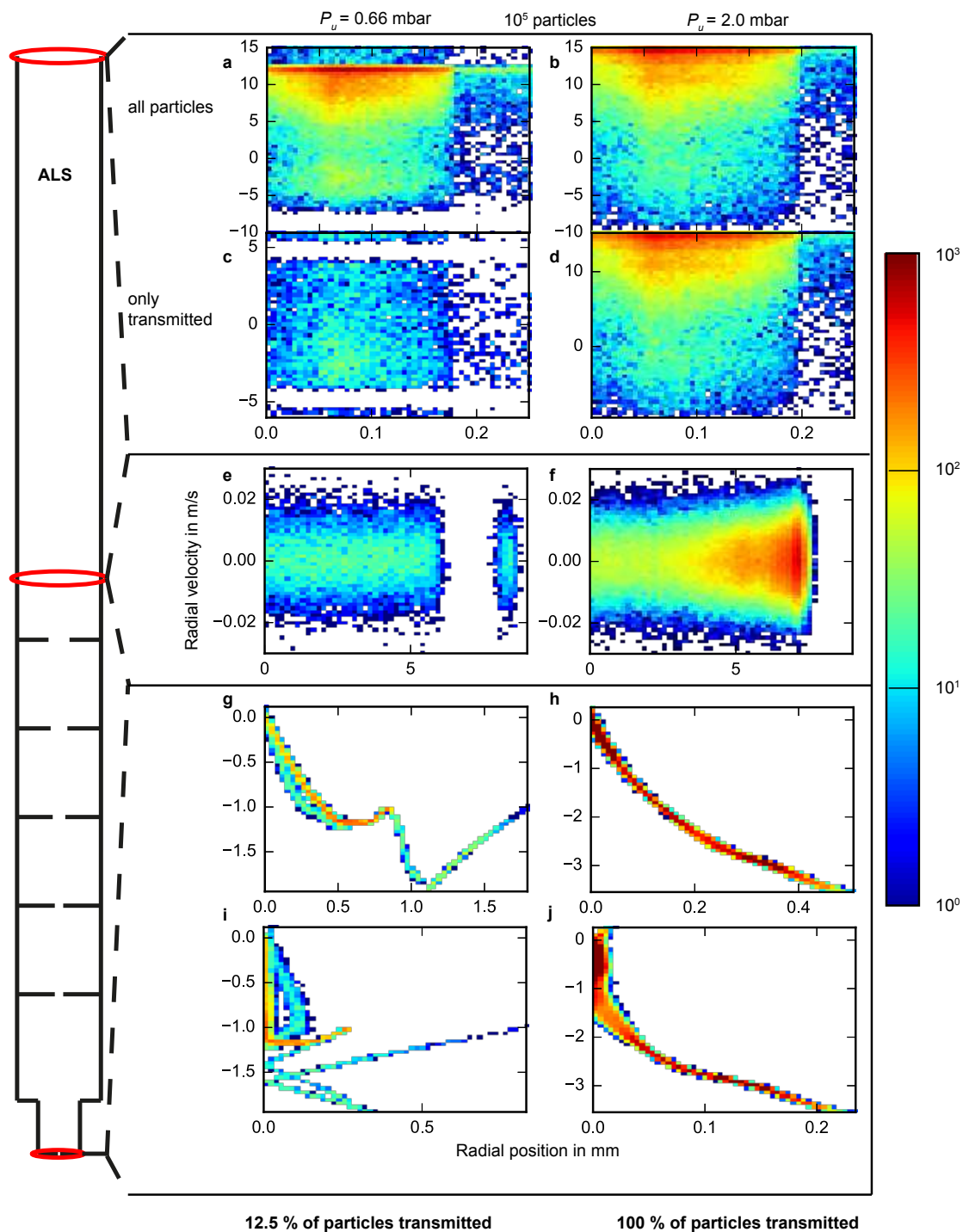


Figure 4.7: Histograms of the radial phase-space distribution for 500 nm particles at various positions in the ALS for $P_u = 0.66$ mbar (a, c, e, g, i) and $P_u = 2.0$ mbar (b, d, f, h, j). a, b show the distributions for all particles at the inlet of the ALS. All other distributions show only particles successfully transmitted through the ALS and are taken at a position at the inlet (c, d), before the first lens (e, f), after the ALS (g, h) and at the distance of highest density, 10 mm (i) and 5 mm (j) downstream of the outlet, as indicated by the red lines.

dependence of the radial velocity and total speed of the gas flow before (Figure 4.8 a) and after (Figure 4.8 b) the last lens in the ADL. The radial velocity of the flow changes throughout the orifice, from a contraction towards the centerline, i. e., negative radial velocities in Figure 4.8 a, to an expansion afterwards, positive radial velocity in Figure 4.8 b. This dramatic change is caused by the significantly different pressure regimes, inside the ADL *versus* outside the ADL. Since the drag force is proportional to the difference in particle velocity and flow field velocity, see (4.1), the force acting on a particle in the radial direction is proportional to the radial flow velocity. In Figure 4.8 c we show the particle phase-space distribution before the last orifice, i. e., at the same position as the gas flow distribution shown in Figure 4.8 a. A clear correlation is observed between the radial gas-flow velocity, blue line in Figure 4.8 a, and the particle phase-space distribution. As the radial velocity of the gas is changing rapidly on passing the orifice, one might expect a similar effect on the radial velocity distribution of particles. However, since particles carry a significant amount of inertia, they cannot follow this rapid change in gas-flow and the particle phase-space distribution even after the last aperture (as shown in Figure 4.7 g) is still dominated by the distribution *before* the orifice. One noticeable difference, however, is an increase of radial velocity around the position 0.8 mm. We attribute this to the rapid expansion of gas after the last aperture, which peaks at this radial position (Figure 4.8 b) and, hence, accelerates particles most at this distinct radius, leading to the observed local maximum in the particle radial velocity around 0.8 mm.

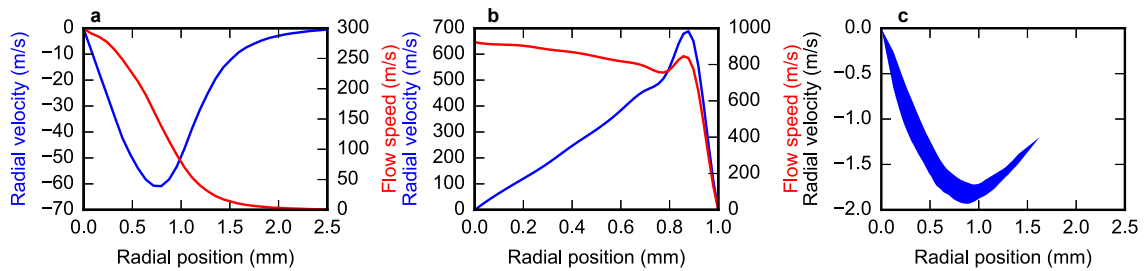


Figure 4.8: Radial velocity and speed of the helium flow as a function of radial position for 0.66 mbar upstream pressure at a position 0.2 mm before (a) and 0.5 mm after (b) the last orifice in the ALS injector. Phase-space distribution of 500 nm particles 0.2 mm before the last orifice in the ALS injector at a 0.66 mbar upstream pressure (c).

Where within the general shape of the phase-space distribution particles are located (i. e., the intensity information missing in Figure 4.8 c) is dependent on the radial position of particles upstream of an ADL. Since, in the high pressure case, no particles are at radial positions above ~ 0.5 mm, only the initial falling edge at small radial positions is represented in the phase-space distribution in Figure 4.7 h.

Comparison of Simulation and Experiment

We compared the simulated results with experimental data by reproducing the pressure dependence of the particle-beam width evaluated 8 mm downstream of the ALS tip, as shown in Figure 4.4 a. The simulations clearly reproduced the experimental observation, with a sharp drop in beam diameter as the pressure is increased, until a plateau is reached at ~ 0.9 mbar. Full radial distributions of particles are shown in Figure 4.4 b–d for three inlet pressures and exhibit an overall good agreement with the experimental data. Some deviations are, however, observed. A slight pressure offset for the location of the sharp

drop is most likely due to the $\pm 15\%$ uncertainty of the pressure gauges used (Pfeiffer Vacuum, TPR 280). Moreover, the simulations overestimate the particle beam size in the plateau region, which could be due to the limited illumination area of the laser used for particle detection [14]. If particles far from the center were not correctly identified, this would lead to lower than expected experimental values for D_{70} and D_{90} . On the other hand, for very high particle densities, there is a probability that the image analysis software cannot distinguish individual particles anymore. This would lead to a decreased particle density detected in the central region.

We also note that our simulation might oversimplify the occurring physical processes, e. g., particles are assumed to have no collisions 1 mm downstream of the last aperture, whereas there are some experimental indications that particles still accelerate in this region [87]. In addition, the used Cunningham correction factors, see Section 4.2.1, were derived for air instead of helium. While this might render it difficult to computationally reach high accuracy, the overall good agreement justifies the use of these models, and our simulation infrastructure in general, to understand and predict ALS behavior.

4.3.3 Radial distribution analysis

In SPI experiments the interaction volume is a cylinder, representing the x-ray beam volume, through the three dimensional particle beam. Therefore, the vast majority of particles with a radial position greater than the x-ray spot will not interact with the photons. The radial particle distributions in Figure 4.4 b–d (red lines) show that, additionally to the main peak, smaller outer secondary maxima are present, which reduce the number of particles contained within the interaction volume. The formation of these “wings” has also been observed in other studies of particle distributions from ALS [88, 89], but no explanation as to the source of this effect was given.

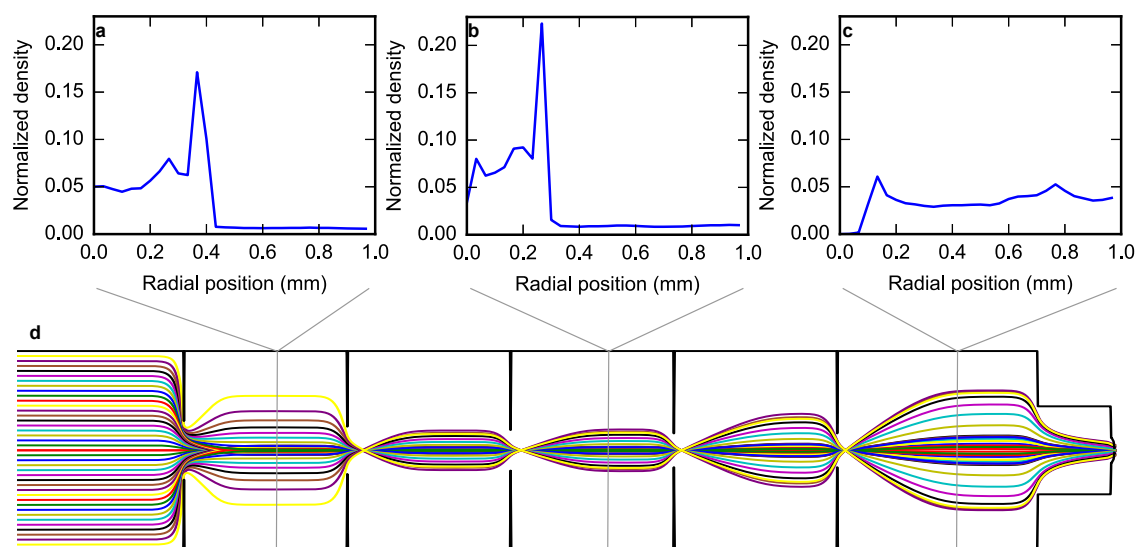


Figure 4.9: Radial distributions of 500 nm particles at different stages inside the ALS injector for a uniform initial radial distribution (a–c). The formation of a peak at large radii (i. e., a “wing” in the particle distribution) is already evident after the first lens (a). Example trajectories of 500 nm particles through the ALS injector, without diffusion effects (d).

To investigate this, we considered the radial distributions of particles within the ALS and

show these after the first, third, and fifth lens in Figure 4.9 a–c, respectively. These were simulated for 2 mbar inlet pressure and 0.31 mbar downstream pressure, with particles evenly distributed at the inlet and neglecting Brownian motion. Example trajectories through the entire ALS are shown in Figure 4.9 d. It is immediately evident that an outer maximum in the radial distribution is already present after the first lens, and that not all lenses are contracting the particle beam, with some even broadening the distribution. These effects are due to the design of this ALS to accept a large range of particle sizes. In order to visualize the origin of the outer radial maxima we considered particle trajectories through the first lens for different radial starting positions, Figure 4.10.

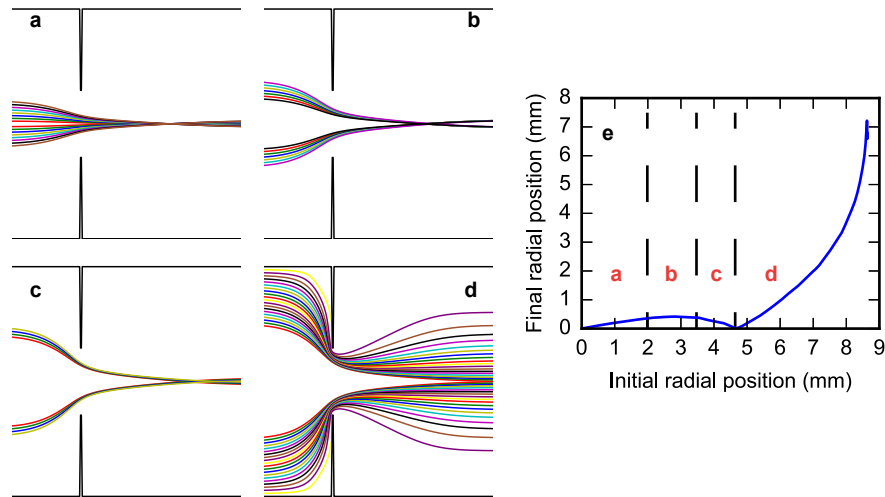


Figure 4.10: Trajectories of 500 nm particles through the first lens of the ALS injector, for different radial starting positions of 0 – 2 mm (a), 2 – 3.5 mm (b), 3.5 – 5.0 mm (c) and 5.0 – 8.8 mm (d). Correlation between initial and final radial position for particles traveling through the first lens (e). We identify four distinct regions, as exemplified by the trajectories in a–d.

A particle exactly on the centerline of the ADL simply stays there, as it feels no radial force, see Figure 4.8 a. The further off-center the particle is located, the larger the curvature of the flow toward the centerline, leading to a larger radial force. This leads to particles with initial radial positions between 0–2 mm (Figure 4.10 a) getting pushed towards the center. Due to their inertia particles cross the centerline, but remain closer to it than initially, i. e., the beam is contracted and larger initial radial positions lead to larger final radial positions.

Further away from the centerline the curvature of the flow still increases, while flow speed decreases with proximity to the outer wall (see Figure 4.8 a). These counter-acting mechanisms negate each other for particles with initial radial positions between 2 and 3.5 mm (Figure 4.10 b) and in this region all particles arrive at approximately the same final radial position, regardless of their initial radial position.

Increasing the initial radial position even further (3.5 to 5.0 mm, Figure 4.10 c) leads to the decreasing flow speed dominating and final radial positions get closer to the centerline with increasing initial radial position, i. e., the opposite effect to that observed in Figure 4.10 a.

Eventually, at around 5.0 mm (Figure 4.10 d), trajectories stop crossing the centerline and the final radial position increases with increasing initial radial position again. This overall behavior is also summarized in Figure 4.10 e, showing the radial position after the first lens as a function of the initial radial position. The secondary maxima observed in the

radial distribution in Figure 4.4 thus arise at the turning point in b, where several initial radial positions result in the same final position, hence leading to an increased particle density at distinct radii.

This undesirable behavior can be mitigated by designing an ALS such that it only operates in either one of the regimes corresponding to Figure 4.10 a or d. Total avoidance of secondary maxima can only be accomplished by operating exclusively in regime a, which would – conceptionally – be the best solution to this problem. However, it is experimentally impractical, because it requires an ALS tube much larger than the radial size of the incoming particle beam. Designing a lens such that crossing of the centerline is minimized would ensure that more particles, including those at small initial radii, will be in the regime d, producing a more collimated particle stream at the output, with fewer particles in secondary maxima, but also with a reduced amount of focusing. This can be achieved by increasing the orifice diameters of the ADL for a given mass flow. This way the absolute value of the derivative of the radial velocity of the gas flow before the orifice with respect to the radial position decreases, while the flow speed drop caused by the walls remains the same. Hence, the radial velocity minimum has an increased value and its position changes to smaller radii, i. e., the minimum in Figure 4.8 a moves to the upper left. The regimes a–c are moved towards smaller radii until they get negligible. This is

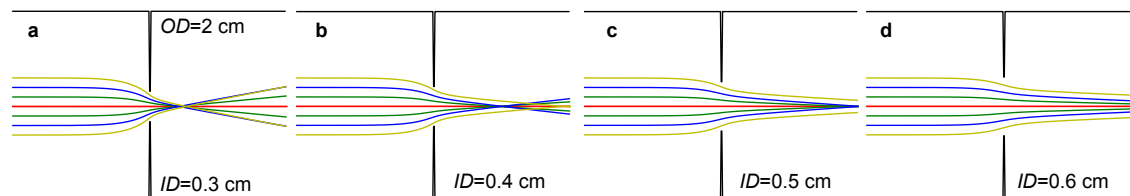


Figure 4.11: Simulated trajectories of 500 nm particles through an ADL with an outer diameter of 2 cm and an inner diameter of 3 mm (a), 4 mm (b), 5 mm (c), 6 mm (d). The pressure downstream of the ADL is 0.5 mbar and the mass flow of carrier gas is $1.2 \cdot 10^{-2}$ mg/min.

highlighted in Figure 4.11, showing particle trajectories through lenses with various inner diameters for an identical mass flow. Increasing the orifice diameter shifts the crossing point of trajectories further away from the lens and a more collimated particle stream is produced (Figure 4.11 d). Thus operation in regime d is readily achievable, but the corresponding effects of stronger collimation and weaker focusing requires more ADLs for reaching high densities. Balancing these effects for a limited amount of ADLs in the ALS, secondary maxima will not completely be avoided when maximizing the central particle density.

Figure 4.12 shows a three-lens-system for focusing 500 nm particles that way. Figure 4.12 a–c shows radial distributions of 500 nm particles at various positions within the new ALS, demonstrating that particles are smoothly collimated toward the centerline with significantly weaker secondary maxima than for the conventional ALS in Figure 4.9. To compare the particle beams of the optimized and the "Uppsala" ALS, we evaluated the fraction of particles arriving within a given radius at the respective particle beam foci, 4.6 mm and 0.5 mm downstream for the "Uppsala" and optimized injector, respectively; see Figure 4.13. The optimized ALS exhibits a much steeper increase of the integrated particle fraction at small radii, i. e., focusing a significantly larger fraction of particles into a given radius. As discussed above, secondary maxima cannot be avoided completely in the improved ALS, leading to a kink in the fraction of particles contained around a radius of $\sim 0.5 \mu\text{m}$. In SPI experiments, it is especially pertinent to compare the fraction

of particles that would cross the interaction volume with the x-rays. For an x-ray focal spot size with a radius of $0.5\ \mu\text{m}$, in the current lens design only 17.1 % of the particles are contained within that radius, while in the optimized design this increases to 48.5 % — corresponding to a nearly threefold improvement. At the same time, the final particle density in the interaction volume also depends on the velocity of the particles leaving the injector. With lower velocities the particles are “packed” closer in the z dimension and the density is correspondingly higher. For the optimized injector the mean final particle velocity is 43.8 m/s, whereas for the “Uppsala” injector it is 57.9 m/s. This leads to a velocity weighted density within the $0.5\ \mu\text{m}$ radius spot that is higher by a factor of ~ 4 for the optimized injector; for an x-ray focal spot size of $50\ \text{nm}$ radius it would even be higher by a factor of ~ 9 . While the simulated increase in particle density might not be quantitatively accurate, since this simulation was not taking into account particle diffusion or the skimmer setup, which could significantly influence the final particle beam, see

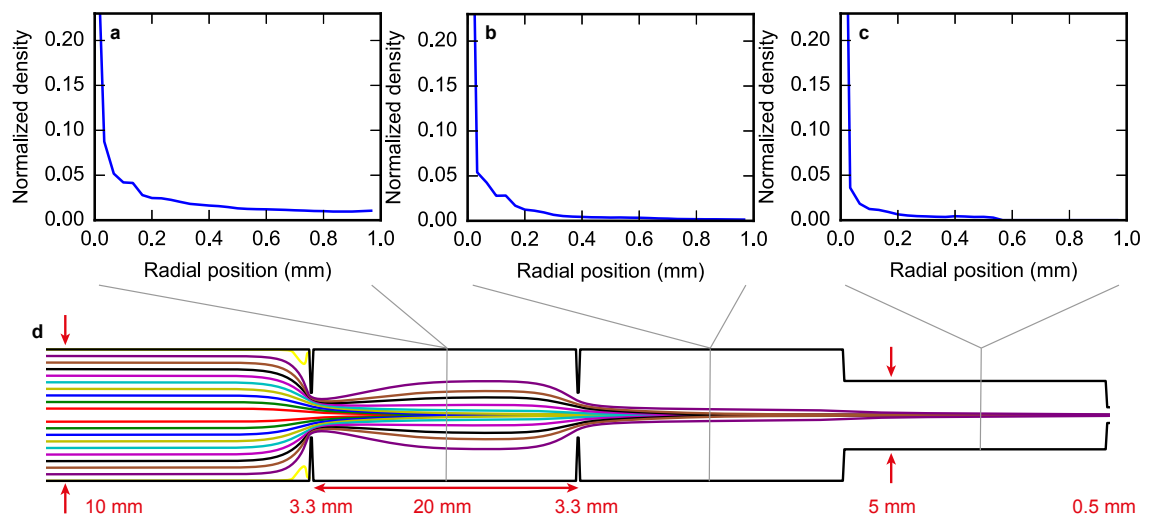


Figure 4.12: Radial distributions of 500 nm particles at different stages inside an optimized ALS injector (a-c). The formation of peaks at large radii (i. e., a “wing” in the particle distribution) is significantly reduced in comparison to the conventional ALS in Figure 4.9. Example trajectories of 500 nm particles through the optimized ALS injector, without diffusion effects (d).

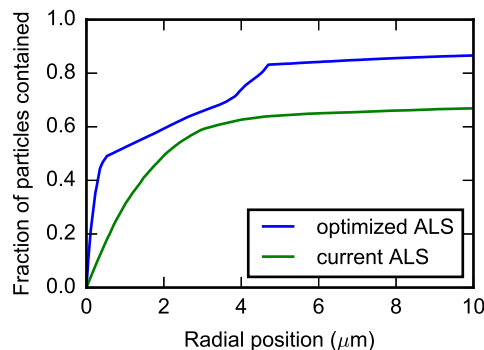


Figure 4.13: Fraction of particles within a given radius at the position of the respective smallest particle beam waist for the “Uppsala” injector (4.6 mm downstream the exit) and the new ALS design (0.5 mm downstream the exit).

subsection 4.2.1, it is, nonetheless, clear that an optimized ALS with a compact three-lens design can achieve significantly better particle beam concentration than current injectors.

4.4 Conclusion

The results of a new computer-simulation environment for ALS injectors have been presented. Previous theoretical treatments were quantitatively well reproduced. Focusing on the development of ALS for SPI experiments, the priority is to maximize the particle density along the centerline of the produced particle beam. Comparison of simulated particle profiles with experimental measurements show a good agreement, further validating our computational approach and the ability to describe the experimentally observed behavior. By computing particle trajectories through the ALS, our simulation framework can provide a detailed insight into the particle dynamics inside the ALS, such as the radial position dependent concentration mechanism of an ADL, and hence, the resulting particle profiles. This way we were not only able to monitor, e. g., the overall pressure dependence of the resulting particle beam, but to understand the mechanisms inside an ALS that are responsible for specific artifacts in the radial particle distribution. We could pin down the source of the majority of particle losses in current ALS to be caused by the double skimmer setup *before* the first lens.

Furthermore, we analyzed the formation of secondary maxima in the radial particle distribution in current ALS and found these to be caused by particles crossing the axial centerline inside the ALS. We demonstrated that it is feasible to design a simple ALS that avoids this problem altogether for particles within a narrow size range. It produces a tightly focused stream of particles exhibiting less secondary maxima and a significantly, nearly fourfold, increased particle density at the center of the distribution. In an ALS designed for a wide range of particle sizes the defocusing process and the trapping of particles in secondary maxima cannot be avoided. Therefore, a simple ALS injector system, designed only for a specific particle size, is better suited to fulfill the stringent requirements for atomic-resolution single-particle diffractive imaging and other applications that require highest particle densities. The quick exchange of lenses to adjust for distinct samples would be advantageous for high-throughput experiments. Such an ALS setup is currently under development in our laboratory, along with further quantitative measurements of particle and absolute gas densities emerging from the injector [14, 90], to benchmark and improve simulations by comparison to experiment.

Furthermore, we point out that such an optimized ALS provides a spatial separation of different species that might be present in the original aerosol, similar to more specific separation techniques for small molecules [82, 91], and thus provides a more homogeneous sample for SPI experiments [15].

5 Aerodynamic lenses at FLASH¹

An aerodynamic lens injector was developed specifically for the needs of single-particle diffractive imaging experiments at free-electron lasers. Its design allows for quick changes of injector geometries and focusing properties in order to optimize injection for specific individual samples. Here, we present results of its first use at the FLASH free-electron-laser facility. Recorded diffraction patterns of polystyrene spheres are modeled using Mie scattering, which allowed for the characterization of the particle beam under diffractive-imaging conditions and yield good agreement with particle-trajectory simulations.

5.1 Introduction

SPI at XFELs promises the recording of three dimensional structures of biological macromolecules and nanoparticles with atomic spatial resolution [11, 71]. The use of hard x-rays from XFEL sources for imaging intact molecules is enabled by ultrashort pulse durations that outrun radiation damage [4]. The three-dimensional structure can be reconstructed through careful analysis of millions of diffraction patterns from identical particles [71, 73, 83, 92]. Since every diffraction event destroys the sample [9] a continuous source of these identical particles is needed. In comparison to serial crystallography, where the diffraction signal is enhanced by the Bragg conditions of the crystalline structure of the sample, SPI of biomolecules in the range of 10–200 nm struggles a lot more with the signal to noise ratio of individual patterns. With SPI it is possible to record structures of samples that cannot be crystallized, but the brilliance of current XFELs necessitate a reduced background, the collection of even more diffraction patterns, and a smaller focus of the XFEL x-ray beam for higher intensities. And while several successful attempts of SPI have been reported [11, 13, 93], all of the mentioned additional requirements are up to now a challenge especially for sample injection.

Aerosol injectors proved to be a promising technique for delivering nanoparticles at high densities to the x-ray focus while keeping the background signal low, e. g., compared to liquid or fixed target based delivery methods [10, 12]. Commonly used injectors in SPI experiments are ALS, designed to transmit nanoparticles over a wide size range (~ 30 nm– $1\mu\text{m}$). However, as we pointed out before [94] even higher densities can be achieved by optimizing the geometry of the injector for the individual sample particles. We developed a new ALS system tailored to the needs of SPI experiments, i. e., allowing for fast changes of the geometry in order to enable optimized injection for every sample. This new ALS was demonstrated and characterized during a beam time at the Free-Electron Laser in Hamburg FLASH.

5.2 Methods

5.2.1 Experimental setup at FLASH

While the ALS presented here is used for an SPI experiment for the first time, it is completely compatible with existing injection hardware and aerosolization methods, e. g.,

¹This chapter is based on the draft: N. Roth, D. A. Horke, J. Lübke, A. K. Samanta, A. D. Estillore, L. Worbs, N. Pohlman, K. Ayyer, A. Morgan, H. Fleckenstein, M. Domaracky, B. Erk, C. Passow, J. Correa, O. Yefanov, A. Barty, S. Bajt, R. A. Kirian, H. N. Chapman, and J. Küpper. “Aerodynamic lenses at flash”, (2020). I took part in designing the new injector and preparing and conducting the experiment. I performed the trajectory simulations and the analysis of the data and wrote and discussed the manuscript.

used at XFEL endstations and in our in-house injector-characterization setup [14]. For the experimental characterization of the new injector at the CAMP endstation [95] at FLASH [96] polystyrene spheres with diameters of 220 nm and 88 nm, both with a coefficient of variance of 8 % (certificate of analysis by Alfa Aesar), were used. The sample was provided in water with a concentration of $\sim 3 \cdot 10^{11}$ particles/ml for the 220 nm and $\sim 5 \cdot 10^{11}$ particles/ml for the 88 nm spheres. For aerosolization GDVN [10] were used at flow rates of ~ 2 μ l/min. FLASH was operated at $\lambda = 4.5$ nm providing pulse trains at 10 Hz with 100 pulses per train, a 1 MHz intra-train repetition rate and an average pulse energy of ~ 15 μ J. The area of the x-ray focus was nominally 6×8 μ m², but not explicitly measured. For the reduction of background a post-sample aperture [97] was used. The pnCCD detector [80] recorded one integrated frame per pulse train. Frames with blocked x-rays were taken for dark calibration roughly every hour. The distance between the detector plane and the x-ray focus was ~ 70 mm.

5.2.2 Aerodynamic lens stack

We implemented the new ALS by attaching it to the aerosolization set-up at the end of the tube that transports the aerosol into the interaction chamber through a quick release mechanism. Figure 5.1 a shows the ALS and the quick mount. The ALS can be inserted into the mount from the side. A screw in the mounting bracket, together with two alignment rods, ensures that the round base of the ALS is centered in the correct position. Two clamps press the ALS base and its o-ring against the mount. The ALS shell consists of a tube with a round base for the quick release mount and a screwcap. The total length of the tube with the screwcap is 133.5 mm. The tube has an inner diameter of 25 mm and an outer diameter of 35 mm. Several smaller tubes with matching outer diameter and variable inner diameter can be inserted into the ALS shell. Each of these has a slot for a 0.5 mm thin pinhole aperture. The set of tubes and apertures is fixed in place by the screwcap. Different samples ask for different sets of ADLs in the ALS stack. By changing the inner diameter of the tubes, their lengths, or the aperture pinhole sizes the ALS can be individualized. This is easily implemented through the replacement of single parts. Having a set of apertures and tubes with different geometries in stock, together with the quick release mount, allows for fast adaption of the ALS without the need of manufacturing or time consuming disassembling of the sample injection set-up. Furthermore, this concept also allows replacing of the tubes and apertures with more complex geometries. Some parts are made of different materials in order to prevent cold welding: The screwcap is made of copper while the tube, the clamps and the pinhole apertures are made of stainless steel. The mounting plate, the mounting bracket, and the distance tubes are made of aluminum. The o-ring is made of viton.

Figure 5.1. During the beam time at FLASH the same experimental apparatus was used for other, biological, samples as well. The ALS geometry was not optimized explicitly for the samples used here and the geometry and the injection conditions were kept constant for both polystyrene sizes. The exact geometry is shown in Figure 5.1 b. The ALS was mounted onto a motorized XYZ manipulator such that the particle beam could be moved across the x-ray focus. Due to mechanical restrictions in the endstation setup the ALS was kept at rather long distances from the x-ray focus of 16.5 mm.

5.2.3 Trajectory simulation

The ALS performance and resulting particle beam profile were simulated using our previously reported approach [94]. The flow field of the helium carrier gas through the

differential pumping between GDVN and ALS as well as the flow field through the ALS were calculated using the finite-elements method solving the Navier-Stokes equations [62]. Trajectories of individual polystyrene spheres were calculated using Stokes' drag force. While the overall procedure and assumptions were the same as reported previously [94], the boundary conditions and the geometry, see Figure 5.1, were adapted to the current experimental conditions. The most significant adjusted simulation parameters are the mass flow of the helium entering the aerosol injector from the GDVN and the measured pressure in the tube directly before the ALS. The former is used as the boundary condition for simulating the differential pumping stage and was set to 100 mg/min. The pressure before the ALS was measured to be 1.4 mbar.

5.2.4 Pattern classification

Following dark calibration and correction of bad detector pixels, only frames containing at least 500 of the 542394 remaining pixels above the one-photon level were retained for analysis. The known spherical structure of the polystyrene was used to differentiate

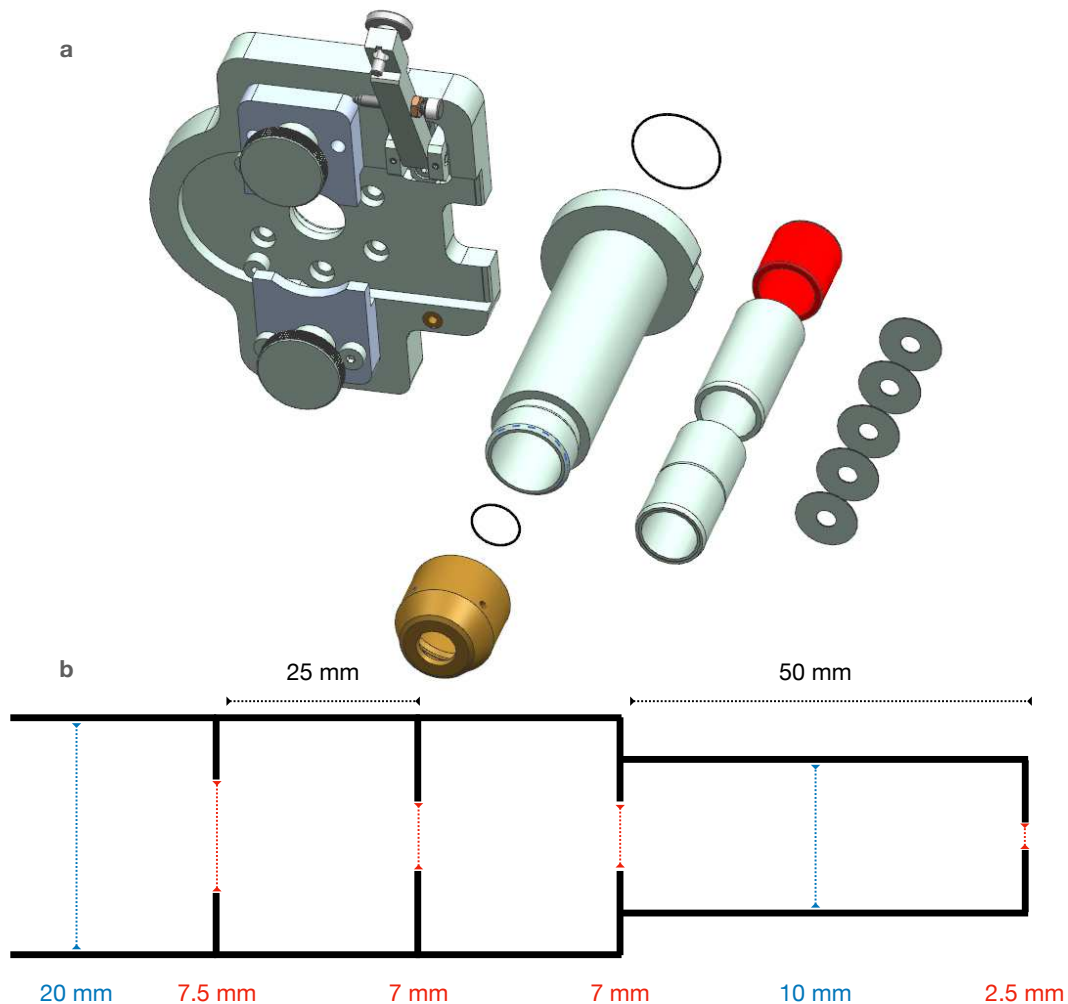


Figure 5.1: a) The quick release mount, that attaches the ALS to the aerosol transport tube. The new ALS and its parts. b) The geometry of the ALS set-up used at the experiment at FLASH.

between camera frames that recorded a diffraction pattern of single sample particles and patterns from clusters of sample or any other impurity that might have been recorded. The diffraction pattern of a polystyrene sphere was modeled by the calculated Mie scattering of a homogeneous sphere using the miepython library [98]. The complex refractive index for this calculation, the position of the x-ray focus relative to the detector, and the mean particle diameter were obtained by fitting the model to the sum of all 20964 hits collected while injecting 220 nm polystyrene spheres. The fitness function was $F = 1 - P(f, g)$ with the Pearson correlation P of the one dimensional representations of the summed experimental (f) and the modeled (g) pattern. The complex refractive index obtained was assumed to be the same for all PS particles. With this refractive index and the x-ray focus position every single diffraction pattern was modeled individually using the same model; the radii of the particles were again fitted using the same fitness function as above. 6745 diffraction patterns for 220 nm particles and 1893 for 88 nm particles with a similarity of $P(f, g) > 0.3$ were kept for further analysis. Histogramming the diffraction patterns per transverse injector position yielded a two-dimensional projection of the particle beam profile at a distance of 16.5 mm from the injector tip.

5.3 Results & Discussion

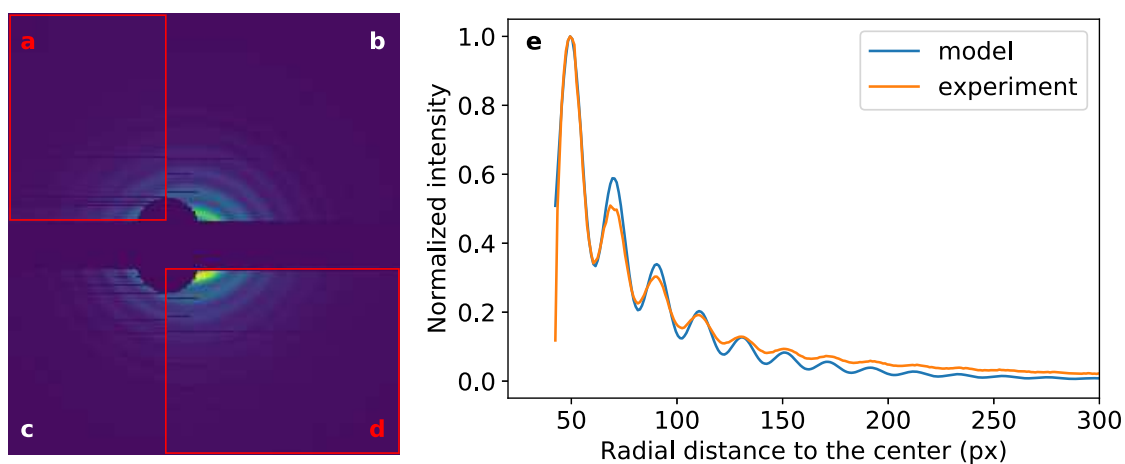


Figure 5.2: Sum of 20964 diffraction patterns collected during 220 nm polystyrene injection; experimental data is provided in the red boxes (a, d) and compared to the fitted model. The left figure shows a section of the left half (a) and the right half (d) of the upper detector. The corresponding modeled sections (b, c) are flipped at the horizontal axis to allow for a detailed comparison. (e) Radial plot comparing the angularly integrated experimental and simulated data.

Figure 5.2 shows the sum of the 20964 experimental patterns for 220 nm polystyrene in comparison to the fitted model in a 2D image and a radial plot. Figure 5.2 a shows a section of the left half of the upper detector with the measured data. The corresponding modeled section of the left half of the upper detector is shown in Figure 5.2 c mirrored around the x axis. Figure 5.2 b, d shows a section of the the right half of the upper detector. This time the measured data is mirrored around the x axis and shown in Figure 5.2 d. Accordingly, Figure 5.2 b is the modelled right detector half. As previously described this fitted model is used to obtain static parameters such as the distance to the x-ray focus and the refractive index of the polystyrene spheres. Good agreement regarding both the intensities and the

fringe spacing can be observed. The fitted mean diameter of the polystyrene spheres of 222.5 nm is in excellent agreement with the manufacturer specifications. From this fit, we obtained a refractive index for polystyrene at a wavelength of 4.5 nm of $m = 0.976 - 0.001i$. We point out that our derivation is not very sensitive to the real part of the refractive index. To our knowledge, no comparable values are available; using theoretical predictions for atomic carbon [99] for 4.5 nm and 1050 kg/m^3 , the density of polystyrene the refractive index would be approximately $m_C \approx 0.999 - 0.0001i$, which is in fair agreement with our experimental value.

Fitting the 6745 and 1893 individual diffraction patterns of 220 nm and 88 nm particles result in mean particle sizes of $223 \pm 7 \text{ nm}$ and $93 \pm 5 \text{ nm}$, respectively. Comparing this with the specifications given by the manufacturer ($220 \pm 18 \text{ nm}$ and $88 \pm 7 \text{ nm}$) further increases the confidence in our analysis. For the larger polystyrene sphere the obtained mean diameter is within 2 % and for the smaller within 6 % variation from the specified size, well within the manufacturer's 8 % confidence range.

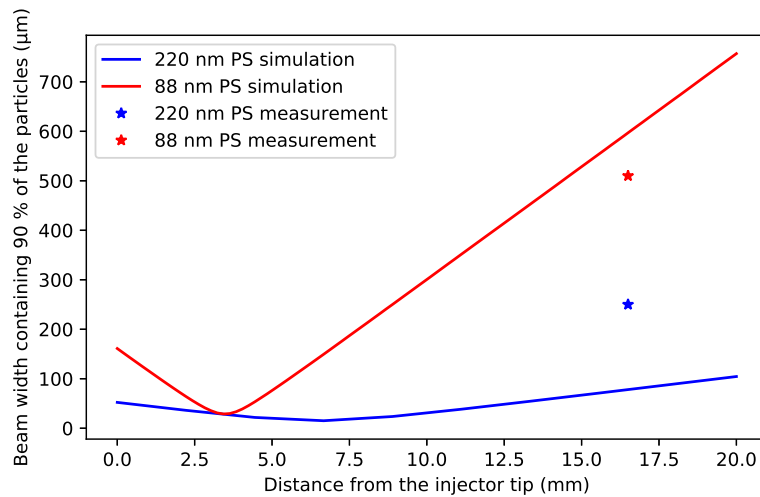


Figure 5.3: Simulated beam width containing 90 % of the particles for different distances to the injector tip for 220 nm and 88 nm polystyrene spheres. The measured beam widths are marked as single points with a star, see text and Figure 5.4 for details.

Figure 5.3 shows the simulated beam width containing 90 % of the particles at different distances to the injector tip. The particle beam for 220 nm is overall narrower and has its focus at $\sim 7 \text{ mm}$ downstream the injector tip. The focus of the 88 nm beam is roughly a factor two closer to the tip at $\sim 3 \text{ mm}$ and the beam has a much higher convergence before and divergence after its focus. For comparison, the experimentally observed beam widths for both sizes are depicted by stars in Figure 5.3. The measurement reflects the tendency of the 88 nm beam to be broader at this position, but the simulations are clearly underestimating the observed 220 nm beam width. Measured and simulated beam profiles of the two particle sizes at this position, $z = 16.5 \text{ mm}$, are shown in Figure 5.4. The beam profiles for the 220 nm polystyrene spheres (blue) show a clear peak and a fast fall off, graphically comparable to a Lorentz function, but with the experimental beam being broader than the simulated profile. The beam profiles for the 88 nm polystyrene spheres (red) on the other hand also show a peak in the center, but a much slower fall off and even still significant population at the edges of the measurement window. This behavior is present for both, the measured and the simulated profile.

As previously mentioned, for this experimental campaign the ALS was not optimized for a specific size but to transmit particles in a broad size range from 40 to 300 nm well. Also the geometry and injection conditions were kept constant. Hence, it is expected that the focusing behavior of the ALS for 220 nm and 88 nm differs substantially. Especially for particles below 100 nm optimization of the injector conditions is usually quite challenging [94, 100] and without specific optimization a broader beam profile compared to beams of larger particles is expected. The 88 nm particles are not only smaller but also lighter, hence at the same flow conditions they get accelerated to higher radial velocities and indeed this is what we observe in Figure 5.3. The slow fall off in the beam profile is actually a behavior that was previously observed and explained by too high radial acceleration of the particles at individual ADLs within the injector [94]. This also explains why we do not see this effect for 220 nm particles, since their higher mass and inertia leads to less extreme focusing mitigating these effects.

While underestimating the beam width for 220 nm particles, these simulations clearly reflect the major aspects of the measured data. With only one measurement point it is challenging to provide a detailed explanation for the deviation between simulation and experiment in the case of 220 nm polystyrene, possible reason is that the 220 nm particle beam is almost collimated. Hence, the position of the focus is a lot more sensitive to experimental imprecisions not reflected in the simulations. For instance, a systematic error on the measured pressure before the ALS could significantly change how hard the 220 nm beam is focused, while the 88 nm beam is already at its extreme.

In any case, the results provided here demonstrate that the described new flexible ALS injector setup with novel capabilities for fast exchange and geometry adjustments works very well for the injection of nanoparticles in SPI experiments.

5.4 Conclusion

SPI experiments have the potential to unravel the three-dimensional structure of complex biomolecules such as proteins, but they have very specific requirements for the sample

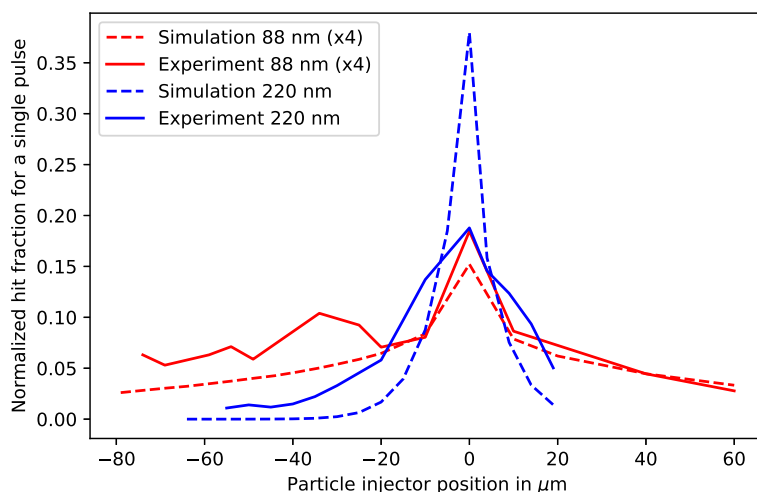


Figure 5.4: Measured and simulated hit fraction for a single x-ray pulse dependent on the transverse injector position relative to the x-ray focus. The data for 88 nm polystyrene was scaled by a factor of 4 for better visibility.

injection. In order to be able to provide the necessary densities for efficient SPI experiments an injector needs to be optimized for every individual sample. Here, we established a new aerodynamic lens injector tailor made for these experiments that allows for quick exchange of the geometry and allows optimization of the injection system beyond the adoption of carrier gas pressures. Besides the successful first operation under SPI conditions at an XFEL, the resulting particle beams could be well predicted using our simulation framework citeRoth:JAS124:17, Welker:CMInject:inprep. The simulations showed that the focus of the particle beams for both samples was closer to the injector tip than the mechanical limitations of the setup allowed. This shows how crucial it is not only to characterize the injection system in advance utilizing simulations, but also to be able to adopt the geometry of the injector for optimized experimental conditions for each sample, especially when moving to smaller samples where the amount of scattering signal and the general transmission of the sample decreases. The new flexibel ALS system introduced here will simplify and fasten this optimization process. The analysis of the diffraction patterns of 220 nm polystyrene spheres also yielded the *a priori* unknown complex refractive index of this material $m = 0.976 - 0.001i$ at $\lambda = 4.5$ nm.

6 Controlled beams of shockfrozen, isolated, biological and artificial nanoparticles¹

XFELs promise the diffractive imaging of single molecules and nanoparticles with atomic spatial resolution. This relies on the averaging of millions of diffraction patterns of identical particles, which should ideally be isolated in the gas phase and preserved in their native structure. Here, we demonstrated that polystyrene spheres (PS) and *Cydia pomonella* granulovirus can be transferred into the gas phase, isolated, and very quickly shockfrozen, i. e., cooled to 4 K within microseconds in a helium-buffer-gas cell, much faster than state-of-the-art approaches. Nanoparticle beams emerging from the cell were characterized using particle-localization microscopy with light-sheet illumination, which allowed for the full reconstruction of the particle beams, focused to $< 100 \mu\text{m}$, as well as for the determination of particle flux and number density. The experimental results were quantitatively reproduced and rationalized through particle-trajectory simulations. We propose an optimized setup with cooling rates for few-nanometers particles on nanoseconds timescales. The produced beams of shockfrozen isolated nanoparticles provide a breakthrough in sample delivery, e. g., for diffractive imaging and microscopy or low-temperature nanoscience.

6.1 Introduction

Nanometer objects are of extraordinary importance in nature, for example in the complex biological machinery of viruses [101]. Furthermore, the 21st century has been hailed as the “age of nanotechnology”, with the advent of, e. g., novel nanomaterials, such as quantum-dot light emitting diodes [102] and nanomedicine [103]. Understanding the fundamental functionality of these systems requires high-resolution structural information. Recent years have seen phenomenal progress in this area. One pioneering approach to measure direct structural information from isolated nanoparticles is SPI, enabled by the advent of XFELs [4, 11, 15]. This promises the recording of atomically-resolved structures from isolated nanoobjects without the need for large, highly-ordered crystalline samples [4, 11]. It relies on recording a series of two-dimensional diffraction images from randomly oriented isolated particles, which can then be assembled *in silico* to a 3D diffraction volume and the structure reconstructed. Since the first demonstration of this approach a decade ago [9], several significant steps in experimental procedures [71, 73] and data analysis [76] have pushed the achievable resolution to below 10 nm [104].

A further technique for direct structural imaging of nanometer-sized objects is cryo-electron microscopy (CEM), where several recent breakthroughs have enabled single-particle structure determination to sub-nanometer resolution [105, 106]. Unlike SPI, CEM images a single nanoparticle, immobilized and shock-frozen onto a support. This sample preparation using the plunge-freezing approach is a crucial step of CEM success [107]. However, various issues with the technique have been discussed [107].

In contrast to CEM, the SPI approach images isolated particles *in vacuo*, i. e., without any mechanical sample support. However, due to its diffraction-before-destruction approach [4], it requires the imaging of millions or billions of identical particles to allow

¹This chapter is based on the publication: A. K. Samanta, M. Amin, A. D. Estillore, N. Roth, L. Worbs, D. A. Horke, and J. Küpper, “Controlled beams of shockfrozen, isolated, biological and artificial nanoparticles,” *Struct. Dyn.* 7, 024304 (2020). I performed early simulations for designing the buffer-gas cell, contributed setting up the simulations reported in the publication, assisted improving them and discussed the results.

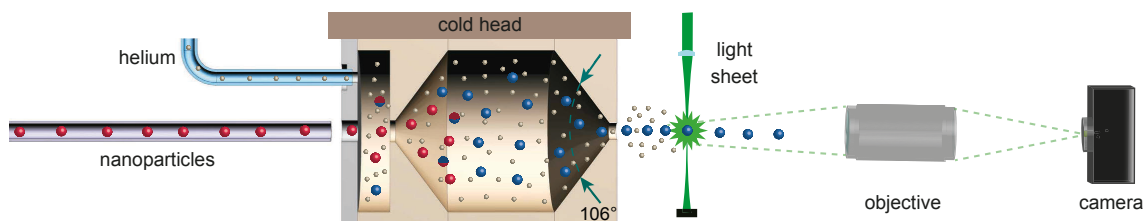


Figure 6.1: **Schematic of the experimental setup.** Aerosolized nanoparticles (red spheres) are transported into the cryogenically cooled buffer-gas cell, where they collisionally thermalize (blue spheres) with pre-cooled helium (brown spheres). They exit the cell forming a beam of cold nanoparticles, which is characterized using a single-particle localization microscope. The buffer-gas cell has detachable conical entrance and exit endcaps with a full opening angle of 106° [108].

the reconstruction of the 3D structure. One of the major challenges for improving the achievable resolution is the reproducibility of the target, i. e., the stream of isolated single particles probed by the XFEL. To date, these experiments have been conducted with room temperature aerosols, in an attempt to keep the biological systems studied under native-like conditions. This approach also leads to a dynamical exploration of the conformational landscape. It demands the collection of a very large dataset for SPI experiments, which then have to be analyzed for structures in terms of conformations and spatial orientations. Eventually, this will also limit the achievable resolution for a given measurement time. Moreover, these experiments are often struggling with limited hit rates and limited availability of time for experiments at XFEL facilities, which represent a major obstacle for the collection of a sufficiently large dataset required for a high-resolution reconstruction.

Here, we propose and demonstrate a novel sample preparation using rapidly shock-frozen beams of, potentially hydrated, isolated nanoparticles. Using a cryogenic buffer-gas cell, nanoparticles were rapidly cooled on a microsecond timescale, sufficiently fast to prevent denaturation, and then extracted into a collimated particle stream in vacuum. The produced high-density beams make an ideal target for SPI experiments and, furthermore, are highly amenable to further control, e. g., by external electric or acoustic fields. The cryogenic-temperature samples will allow one to spatially separate conformers [82, 91, 109–111], to strongly align and orient the particles in the laboratory frame [112, 113], or to produce very high densities through the focusing of the particles with external fields [114, 115].

Our development provides touch-free shock-frozen sub-10 K focused particle beams of artificial and biological nanoparticles. Particles were aerosolized from solution at room temperature using a gas-dynamic virtual nozzle [10, 86] and transported into a cryogenically-cooled helium-filled buffer-gas cell, in which isolated nanoparticles were quickly cooled through collisions with the cold helium gas. Buffer-gas cooling is an established technique in atomic and molecular physics [116], but had so far not been applied to systems with more than a few tens of atoms [117, 118]. We demonstrate its applicability to shock-freeze PS of 220 nm and 490 nm diameter as well as the native occlusion bodies of *Cydia pomonella* granulovirus (CpGV) particles with a size of approximately $265 \times 265 \times 445 \text{ nm}^3$ [119]. The shock-frozen particles were extracted from the buffer-gas cell and formed a collimated or focused nanoparticle beam. Here, individual particles were detected using single-particle-localization microscopy [14]. Measured particle distributions for different helium-flow conditions were well reproduced by particle-trajectory simulations, which furthermore allowed us to extract cooling rates and times.

6.2 Methods

6.2.1 Experimental details

A schematic of our experimental setup is shown in Figure 6.1. It consisted of four main parts: an aerosolization chamber, a differentially pumped transport tube, the cryogenically-cooled buffer-gas cell, and a detection region. Isolated nanoparticles were created by aerosolizing aqueous solutions using a gas-dynamic virtual nozzle [10, 86]. We have used PS of 220 nm (Alfa Aesar, 220 ± 17.3 nm) and 490 nm (Molecular Probes, 490 ± 15 nm) with a concentration of 5×10^{10} particles/ml. CpGV samples were produced following a known protocol [119]. Leaving the aerosolization chamber, the particles passed through a set of two skimmers ($\varnothing_1 = 0.3$ mm, $\varnothing_2 = 0.5$ mm) placed 2 mm apart. The region between the skimmers was evacuated to remove background gases from the aerosolization processes, e. g., helium and water, to avoid ice formation and clogging of the buffer-gas cell (BGC) inlet and outlet. The particle stream then entered a transport tube, with a typical pressure of 10 mbar during operation. The warm isolated nanoparticles were introduced into the buffer-gas cell using a 10 cm long stainless steel capillary with an inside diameter of 800 μ m. The complete aerosol generation and transport assembly is attached to the vacuum chamber using a three-dimensional position manipulator, allowing precise alignment of the capillary to the 2 mm buffer-gas cell inlet. During the experiment the capillary tip was located 7 mm outside the cell entrance aperture. The buffer-gas cell was located in the main vacuum chamber, maintained at a pressure below 10^{-6} mbar by a turbomolecular pump (Pfeiffer Vacuum HiPace 2300). It was attached to a 2-stage pulse-tube refrigerator (Sumitomo RP082E2) with typical operating temperatures of 29 K and 3.6 K, shielded from thermal radiation by aluminium and copper heat shields attached to the cooling stages. Coconut charcoal attached to the second stage radiation shield provides additional pumping capacity. The buffer-gas cell itself was a hollow copper cylinder ($\varnothing = 3$ cm, 2 cm length) with detachable copper endcaps for both entrance and exit side. We used conical endcaps with an opening angle of 106° [108]. Inside the buffer-gas cell, the room-temperature nanoparticles underwent rapid collisional thermalization with the 4 K cold helium gas at typical densities of $\sim 10^{16}$ cm $^{-3}$. The cooled nanoparticles were extracted through an exit aperture of 2 mm diameter into high vacuum, $p < 10^{-6}$ mbar, forming a collimated/focused particle beam [94], while the density of the helium gas dropped quickly [90]. Particles were detected 10 mm after the exit of the cell by particle-localization microscopy based on optical light scattering [14]. The use of a light sheet to illuminate particles allowed a large-area illumination and hence direct measurement of the entire transverse profile of the particle beam [32]. The generated particle size distribution was monitored using a commercial differential mobility analyzer (TSI 3786) and condensation particle counter (TSI 3081).

6.2.2 Simulation details

The experiments were complemented by quantitative simulations of nanoparticles traveling through the apparatus. To model the gas-particle interactions within the buffer-gas cell, we developed a numerical simulation framework capable of calculating the buffer-gas flow field, trajectories of particles in the flow field, and the resulting particle temperatures. The velocities and pressures of the helium flow-field were obtained by solving the Navier-Stokes equation at 4 K using a finite element solver [120] for different mass flow conditions. Then, using a homebuilt simulation framework, particle trajectories were calculated within the evaluated steady-state flow field according to Stoke's law. A temperature dependent particle-slip-correction factor is required to calculate the drag forces [46]. As no such

correction factor was reported for cryogenic temperatures, we used the known values for air in the range 200–1000 K [46] scaled up by a factor of 4 to give consistent results with our experiment at cryogenic temperature. Due to the low nanoparticle densities, we assumed no effect of the particles on the flow-field and no particle-particle interactions. Numerical integration is performed using the Dormand & Prince Runge-Kutta method `dopri5` as provided in `scipy.integrate.ode`. The flowfield data are linearly interpolated using `scipy.interpolate.RegularGridInterpolator` [121]. The particles' phase-space distribution at the inlet of the buffer-gas cell was assumed to be Gaussian, with mean values and standard deviations obtained from simulating particle trajectories in the transport tube and capillary using an cylindrically symmetric model for that part of the setup. Simulations through the buffer-gas cell were performed using both, a 2D description assuming cylindrical symmetry and the 3D exact experimental geometry. The latter was deemed necessary because of small deviations of the apparatus from cylindrical symmetry due to the precooled-helium inlet, see Figure 6.1. At high helium flows this led to a noticeable asymmetry in the produced particle distribution, which was well-reproduced by the 3D simulations, *vide infra*. Initial phase-space distributions of particles at the entrance of the buffer-gas cell were taken from equivalent simulations of the transport system [94]. The final phase space distribution of the particle beam was collected at a detector placed 10 mm behind the buffer-gas cell outlet.

Nanoparticle temperatures were evaluated by two independent approaches. A collision-based model was used to calculate the temperature drop per helium-particle collision, ensuring conservation of energy and momentum [116]. This yields the particles translational temperature, but does not take into account the thermal properties or the internal heat capacity of particles. In the second approach the heat transfer from the nanoparticle into the buffer gas was estimated by calculating the Nusselt number for forced convection of flow past a single sphere [122]. The cooling rate taking into account the heat capacity of the particles was then estimated according to Newton's law of cooling:

$$T(t) = T_{\text{He}} + (T(0) - T_{\text{He}})e^{-hA/C} \quad (6.1)$$

with the temperature $T(t)$ of the particle at time t , $T_{\text{helium}} = 4$ K, the initial temperature of polystyrene $T(0) = 298$ K, the surface area A of the nanoparticle, the total heat capacity C , which is the specific heat capacity C_p multiplied by the particle mass, and the heat transfer coefficient h . The latter was obtained by calculating the Nusselt number Nu for a flow past a sphere using the Whitaker formula [122]:

$$\bar{Nu} = 2 + \left(0.4 Re^{1/2} + 0.06 Re^{2/3}\right) Pr^{0.4} \left(\frac{\mu_b}{\mu_0}\right)^{1/4} \quad (6.2)$$

with the Reynolds number Re , the Prandtl number Pr , the fluid viscosity μ_b evaluated at the bulk temperature $T_{\text{He}} = 4$ K, and the fluid viscosity μ_0 evaluated at the initial surface temperature $T(0) = 298$ K. As the mean free path of the helium gas is larger than the nanoparticle diameter, a rarefied-gas correction was used [123]:

$$\bar{Nu} = \frac{Nu_0}{1 + 3.42 \frac{M}{Re Pr} Nu_0} \quad (6.3)$$

with the Nusselt number in the continuum regime Nu_0 and the Mach number M . The heat transfer coefficient h was calculated as $h = k \bar{Nu} / D$ with the diameter of the nanoparticle D and the thermal conductivity of helium k .

6.3 Results and discussion

Spatial profiles of shock-frozen particles in the detection region are shown in Figure 6.2 for 220 nm and 490 nm PS for different helium flow rates. The strong variations of the particle beams for different flow conditions clearly indicate a strong interaction, i. e., many collisions, with the helium gas. For the experimental detector position 10 mm behind the cell outlet, the most collimated particle beam was observed at helium flow-rates of 30 and 50 ml_n/min for 220 nm and 490 nm PS, respectively. From Figure 6.2 it is evident that the particle distributions were not spherically symmetric, but elliptical. We attribute this to an asymmetric helium flow-field, caused by the location of our helium inlet at the top of the buffer-gas cell inlet. Despite careful cell design, including a first gas inlet chamber for providing a quasi-axisymmetric flow into the main cell [108], at large flow rates significant asymmetries existed in the gas flow, see Figure 6.3. We quantified

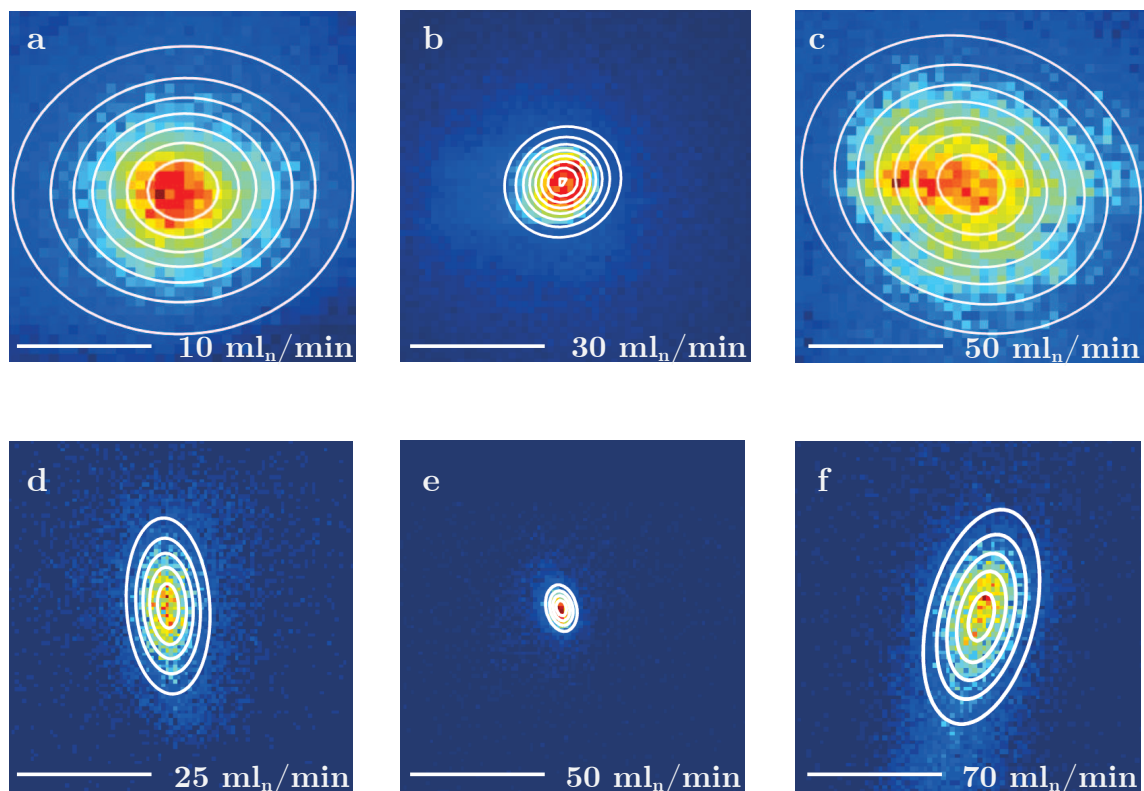


Figure 6.2: **Experimental particle beam profiles of PS.** Profiles of the particle beam emerging from the buffer-gas cell for different helium flow rates at the position of the light sheet (a–c) for 220 nm and (d–f) for 490 nm PS. The scalebars in the left bottom of the figure represent 500 μm , the individual helium gas flows are specified at the bottom right of every panel, and the color coding represent increasing particle flux from blue to red. Contour lines (white) represent 2D Gaussian fits; see text for details.

the size of the particle beams using a 2D Gaussian, indicated by the contour lines in Figure 6.2. The measured dependence of the particle beam size on the helium flow is shown in Figure 6.7 (black curves). Here, we used the mean of the full width at half maximum (FWHM) of the minor and major axes of the 2D Gaussian to quantify the produced beam size. Individual plots for the major and minor axis for both particle sizes are shown in Figure 6.4. For both PS sizes an increase in helium flow led to a gradual

decrease in particle beam size until it reaches a minimum, i. e., a spatial focus, at the detector. Further increasing the helium flow focused the particle beam further, moving the focus before the detector, which resulted in an again larger beam size at the detector, as evident from simulated particle beam diameters at different distances from the buffer-gas-cell outlet and for different flow conditions, see Figure 6.5–Figure 6.6. We simulated the measured focusing curves using both, 2D-axisymmetric and 3D asymmetric, flow-condition models, *vide supra*. Comparisons between measured and simulated beam widths for 220 nm and 490 nm PS are shown in Figure 6.7. All simulations are in very good agreement with the experimental data. This also validated our simulation framework, which thus provides further insight into the fluid-dynamic focusing process. For instance, for 490 nm and 220 nm PS particles and a helium flow of 50 ml_n/min the simulations yielded particle speeds in the laser-detection region of 16 m/s and 22 m/s, respectively. The simulations also provided the phase-space distributions of the particle beams at different coordinates within the buffer-gas cell, which for three different flow rates are visualized in Figure 6.8 and Figure 6.6. These distributions clearly illustrate the focusing effect, but also the asymmetry present in the helium flow-field for large flows. While the obtuse angles of the buffer-gas cell significantly reduce the formation of turbulences [108] the asymmetry of the flow-field, with some indications of remaining turbulences, led to a significant variation of the particles transverse velocities, especially at large helium flows. It is also evident from the simulated particle beam diameters at different distances from the buffer-gas-cell outlet, Figure 6.5, that at a very low helium flow of 25 ml_n/min

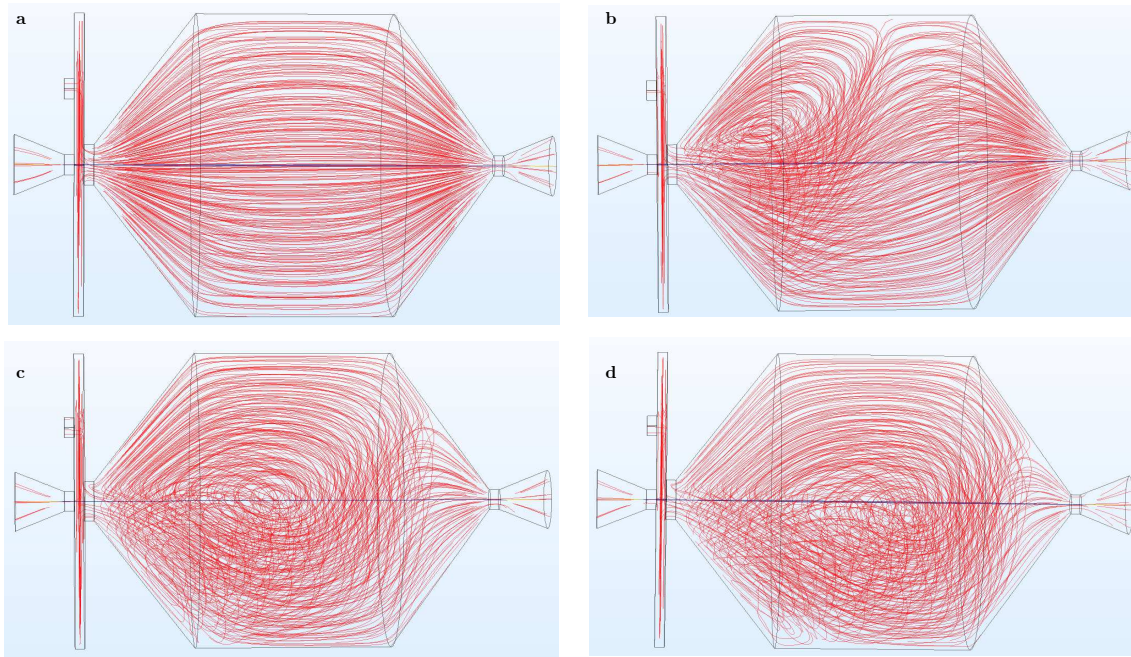


Figure 6.3: **Helium flowfields for different flow conditions in the BGC**, calculated using a finite-element method for laminar flows (COMSOL Multiphysics). **(a–d)** Calculated fields for helium flows of 10 ml_n/min, 30 ml_n/min, 50 ml_n/min and 70 ml_n/min, respectively, are depicted through streamlines with the helium flowing from left to right. The location of the helium inlet is at the top of the thin inlet-disk on the left of the main cell. It is evident that an increased helium flow resulted in turbulence and thus introduced asymmetries in the helium flowfields.

not much focusing occurred and the particle beam was collimated, in contrast to the typical convergence-divergence behavior at higher helium flows, which resembles typical aerodynamic lens systems [23, 94]. At sufficiently high flow rates, the thermalized particles in the buffer-gas cell followed the flow-field and, when traveling through the small orifice, sped up. The large momentum of the particles led to a more ballistic behavior when

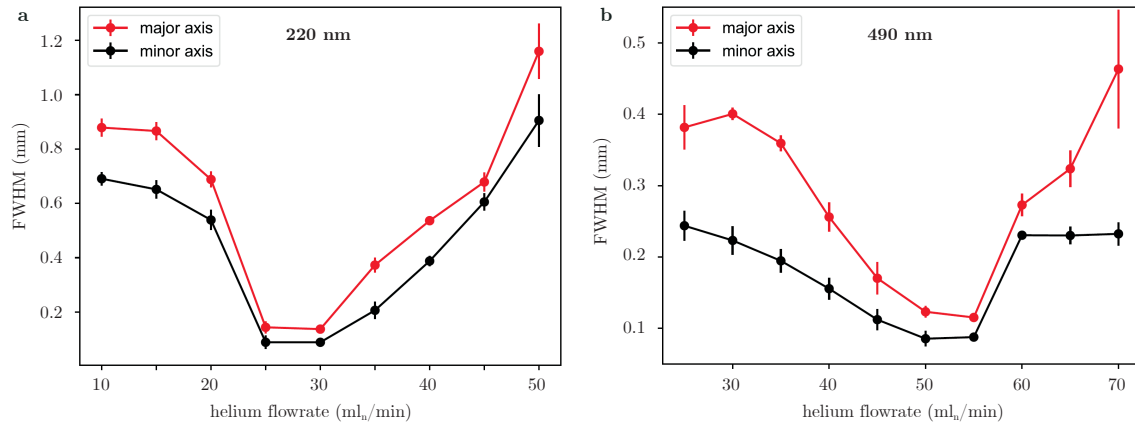


Figure 6.4: Measured dependence of the particle beam size on the helium flow rates for PS. FWHM of the particle beams at the detector position, 10 mm behind the BGC outlet, along the major (red) and minor (black) axis for (a) 220 nm and (b) 490 nm PS spheres, as determined using 2D-Gaussian fits.

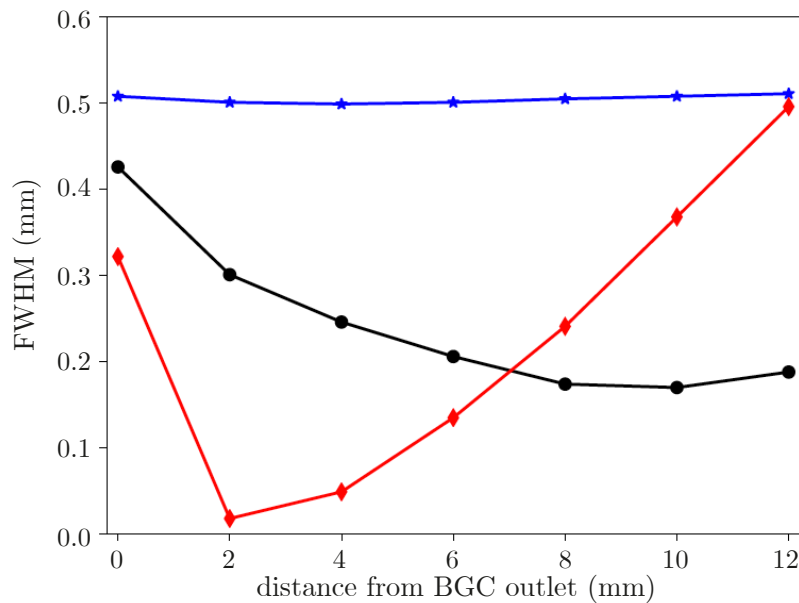


Figure 6.5: Simulated focusing behavior at different helium flow rates of 25 ml_n/min (blue), 50 ml_n/min (black), and 65 ml_n/min (red) for 490 nm PS particle beams. The mean values of the major and minor axes FWHMs are plotted as a function of the distance behind the buffer-gas cell outlet. At low helium flow, 25 ml_n/min, the particle beam is collimated, in contrast to the focused particle beams at higher flow rates of 50 and 65 ml_n/min. This also demonstrates that the location of the focal distance can be tuned through changes in the flow rate, i. e., the helium inlet pressure.

leaving the buffer-gas cell and thus a significantly lower divergence of the particle beam

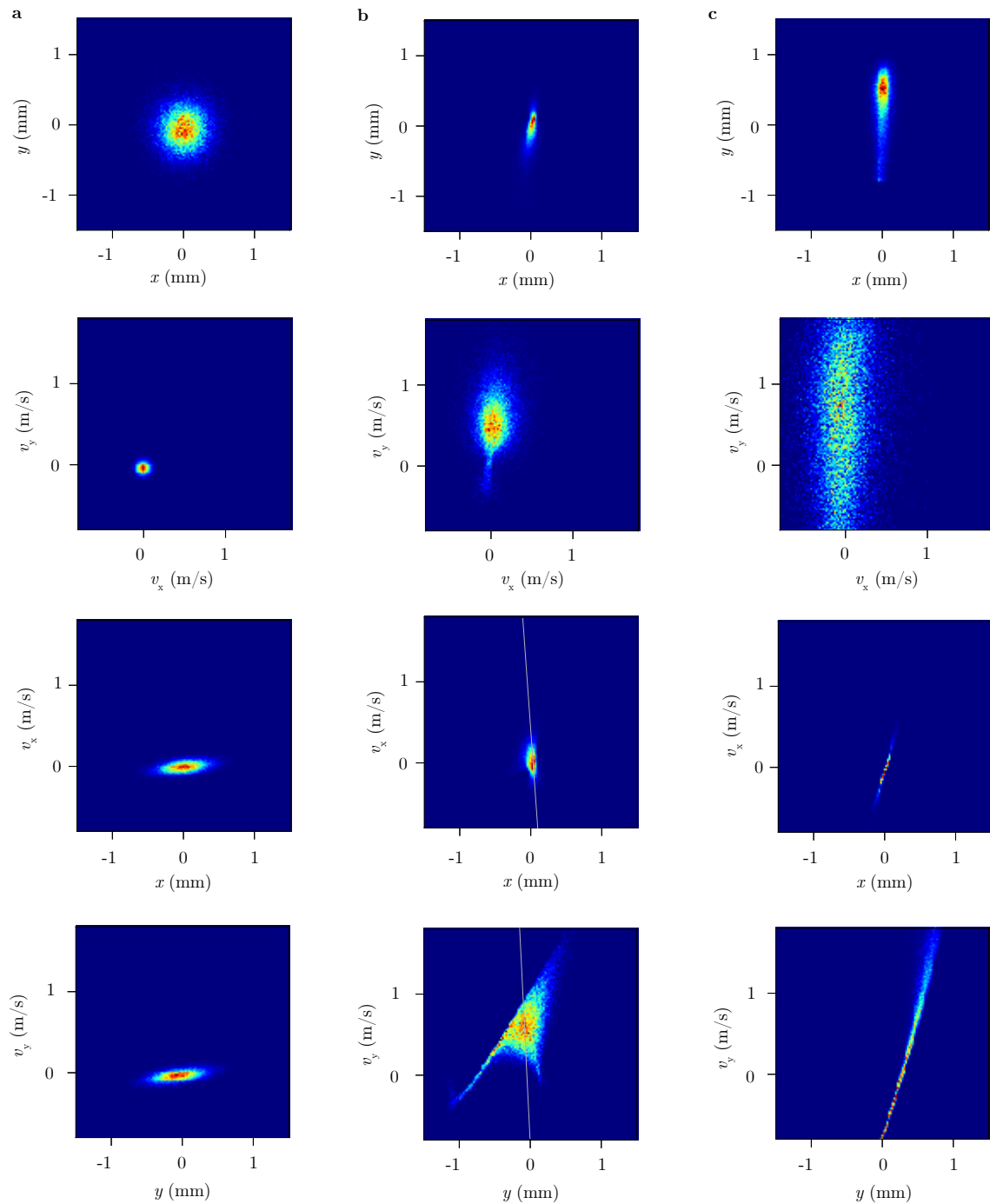


Figure 6.6: Phase space distributions of a beam of 490 nm PS particles 5 mm after the buffer-gas cell outlet, similar to the distribution shown in Figure 6.8. Columns (a–c) represents different flow conditions of 25 ml_n/min, 50 ml_n/min and 65 ml_n/min, respectively. The (x, v_x) and (y, v_y) slices for 50 ml_n/min demonstrate that this beam is still converging, as highlighted by the major principal component of the distribution (grey line). However, for the 65 ml_n/min flow rate they show a diverging particle beam, i. e., in this case the $z = 5$ mm position is already behind the focus, consistent with Figure 6.5.

than of the gas flow. The exact focusing properties of the nanoparticle beam depended on the particles momentum and thus its fluid-dynamic properties and mass, as well as the flow-field [23, 124]. Generally, heavier particles require larger gas flows for focusing. The particle transmission also increased with increasing helium flow inside the cell, see Figure 6.9. For 220 nm particles, the maximum transmission is achieved for a helium flow of 30–35 ml_n/min at 4 K, with a tenfold increase in transmission compared to the lowest flow rate of 5 ml_n/min . This is attributed to stronger fluid-dynamic forces due to the pressure increase, which efficiently guided the nanoparticles through the buffer gas cell and minimized losses due to collisions with the walls [116]. Flow conditions for maximum transmission also coincide well with maximum focusing, yielding a seventy times higher flux at the detector for 30 ml_n/min than for 5 ml_n/min , see Figure 6.9. With advanced fluid-dynamic focusing outlets [94], beam focusing and particle flux can be improved even further. Moreover, the effect of Brownian motion will be significantly reduced by the 4 K translational temperature compared to previous room-temperature approaches. This is especially important for small particles and thus will strongly improve their focusing and thus the densities in single-particle imaging experiments. Our precise flow-field and particle-trajectory simulations allowed us to assess the temperature and cooling rate of particles traveling through the cold buffer-gas cell. The number of collisions with helium required for full thermalization depended on the thermal properties of the particle as well as its size and velocity relative to the gas. In Table 6.1, we provide simulated cooling times to several temperatures and corresponding initial cooling rates, for PS of 10–500 nm diameter as well as for the prototypical protein lysozyme [4, 125]. These were calculated assuming forced convection and Newton’s law of cooling and took into account the particles initial internal energy at room temperature. Full cooling curves, i. e., the

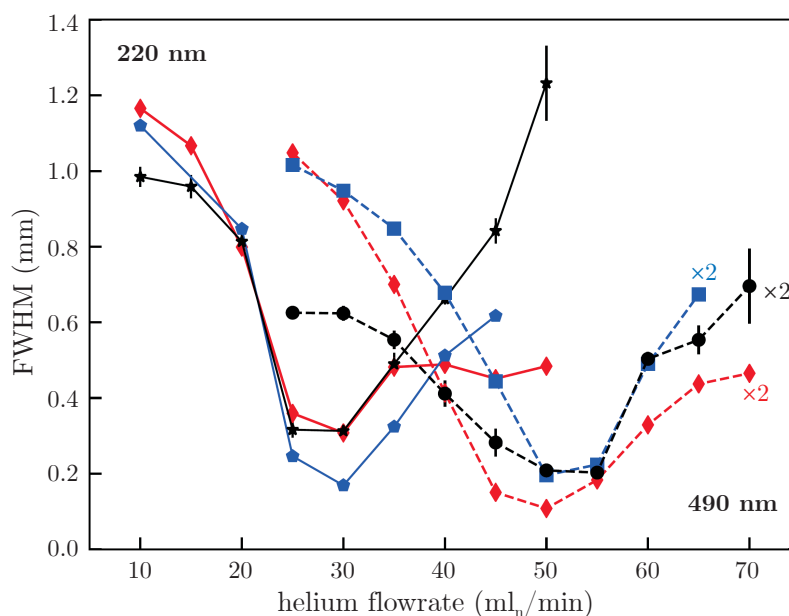


Figure 6.7: **Focusing behavior of PS.** Measured particle beam widths for 490 nm (dashed lines) and 220 nm (solid lines) PS as a function of helium flow rate. Black lines represent the experimental data, while red lines are from two-dimensional-axisymmetric and blue lines from three-dimensional simulations, as discussed in the text. For the 490 nm datasets the width are scaled by a factor two to improve visibility of the variation.

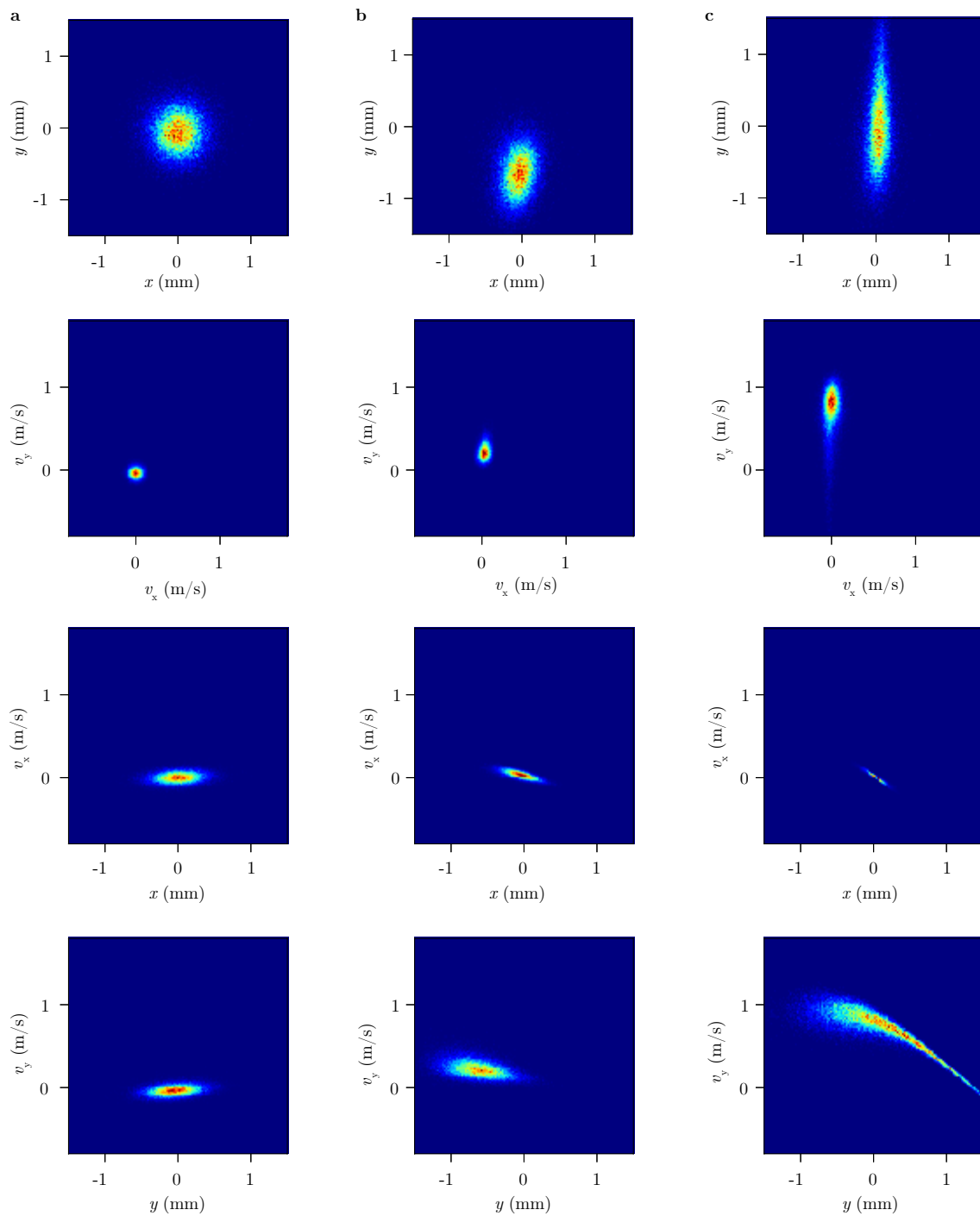


Figure 6.8: **Phase space distributions of a beam of 490 nm PS particles 5 mm before the buffer-gas cell outlet.** Each column (a–c) represents different helium flow conditions of 25 ml_n/min, 50 ml_n/min and 65 ml_n/min, respectively. y is along the vertical direction in Figure 6.3, i. e., in the direction from the center to the helium flow inlet at the top of the buffer-gas cell. Generally, the spread along v_y is significantly higher than along v_x , which is due to asymmetries introduced by the position of the helium inlet, especially at higher helium flow. For the larger flow rates, the (x, v_x) and (y, v_y) slices show a converging particle beam due to the focusing induced by the hydrodynamic forces.

	200 K	133 K	77 K	10 K	Cooling rate
	(μs)	(μs)	(μs)	(μs)	(K/s)
500 nm	613	1409	2467	12000	1.8×10^5
200 nm	224	476	821	3007	4.9×10^5
50 nm	55	110	185	539	2.2×10^6
10 nm	12	23	37	103	1.1×10^7
Lysozyme	6	10	16	40	2.6×10^7

Table 6.1: **Cooling rate in the buffer-gas cell for different particle sizes.** Calculated cooling rates at a fixed flow rate of $70 \text{ ml}_n/\text{min}$ and the corresponding cooling times for reaching relevant temperatures, such as the protein glass-transition (200 K), water glass transition (133 K), and liquid nitrogen (77 K) temperatures. The cooling rates have an estimated error of 10 %, propagated from the 10 % error in the Nusselt number [123].

modeled temperature drop as a function of time as the particle traveled through the buffer-gas cell and the instantaneous cooling rates are shown in Figure 6.11 and S8, along with results for a simpler momentum-transfer-based cooling model. These simulations show that for particles smaller than $\sim 50 \text{ nm}$ cooling rates on the order of 10^6 – 10^7 K/s can be achieved. This significantly exceeds the cooling rates for the plunge-freezing approach commonly used in CEM [126, 127]. Furthermore, the simulations show that the cooling rate strongly depends on the initial position of the warm nanoparticle in the cold cell, i. e., on the local helium density, and on the particles' velocity distribution. This provides the way forward toward even faster cooling: Moving the position of the heated inlet capillary into the buffer-gas cell will put the warm particles immediately into regions of higher-helium density. Decoupling the initial-cooling cell from the fluid-dynamic focusing,

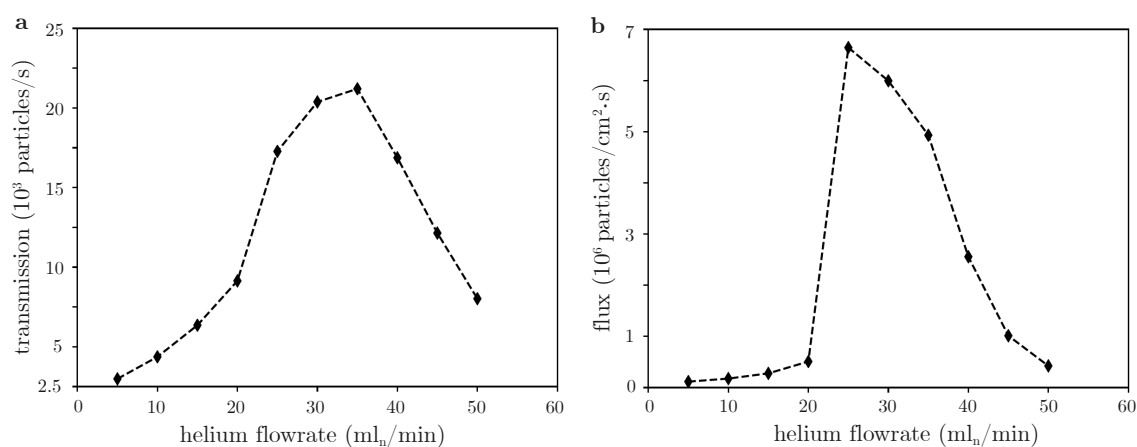


Figure 6.9: **Experimentally obtained transmission and average flux of particles** for 220 nm PS spheres as a function of helium flow at the detector position, i. e., 10 mm behind the buffer-gas cell outlet. (a) The transmission shows the number of all particles that were detected by particle-localisation microscopy as a function of helium flow rate. (b) The corresponding average particle fluxes were calculated from these particle numbers, the camera exposure times, and the corresponding particle beam diameters.

e. g., in double-cell configurations [116], would allow orders of magnitude higher densities of cold helium at the inlet, providing correspondingly faster cooling. This two-cell setup

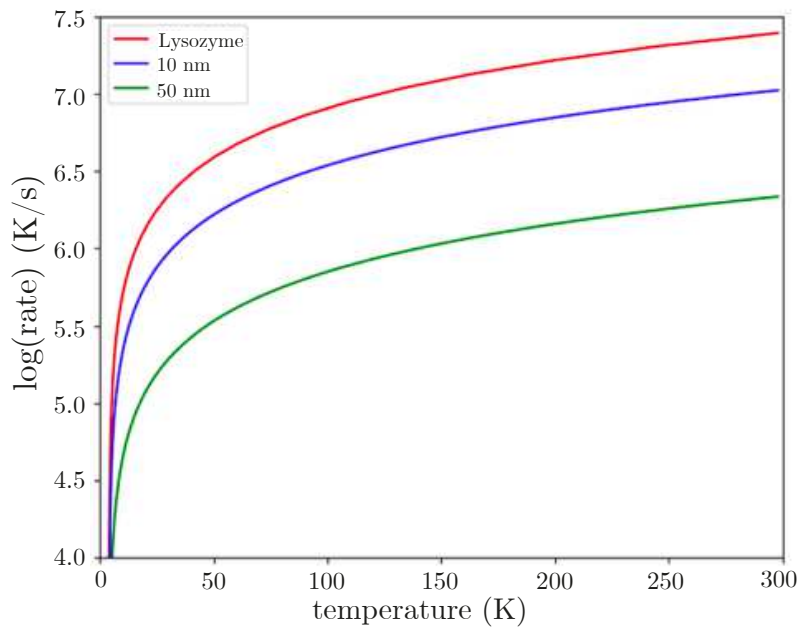


Figure 6.10: **Rate of cooling as a function of temperature** for 50 nm (green) and 10 nm (blue) PS particles and Lysozyme (red), calculated assuming forced convection and Newton's law of cooling and took into account the particles initial internal energy at room temperature.

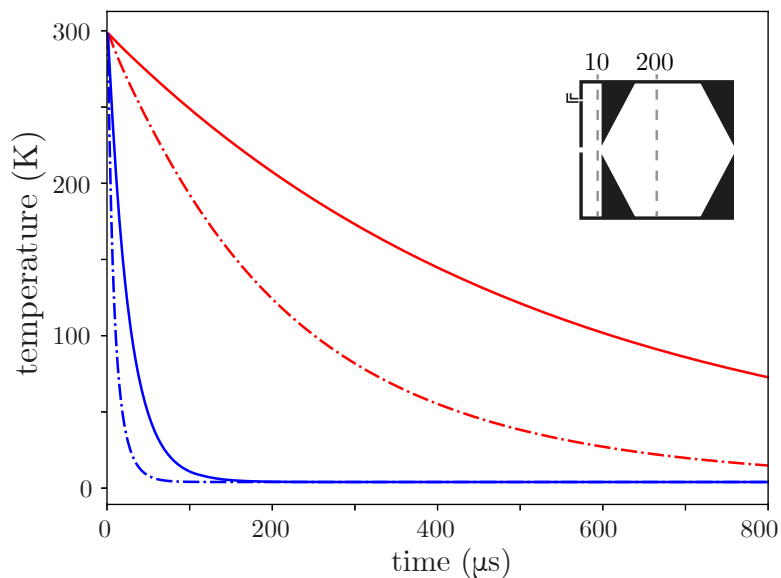


Figure 6.11: **Simulated thermalization times of nanoparticles** for 200 nm (red) and 10 nm (blue) PS particles. We have used both, forced convection with Newton's law of cooling (solid lines) and the simpler momentum-transfer-based cooling (dashed lines), models to simulate the thermalization. The inset of the figure also shows the position within the cell, indicated by the dashed line, where the nanoparticles were completely thermalized to the buffer gas temperature.

will also enable further control of the fluid-dynamic focusing at the outlet [94], enabling strongly increased particle densities in the focus. Besides higher densities and better shock-freezing of biological samples, such improvements and corresponding variability in the experimental parameters would also enable studies of possible effects of the freezing rate on the structure of biological macromolecules.

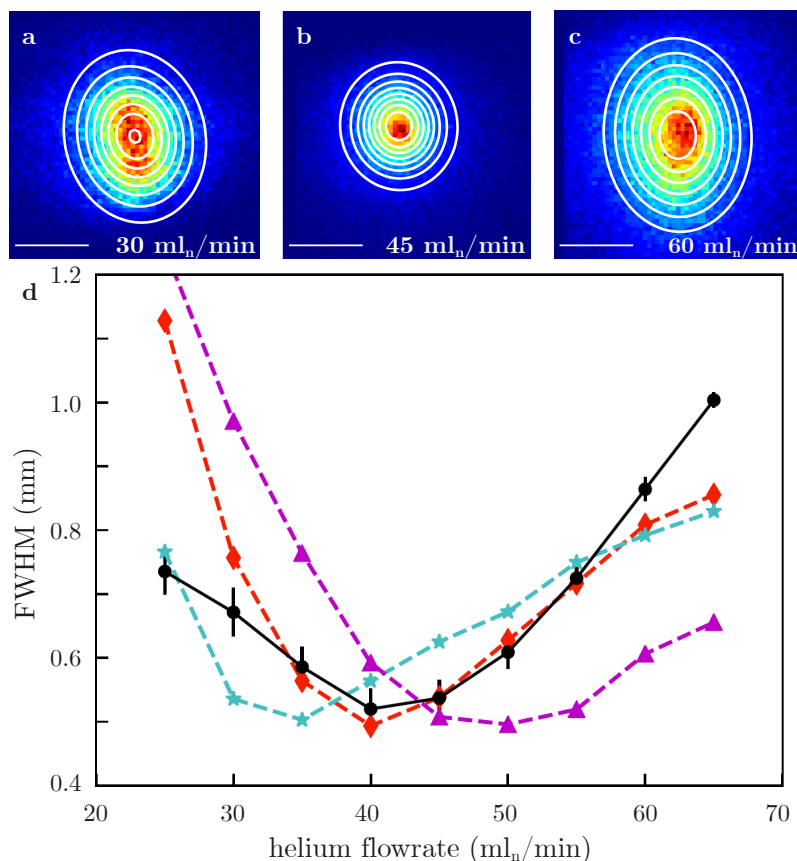


Figure 6.12: **Shock-freezing and focusing Granulovirus occlusion bodies.** (a, b, c) Experimental particle-beam profiles at the detector position for three different helium flow rates of 30, 45, and 60 ml_n/min, respectively. Scale bars and color codes are same as Figure 6.2. (d) Experimental (black) and simulated (cyan, red and purple) particle beam widths as a function of helium flow rate. Simulations are shown for three different hydrodynamic diameters: 280 nm (cyan), 320 nm (red) and 360 nm (purple), confirming the expected effective hydrodynamic diameter of 320 nm for CpGV.

To study the applicability of our approach to non-spherical biological nanoparticles, we created a cryogenically cooled beam of CpGV. CpGV is readily available commercially as an insecticide alternative to control codling moth populations [128]. The resulting focusing curves following injection of CpGV into the buffer-gas cell are shown in Figure 6.12. As previously observed for PS, the size of the produced particle beam at the detector showed a strong dependence on the helium flow rate, with the narrowest profile and highest density observed for helium flow rates of 40–45 ml_n/min. Our current simulation approach inherently assumes spherical particles. Therefore, to model the CpGV data we simulated spherical particles of various sizes with the known density of CpGV of 1160 kg/m³. Simulations for diameters of 280 nm, 320 nm and 360 nm are shown in Figure 6.12 and the best fit was observed for a particle size of 320 nm as an effective

fluid-dynamic diameter for CpGV. This value is in good agreement with the 325 nm obtained as the geometric mean of CpGV's 3D diameters. This indicates that particles inside the buffer-gas cell are freely rotating and no significant flow-alignment effects occur under the experimental conditions of our study. Furthermore, these simulations confirm that also biological particles leave the buffer-gas cell thermalized with the cold helium gas.

6.4 Conclusion and outlook

We have demonstrated a cryogenic nanoparticle source capable of producing tightly focused beams of shock-frozen aerosolized nanoparticles and its quantitative description. Using a helium buffer-gas cell, isolated room-temperature particles are rapidly cooled, typically reaching liquid nitrogen temperatures within hundreds of microseconds, and quickly thermalizing with the buffer gas at 4 K. The current outlet of the cell acts as a simple fluid-dynamic lens, efficiently extracting particles and forming a focused beam. These beams were characterized through particle-localization microscopy. The cooling and focusing properties can be tuned by varying the helium flow-rate and its temperature. A novel numerical simulation infrastructure was set up to provide quantitative simulations of particle trajectories and phase-space distributions, which are in very good agreement with the measurements. These simulations then enabled the extraction of cooling rates and particle temperatures, highlighting the very fast shock-freezing of nanoparticles. Last, but not least, we demonstrated the applicability to non-spherical biological nanoparticles by producing beams of shock-frozen granulovirus particles. Further improvements of the setup will provide orders of magnitude faster cooling rates of the particles as well as better focusing of the emerging beams: The initial cooling can be improved by placing the particle inlet into the buffer gas cell and through two-cell approaches from small-molecule buffer-gas cooling [116]. The latter will also allow for advanced fluid-dynamic focusing outlets [94] resulting in strongly increased particle densities in the focus. The demonstrated high-flux beams of shock-frozen nanoparticles will be beneficial to a wide range of experiments in structural biology, nanoscience, and physics, including high-resolution single particle x-ray and electron diffractive-imaging. In particular, our approach, together with control and selection, will overcome the sample variability problem typically encountered in single-particle coherent x-ray diffraction measurements, where millions of particles are needed to create a 3D structure [7]. Furthermore, the beams of cold isolated particles open up a large tool-box of control methods, originally developed for cold small gas-phase molecules [82, 129], to these large nanoscale systems. These include the separation of structural isomers or major folding structures [82, 109, 130] or molecular alignment approaches that fix molecules in the laboratory frame using optical fields [3, 112, 129, 131, 132]. Such control would enable the experimental averaging of imaging data over many identical molecules/particles. Furthermore, it provides the prerequisites for future time-resolved studies of ultrafast biochemical dynamics, which require well-defined starting states to controllably and reliably trigger specific dynamic processes of interest. Additionally, the ability to control the particles final temperature and cooling rate will allow the exploration of the ground-state potential energy landscape and answer important outstanding questions regarding the preservation of native-like conditions upon rapid-freezing. It furthermore enables the direct study of important temperature and size dependent phenomena in artificial nanoparticles, such as extremely large magnetoresistance [133] or light-induced superconductivity [134]. Furthermore, it could propel matter-wave interference to new limits [135].

Our approach enables imaging experiments that bring the benefits of CEM, well-controlled and static sample particles, to single-particle imaging where they can be imaged *in vacuo* without support structures and with ultrafast time-resolution. In turn, combining the very fast cooling enabled by our approach with soft-landing techniques could bring strong and crucial progress to the sample delivery in CEM experiments.

7 Microscopic force for aerosol transport¹

A key ingredient for single particle diffractive imaging experiments is the successful and efficient delivery of sample. Current sample-delivery methods are based on aerosol injectors in which the samples are driven by fluid-dynamic forces. These are typically simulated using Stokes' drag forces and for micrometer-size or smaller particles, the Cunningham correction factor is applied. This is not only unsatisfactory, but even using a temperature dependent formulation it fails at cryogenic temperatures. Here we propose the use of a direct computation of the force, based on Epstein's formulation, that allows for high relative velocities of the particles to the gas and also for internal particle temperatures that differ from the gas temperature. The new force reproduces Stokes' drag force for conditions known to be well described by Stokes' drag. Furthermore, it shows excellent agreement to experiments at 4 K, confirming the improved descriptive power of simulations over a wide temperature range.

7.1 Introduction

The functionality of molecules and materials is strongly correlated to their atomic structure. Currently, biomolecules with sizes of a few nanometers are of particular interest for visualizing their high-resolution atomic structure in order to unravel the secrets of life and for developing, e. g., pharmaceuticals or novel biomimetic materials. With the advent of modern XFELs SPI has become feasible [4, 11, 15, 71, 136]. SPI allows to retrieve the 3D atomic structure of nanoparticles by processing a series of two dimensional diffraction patterns of the corresponding isolated nanoparticles *in silico*.

SPI does not rely on highly-ordered crystalline sample, as in x-ray crystallography [6], nor on a mechanical sample support as in CEM [105, 106]. However, its diffraction-before-destruction approach [4] requires constant replenishment of identical targets in order to collect the necessary number of diffraction patterns for the 3D reconstruction. Sample sources are typically aerosol injectors producing tightly focused streams of nanoparticles [11]. However, the efficient delivery of identical nanoparticles is still a bottleneck for SPI experiments [137]. Our recently reported approach of using a cryogenic buffer-gas cooled aerosol injector [138] promises to overcome this limitation by increasing the reproducibility and control over the sample. There aerosolized nanoparticles were transported into a cryogenically-cooled helium-filled buffer-gas cell, where the nanoparticles were rapidly cooled [138]. The low temperature reduces particle losses and broadening of the stream due to diffusion, and it allows for better subsequent nanoparticle control [82, 114, 115].

Generally, for best performance it is necessary to optimize the geometry of aerosol injectors and the flow conditions of the carrier gas for every individual nanoparticle sample. For SPI experiments at room temperature simulations have already shown to be a useful tool to get insights on the sample delivery process and to aid during optimization [94]. However, for the cryogenic buffer-gas cell an improved description of the interaction between the gas and the nanoparticles is required for a better understanding of the particles' trajectories and phase-space distributions. These simulations should also reliably predict the final temperature of the nanoparticles and their cooling rate, an important aspect of buffer-gas cooling [138].

¹This chapter is based on the publication: N. Roth, M. Amin, A. K. Samanta, and J. Küpper. "Microscopic force for aerosol transport", (2020). I developed the physical model, performed and analyzed the simulations and wrote and discussed the manuscript.

A general theory for describing the forces of an aerosol in a gas flow has yet to be found. For the purpose of modelling particle trajectories through aerodynamic focusing devices it is important to consider the usual working conditions that apply during the experiment. The pressure regimes can be described by the Knudsen number $Kn = \lambda/d_p$, which is the ratio of the mean free path of the fluid λ to the diameter of the particle d_p . In the experiment the pressure ranges, in principle, from atmosphere to ultrahigh vacuum. However, the actual focusing and transport that we are mainly interested in occurs in pressure regimes below 10 mbar, leading to $Kn \geq 100$ for nanometer size particles. The regime with $Kn \gg 1$ is called molecular flow. For this regime the boundary conditions assumed for Stokes famous drag equation do not hold any more and an empirical correction factor to the drag force, called “Cunningham correction factor”, was introduced [41] and quickly improved to today’s formalism [42]. The empirical parameters were determined several times by fitting the drag force to experimental data, mostly from Milikan’s oil droplet experiments [43, 44]. Hence, this original description of the drag force is valid for the exact conditions in Milikan’s experiment, namely, air at room temperature and particles of hundreds nanometers or larger. The Cunningham correction factor depends on the gas and temperature [45] and the temperature-dependent correction factors were derived from kinetic theory considerations and related to experimental data for temperatures from 200 to 1000 K [46]. However, we are now trying to describe experiments in helium gas at temperatures down to 4 K [138].

Another approach to model the force of a rarefied fluid on a particle is to use the kinetic theory of gases. For the momentum transfer from gas molecules impinging and emerging from the surface of a particle, Epstein was able to reproduce the experimental data measured by Milikan by assuming 10 % specular reflection and 90 % diffuse reflection and the particle to be a perfect conductor [47]. This approach is valid across all gas types and temperatures. For particle sizes of current interest, which are in the order of 10–300 nm, the assumptions of a rigid body and the mainly diffuse scattering of Epstein’s model are still good approximations. For smaller systems more advanced treatment might be necessary: For particles with sizes of a few nm specular reflection become dominant and for small molecular sizes the treatment as rigid spheres fails and long range interactions, e. g., van der Waals interactions and electric multipole interactions, have to be taken into account [45].

The dimensions of the current aerodynamic focusing devices are on the order of millimeter to centimeter. When miniaturizing these devices it might become necessary to include forces important for microfluidic channels such as the Saffman force [60].

Epstein’s description would match the experimental conditions [94, 138] if it wasn’t for the large relative velocities between particles and gas and the temperature differences between gas and particles. These effects are incompatible with Epstein’s approach, although we note that Epstein’s model was improved in several ways, e. g., to the description of molecular-size particles based on Chapman-Enskog theory and the kinetic theory of gases [45, 49], by accounting for quantum effects [50], by deriving an analytical expression for the ratio between specular and diffuse reflection [52], through molecular dynamics simulations [53–55], or for non-isothermal fluids [56, 57] and lift forces due to the rotation of the particle or the velocity gradient in the flow field [58–60]. Unfortunately, none of these advances treated the needed adaptation for our experimental conditions, although they were derived for a flat surface [139]. Here, we extended this to formulate a new specific model based on Epstein’s original approach for spherical particles. Our model allows for different temperatures between the particle and the gas and it also is not limited to small relative velocities between gas and particle.

7.2 Modeling the particle transport in an aerosol injector for SPI Experiments

7.2.1 Drag force in an aerosol injector for SPI experiments

For molecular flow the mean free path of the gas is much larger than the diameter of the particle. Hence, it is a valid assumption that the presence of the particle does not change the gas flow, e. g., the velocity distribution of the gas molecules. Assuming a Maxwell distribution, the number of gas molecules with velocities between (v_x, v_y, v_z) and $(v_x + dv_x, v_y + dv_y, v_z + dv_z)$ is

$$N_{v_x, v_y, v_z} dv_x dv_y dv_z = N \left(\frac{h}{\pi} \right)^{\frac{3}{2}} e^{-h(v_x^2 + v_y^2 + v_z^2)} dv_x dv_y dv_z, \quad (7.1)$$

with

$$h = \frac{m}{2kT}, \quad (7.2)$$

where N is the Number of molecules per unit Volume, m is the mass of the gas molecule, k is the Boltzmann constant and T is the gas temperature. From the point of view of a particle moving in a gas with speed U and velocity components $U_x = \alpha U$, $U_y = \beta U$ and $U_z = \gamma U$, with velocities along the x, y, z axes according to the fractions of speed α, β, γ , the velocity distribution is

$$N_{v_x, v_y, v_z} dv_x dv_y dv_z = N \left(\frac{h}{\pi} \right)^{\frac{3}{2}} e^{-h((v_x + \alpha U)^2 + (v_y + \beta U)^2 + (v_z + \gamma U)^2)} dv_x dv_y dv_z. \quad (7.3)$$

To determine the amount of gas molecules that hit the particle we assumed a surface element dS of the particle normal to the x direction. The volume that contains all particles with velocity $v_x + dv_x$ that will hit the surface in unit time is given by $v_x dS$ and the amount of particles in this volume is

$$n_{v_x, v_y, v_z} dv_x dv_y dv_z dS = v_x N_{v_x, v_y, v_z} dv_x dv_y dv_z dS. \quad (7.4)$$

The amount of momentum transferred to the particle in a given direction by an individual gas molecule impinging and sticking to the particle is given by $m(\alpha' v_x + \beta' v_y + \gamma' v_z)$. For a sphere with radius R , the z -axis defined to be normal to the plane through x and U , and the angle θ between y and U we obtain $\alpha = \cos(\theta)$, $\beta = \sin(\theta)$, $\gamma = 0$. Furthermore, for the momentum transferred in the direction of U we obtain $\alpha' = \cos(\theta)$, $\beta' = \sin(\theta)$, $\gamma' = 0$. The total amount of momentum transferred in the direction of U can be calculated analog to Epstein's model [47], directly using (7.3) instead of an approximation for small U , by integrating over all surface elements $dS = R^2 \sin(\theta) d\theta d\phi$ and all gas molecules impinging the particle in unit time. The amount of gas molecules impinging the particle per time is constant in the statistical limit, so is the momentum transferred per time, the force. It is given by

$$F_{\text{imp}} = \frac{p\sqrt{\pi}R^2}{2hU^2} \left(-2e^{-hU^2} \sqrt{h}U (1 + 2hU^2) + \sqrt{\pi} (1 - 4hU^2 - 4h^2U^4) \operatorname{erf}(\sqrt{h}U) \right). \quad (7.5)$$

For specular reflection the x component of the velocity U of all gas molecules is changing

sign, as does α , while everything else stays the same. Performing the integration, the momentum transferred by the reflecting gas molecules, and so the force due to reflection F_r , averages to zero and the total force in case of specular reflection F_{spec} is

$$F_{\text{spec}} = F_{\text{imp}} + F_r = F_{\text{imp}}. \quad (7.6)$$

Calculating the force for diffuse scattering F_{diff} requires to appropriately take the temperature difference between the gas and the particle into account. Assuming the gas molecule to thermalize to the particle's temperature during accommodation and it thus leaving the particle with a Maxwell Boltzmann distribution according to the particles temperature [47], it is possible to calculate the amount of momentum transfer by considering the conservation of the number of gas molecules:

$$n_{v_x, v_y, v_z, \text{imp}} dv_x dv_y dv_z dS = n_{v_x, v_y, v_z, \text{leav}} dv_x dv_y dv_z dS \quad (7.7)$$

The left side of (7.7) is identical to (7.4) and

$$n_{v_x, v_y, v_z, \text{leav}} = C_{\text{leav}} e^{-h'(v_x^2 + v_y^2 + v_z^2)}. \quad (7.8)$$

h' is defined equivalent to (7.2), but using the temperature of the particle instead of the gas temperature. By integrating (7.7) over the whole surface and all velocities, C_{leaving} is determined and thus the force on the particle:

$$F_{\text{diff}} = F_{\text{imp}} - \frac{2}{3} \frac{h}{\sqrt{h'}} p (\pi)^{\frac{3}{2}} R^2 U \quad (7.9)$$

The derivation is analog to the derivations in [47], but with the additional h' . The total force is assumed to be a combination of 10 % specular reflections and 90 % diffuse reflections [47]:

$$F_{\text{total}} = 0.1 F_{\text{spec}} + 0.9 F_{\text{diff}} \quad (7.10)$$

7.2.2 Temperature changes of the aerosol

The drag force (7.9) on a particle depends on its temperature. In the process of diffuse scattering the gas molecules are assumed to thermalize to the particle's temperature. This means, that the velocity distribution of the impinging gas molecules differs from the velocity distribution of the reflected ones not only due to U , but also due to different temperatures. Depending on whether the particle's temperature is higher or lower than the gas temperature, the gas molecules take away energy from or deposit energy in the particle, respectively, in addition to the energy deposited in kinetic energy of the particle due to U . We assume this additional energy change will exclusively lead to a change in particle temperature, because it is even present with $U = 0$. Integrating over all molecules that hit the particle in unit time the change in energy is

$$\begin{aligned} \Delta E = & \frac{p\sqrt{\pi}R^2}{4hh'} \left(-2e^{-hU^2} \sqrt{h} \left(5h' + 2h \left(2 + h'U^2 \right) \right) \right. \\ & - \frac{\sqrt{\pi} \operatorname{erf}(\sqrt{h}U)}{U} \left(3h' + 4h^2U^2 \left(2 + h'U^2 \right) \right. \\ & \left. \left. + 4h \left(1 + 3h'U^2 \right) \right) \right) \end{aligned} \quad (7.11)$$

which for small values of U , using the same velocity approximation as in Epstein's model, simplifies to

$$\Delta E = \frac{4p\sqrt{h\pi}R^2}{h'} - \frac{4p\sqrt{\pi}R^2}{\sqrt{h}} \quad (7.12)$$

A change of the particle's temperature is considered as a change ΔE of the total energy stored in all its degrees of freedom, i. e., its specific heat c_p . Thus the change in particle temperature per unit time is

$$\Delta T = \frac{\Delta E}{c_p m_p}, \quad (7.13)$$

with the particle's mass m_p .

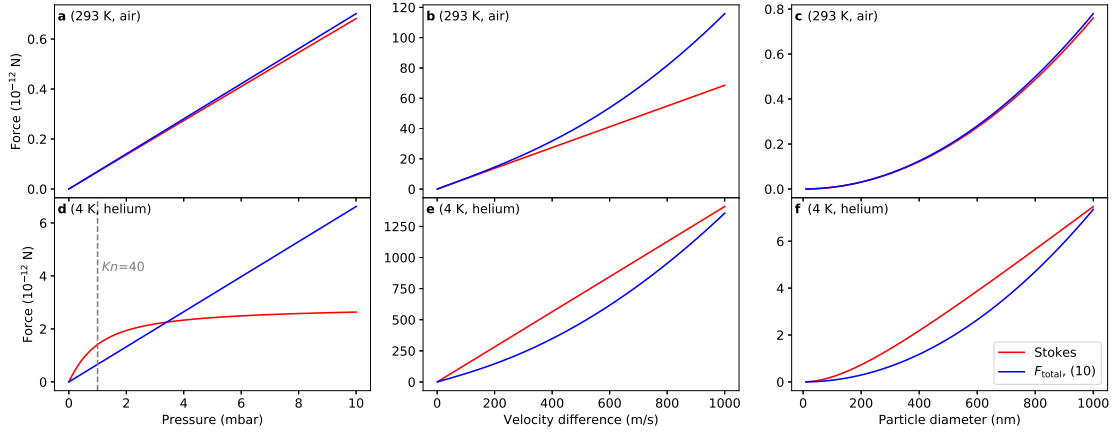


Figure 7.1: Calculated drag force (7.10) in comparison to Stokes' drag force as a function of (a, d) pressure, (b, e) velocity difference, and (c, f) particle diameter at (a–c) room temperature and (d–f) 4 K. Stokes' drag force was calculated as described by [94] for room temperature and as described by [138] for 4 K. While one of the parameters is varied the others are fixed at 1 mbar, 1 m/s, and 300 nm, respectively. The dashed gray line in (d) indicates the pressure where $Kn = 40$; see text for further details.

7.2.3 Brownian Motion

So far we calculated the force by averaging over all single collisions the particle undergoes per unit time, which appropriately predicts the mean force on the particle. However, its actual trajectory depends further on its Brownian motion. For a numerical description of the Brownian motion using the Langevin equation [61] the force on the particle is split into a part F_{drag} that is proportional to U and a part F_b that is a random force. F_{drag} is in our case Equation 7.10, but using the same velocity approximation as in Epstein's model. F_b is assumed to be white noise consisting of an amplitude A and a random number r with zero mean and unit variance. The fluctuation-dissipation theorem defines the amplitude of the random force to be

$$A = \langle F_b(t_1)F_b(t_2) \rangle = 2kT\mu\delta(t_1 - t_2), \quad (7.14)$$

with $\mu = F_{\text{drag}}/U$. F_b considers the particle at rest with the gas and μ is calculated for the case of small U , where F_{total} is proportional to U . With a numerical representation of the

delta function with a time step size Δt the Brownian force is

$$F_b = r \sqrt{\frac{\left(\frac{16}{3} + \frac{2}{3}\pi\sqrt{\frac{h}{h'}}\right) \sqrt{\frac{\pi}{h}} pmR^2}{\Delta t}}. \quad (7.15)$$

7.3 Benchmarking the new force

7.3.1 Comparison to Stokes' drag force

In order to validate the new force, i. e., the model derived above, we compare it to the established model of Stokes' drag force, which is known to produce reliable results for specific conditions, *vide supra*. Figure 7.1 shows the calculated values of the new proposed drag force compared to Stokes' drag force in dependence of the gas pressure, the velocity difference between particle and gas, and the particle diameter for room temperature and 4 K, respectively.

For room temperature, Figure 7.1 a–c, and in a regime comparable to that in the Millikan experiment both models lead to nearly identical results. When the velocity differences becomes larger than 200 m/s the models diverge, which is expected as Stokes' drag force is only applicable for comparable slow flows [140], whereas (7.10) appropriately describes that not only the amount of momentum transferred per gas molecule depends on U , but also the amount of gas molecules that hit the particle increases significantly when U approaches values comparable to the average speed of a single gas molecule.

For a cold gas at 4 K, Figure 7.1 d–f, the functional behavior of the models differ. Here, Stokes' force [46] is calculated as described by [138]. For low pressures (large Kn) both forces have a linear pressure dependency, but with a flatter slope in case of (7.10). In general the results from (7.10) are below the calculated forces using Stokes in this region. However, for high pressures (small Kn) Stokes' force approaches a constant value. The transition occurs around 1 mbar ($Kn \approx 40$). It is important to note that the region on the left to that transition ($Kn \gg 1$) is the region where the assumption for (7.10), that the presence of the particle is not influencing the gas flow, holds. Smaller predicted magnitudes of the force using (7.10) can be observed in Figure 7.1 e,f as well. These lower values are in accordance with our previous experience using Stokes' force at these conditions: In order to successfully describe the available experimental data using Stokes' force, it was necessary to scale the force down by roughly a factor of 4 [138].

7.3.2 Comparison to Newton's law of cooling

We validated the cooling rates (7.13), using (7.11), of our model against Newton's law of cooling [138]. The resulting cooling rates are shown in Figure 7.2. Newton's law of cooling and our model show the same qualitative behaviour. As expected they both linearly depend on the temperature difference between the particle and the gas. Also the dependencies of pressure and particle diameter are very similar. In general, our new model leads to overall somewhat higher cooling rates, with the largest deviations roughly within a factor of two of Newton's law of cooling.

The calculations of cooling rates using Newton's law of cooling involve several empirical approximations in the calculation of the Nusselt number and the heat transfer coefficients for forced convection [138]. In addition, another empirical parameter is needed to correct for the rarefied gas regime. The only empirical value in the new model (7.13) is the specific heat of the particle. Thus, it comes by no surprise, the two models do not produce identical

quantitative results and the agreement we can see in Figure 7.2 a–c is pretty good, with (7.13) being a much clearer, hence more trustworthy, model.

Figure 7.3 shows calculated cooling rates using the full model (7.11) and the approximation for small velocities (7.12) for the change in energy. Up to relative velocities of 100 m/s the calculated cooling rate does not strongly depend on velocity and the approximation of small velocities is applicable. Hence, depending on the system of interest, it is a valid approach to use this assumption for the sake of computational speed.

7.3.3 Comparison to experimental Results

We compared our model against recent experimental and computational results for the focusing of polystyrene spheres of diameter 220 nm in a helium buffer gas cell at 4 K [138]. Figure 7.4 shows the FWHM of the particle beams 10 mm behind the outlet of a cryogenic buffer-gas cell as a function of the helium flow rate, i. e., differing pressures and velocities.

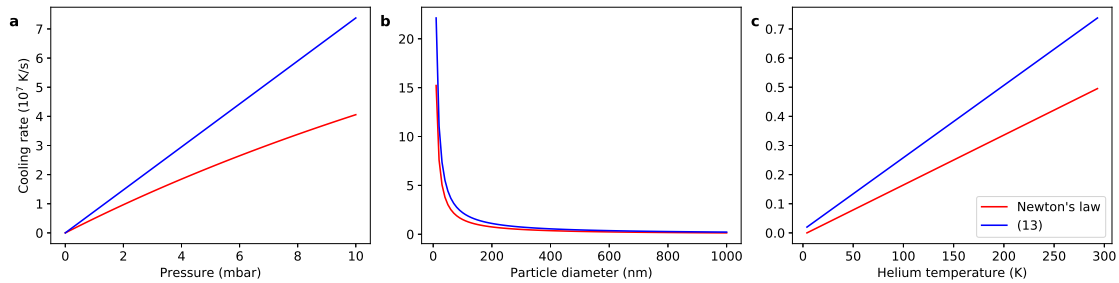


Figure 7.2: Calculated values of the cooling rate (7.13) compared to Newton's law of cooling and its dependence on (a) pressure, (b) particle diameter, and (c) initial temperature of the particle for a polystyrene sphere in helium at 4 K. While one of the parameters is varied the others are fixed at 1 mbar, 300 nm., 293.15 K and 0.1 m/s.

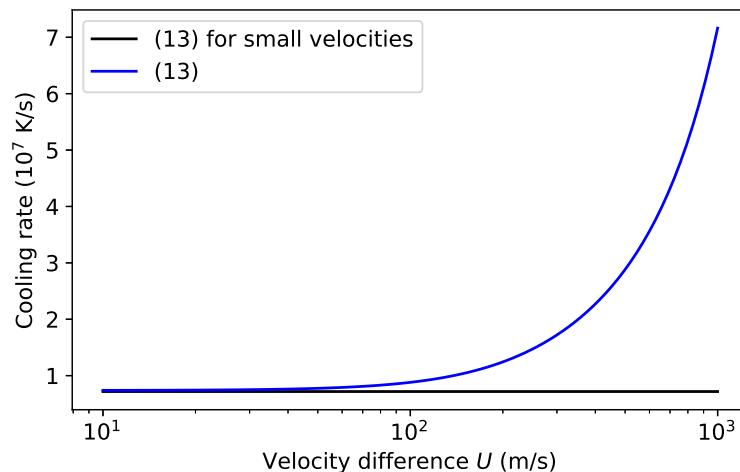


Figure 7.3: Cooling rate as a function of the velocity difference U for a 300 nm polystyrene sphere in helium at 4 K and 1 mbar, calculated with (blue) the full model (7.13) and (black) the approximation for small velocity differences between particle and gas.

The 2D transverse distribution of the particle beam was fitted by a 2D Gaussian in order to obtain the FWHM. As expected, Stokes' drag force, even with a temperature dependent slip

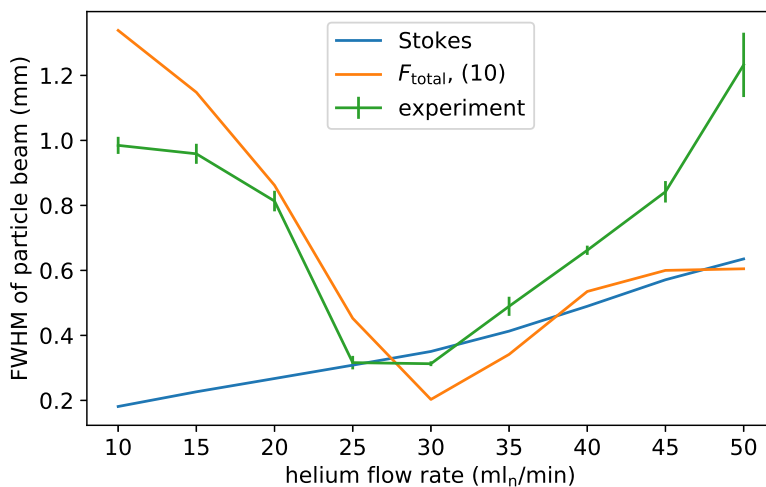


Figure 7.4: The FWHM of the particle beam transverse position 1 cm after the buffer gas cell for different helium mass flows, simulated using the temperature-dependent Stokes' drag force [46], simulated using (7.10), and experimentally measured. The 2D transverse distribution of the particle beam was fitted by a 2D Gaussian in order to obtain the FWHM

correction, does not reproduce the experimental results at all, because it overestimates the force (*vide supra*). Only by scaling it down by a factor of 4 as in Fig. 4 of [138] comparable results can be achieved.

The simulations using the microscopic drag force (7.10) together with the Brownian force (7.15) derived here reproduce these experimental result very well, validating our simulation framework.

7.4 Conclusion

We have developed a new description of the flow of nanoparticles through a fluid, or the flow of a fluid past an object, which works over a large range of pressures, relative velocities, particle sizes, and temperatures. The model follows the ideas of Epstein's formulation of the drag force and does not require additional empirical adjustments of the force. We have verified the model against Stokes' drag force in the regime where the latter is valid and against experimental results for nanoparticles at cryogenic temperatures. Our new description works very well over this wide range of conditions.

The accurate descriptions enabled by our model are an important ingredient, for instance, for optimized sample injection in single-particle diffraction experiments: Hit rates can be significantly improved through reliable predictions of injection parameters before the actual measurement campaign at the large-scale facility. This does not only improve data quality, but allows to make much better use of the expensive x-ray pulses and thus enables better science.

As another benefit, the new model directly provides the particles' temperatures and thus the cooling rate in the gas, which is important, for instance, for the shockfreezing of biological samples.

However, while our model is a good description for the conditions in current SPI experiments, the envisioned advances to single-molecule samples, i. e., proteins or other macromolecules with sizes of a few nanometers, will necessitate an advanced description of the nanoparticle-gas collisions [45, 49].

The model is implemented in our larger CMInject software package for the simulation of generic aerosol injectors, which we currently prepare for publication.

8 Conclusion

Single-particle diffractive imaging is a promising technique to unravel a lot of biochemical and physical properties and mechanisms of large and complex molecules, such as proteins or viruses. While the brilliance of current XFEL sources is high enough to make SPI experiments feasible, using single particles still provides a very limited signal to noise ratio, especially, when moving towards smaller samples in the few ten nm size regime. Hence, a lot of diffraction patterns of these molecules in random orientations are needed to reconstruct the 3D structure. Since the brilliance and repetition rate of the x-rays and the measurement time are limited by the XFEL facility, it is necessary to utilize the given amount of x-ray pulses to its maximum, preferably creating a diffraction event with every x-ray pulse.

Advancing the experimental tools for sample delivery is a key step. Aerosol injectors are currently the best choice, because of their reduced background compared to liquid jet based methods. The local density of sample aerosols in the focus volume of the x-ray provided by the used aerosol injector in these experiments defines, together with the used XFEL source, the possible efficiency, hence, the achievable result within a given time frame, available for experiments at a XFEL beamline. Improving aerosol injectors necessitates extensive understanding of its current performance and operating conditions.

In chapter 3 a novel methodology for measuring local pressures, e. g., at aerosol injector tips, is reported. Helium densities down to $4 \times 10^{16} \text{ cm}^{-3}$ with a spatial resolution of a few μm could be detected.

Iterative improvements of aerosol injectors need a fast feedback cycle and the simulation environment reported chapter 4 has proven to be able to predict the behaviour of an ALS. Measured particle beam profiles of 500 nm PS generated by an ALS were compared to corresponding simulated profiles with good quantitative agreement for different injection conditions. The predictions are reliable enough to partly replace extensive and time consuming experimental characterization. The simulations are not only able to significantly speed up the optimization process, but are giving insights in the functionality of ADLs and aerosol injectors. They are unravelling short comings of current geometric designs and providing knowledge, not only which operation conditions lead to higher injection efficiency, but also why. The simulation results of chapter 4 revealed the sources for transmission losses at specific injection conditions. Additionally for ALSs that are not optimized for a specific sample size a mechanism that leads to an increased population of particles at higher radial positions could be observed and explained. This gained knowledge drove the design of a new ALS, that is able to be changed in geometry, hence, to be optimized for different samples and experimental conditions much faster. The first experiments described in chapter 5 using this injector proved not only the functionality, but also ensured the predictive power of the developed simulation framework.

While it is important to achieve the desired local density of the sample, SPI experiments need a stream of identical sample. At room temperature a lot of samples of interest constantly change their confirmation. Cooling enables the control over these internal degrees of freedom in addition to the translational ones controlled by the aerodynamic forces. Cooling of biomolecules was achieved in chapter 6 by setting up a BGC operated with helium at 4 K. PS and CpGV were shockfrozen and transferred into an aerosol beam by the BGC. An efficient use of this new source for SPI would necessitate geometric optimization of the buffer-gas cell. Taking all the added complexity of the injection set-up, by e. g., the cryostat into account, makes optimization solely by experimental characterization nearly impossible. In addition, the internal temperature of the sample

particle adds a new relevant parameter, that is inaccessible via measurements in the laboratory. Again simulations have proven to be capable of taking the lead in describing and characterizing the experiment. Simulations not only described the particle trajectories, but also provided a prediction for cooling rates much higher compared to plunge-freezing achievable with this set-up.

Especially the improved model reported in chapter 7 for calculating the force of a rarefied gas at any temperature on spherical particle was an important step. In contrast to Stokes' equation, it uses kinetic theory of gas and extends Epstein's model. It allows for different temperatures of the particle and the surrounding gas and includes the calculation of particle temperature changes. It provides comparable results to Stokes's equation for conditions where Stokes's equation is considered to be applicable and is able to describe the experimental data from chapter 6 without any additional empirical corrections, which were necessary using the Stokes based force model. This way the new model allows for designing advanced buffer gas cell geometries optimized not only for high density output beams but also fast shock freezing.

So far the here performed optimizations on the injection set-up do not yet enable ground breaking new experiments. The main achievements of this work is to provide the necessary tools in order to be able to do so. Up until now the injection system as a whole, including the aerosolization, the differential pumping and transportation, as well as the ALS itself, was a black box. Transmission losses could be observed, but it was not possible to identify in which part of the injection system the sample was lost. With the simulation framework this is now possible. Geometric optimizations are not limited to the ALS. Simulations have shown, that, especially the nozzle skimmer assembly needs to be tuned for different samples as well. Even the transport tube is a source of losses, when moving towards samples with sizes of 10 nm and smaller. With the goal of sub 10 nm biomolecules in mind, diffusion is currently the greatest challenge for providing high density particle beams with minimal losses. In the classical ALS design with tubes and apertures, the sample beam is compressed by the aperture. The tube between the apertures ensures the flow field and the sample particles to move parallel to the central axis again before the next aperture is reached. This allowed to decouple individual ADLs in an ALS to some extent for better understanding. In such an assembly small particles will diffuse away from the center towards the walls, before they reach the next ADL. A sufficient transportation and compression will not be possible this way. The simulations do not need to decouple individual ADLs in order to provide predictions of the resulting particle beam. Apertures can be placed at much closer distance. This way optimizations are not limited to the basic shapes of a typical ALS. Automating the *in silico* optimization could lead to surprising new shapes. With the new flexible ALS design any internal geometric assembly can be inserted, while being only limited by its length and the maximum diameter. Another huge impact on the diffusion of the sample is the temperature. Using a BGC at cryogenic temperatures reduces the diffusion broadening substantially. Combining the buffer gas cell with an optimized ALS geometry, even a classical one, could provide local particle densities of sub 10 nm proteins high enough to perform an SPI experiment using current XFEL facilities.

Of course seeing the necessity for simulations and also the potential enabled by the improved simulation model, it seems likely that in the future even more advanced models should be used. Going for sample in the size range of a few nm holds a lot of new challenges for the force model. Overall this work laid the foundation for developing new aerosol injectors for any experiment, that requires lot of control over the translational and internal degrees of freedom of aerosolized sample in the size range from ten to several hundred nm and potentially even smaller.

Bibliography

- [1] E. Schrödinger and R. Penrose, *What is Life?: With Mind and Matter and Autobiographical Sketches*, Canto (Cambridge University Press, 1992).
 - [2] A. Pross, *What is Life? How chemistry becomes biology* (Oxford University Press, 2012).
 - [3] E. T. Karamatskos, S. Raabe, T. Mullins, A. Trabattoni, P. Stammer, G. Goldsztejn, R. R. Johansen, K. Długołęcki, H. Stapelfeldt, M. J. J. Vrakking, S. Trippel, A. Rouzée, and J. Küpper, "Molecular movie of ultrafast coherent rotational dynamics of OCS," *Nat. Commun.* **10**, 3364 (2019), arXiv:1807.01034 [physics] .
 - [4] R. Neutze, R. Wouts, D. van der Spoel, E. Weckert, and J. Hajdu, "Potential for biomolecular imaging with femtosecond x-ray pulses," *Nature* **406**, 752 (2000).
 - [5] K. Nass, L. Foucar, T. R. M. Barends, E. Hartmann, S. Botha, R. L. Shoeman, R. B. Doak, R. Alonso-Mori, A. Aquila, S. Bajt, A. Barty, R. Bean, K. R. Beyerlein, M. Bublitz, N. Drachmann, J. Gregersen, H. O. Jönsson, W. Kabsch, S. Kassemeyer, J. E. Koglin, M. Krumrey, D. Mattle, M. Messerschmidt, P. Nissen, L. Reinhard, O. Sitsel, D. Sokaras, G. J. Williams, S. Hau-Riege, N. Timneanu, C. Caleman, H. N. Chapman, S. Boutet, and I. Schlichting, "Indications of radiation damage in ferredoxin microcrystals using high-intensity X-FEL beams," *J. Synchrotron Rad.* **22**, 225 (2015).
 - [6] Y. Shi, "A glimpse of structural biology through x-ray crystallography," *Cell* **159**, 995 (2014).
 - [7] M. Bergh, G. Huldt, N. Timneanu, F. R. N. C. Maia, and J. Hajdu, "Feasibility of imaging living cells at subnanometer resolutions by ultrafast x-ray diffraction," *Q. Rev. Biophys.* **41**, 181 (2008).
 - [8] R. Fung, A. M. Hanna, O. Vendrell, S. Ramakrishna, T. Seideman, R. Santra, and A. Ourmazd, "Dynamics from noisy data with extreme timing uncertainty," *Nature* **532**, 471 (2016).
 - [9] H. N. Chapman, "X-ray imaging beyond the limits," *Nature Mater.* **8**, 299 (2009).
 - [10] D. P. DePonte, U. Weierstall, K. Schmidt, J. Warner, D. Starodub, J. C. H. Spence, and R. B. Doak, "Gas dynamic virtual nozzle for generation of microscopic droplet streams," *J. Phys. D* **41**, 195505 (2008).
 - [11] M. J. Bogan, W. H. Benner, S. Boutet, U. Rohner, M. Frank, A. Barty, M. M. Seibert, F. Maia, S. Marchesini, S. Bajt, B. Woods, V. Riot, S. P. Hau-Riege, M. Svenda, E. Marklund, E. Spiller, J. Hajdu, and H. N. Chapman, "Single particle x-ray diffractive imaging," *Nano Lett.* **8**, 310 (2008).
 - [12] S. Awel, R. A. Kirian, M. O. Wiedorn, K. R. Beyerlein, N. Roth, D. A. Horke, D. Oberthür, J. Knoska, V. Mariani, A. Morgan, L. Adriano, A. Tolstikova, P. L. Xavier, O. Yefanov, A. Aquila, A. Barty, S. Roy-Chowdhury, M. S. Hunter, D. James, J. S. Robinson, U. Weierstall, A. V. Rode, S. Bajt, J. Küpper, and H. N. Chapman, "Femtosecond X-ray diffraction from an aerosolized beam of protein nanocrystals," *J. Appl. Cryst.* **51**, 133 (2018), arXiv:1702.04014 .
-

- [13] M. F. Hantke, D. Hasse, M. R. N. C, T. Ekeberg, K. John, M. Svenda, N. D. Loh, A. V. Martin, N. Timneanu, L. S. D, van der SchotGijs, G. H. Carlsson, M. Ingelman, J. Andreasson, D. Westphal, M. Liang, F. Stellato, D. P. DePonte, R. Hartmann, N. Kimmel, R. A. Kirian, M. M. Seibert, K. Mühlig, S. Schorb, K. Ferguson, C. Bostedt, S. Carron, J. D. Bozek, D. Rolles, A. Rudenko, S. Epp, H. N. Chapman, A. Barty, J. Hajdu, and I. Andersson, "High-throughput imaging of heterogeneous cell organelles with an x-ray laser," *Nat. Photon.* **8**, 943 (2014).
- [14] S. Awel, R. A. Kirian, N. Eckerskorn, M. Wiedorn, D. A. Horke, A. V. Rode, J. Küpper, and H. N. Chapman, "Visualizing aerosol-particle injection for diffractive-imaging experiments," *Opt. Exp.* **24**, 6507 (2016), arXiv:1512.06231 [physics].
- [15] A. Barty, J. Küpper, and H. N. Chapman, "Molecular imaging using x-ray free-electron lasers," *Annu. Rev. Phys. Chem.* **64**, 415 (2013).
- [16] C. Uetrecht, K. Lorenzen, M. Kitzel, J. Heidemann, J. H. Robinson Spencer, H. Schlüter, and J. Schulz, "Native mass spectrometry provides sufficient ion flux for XFEL single-particle imaging," *J. Synchrotron Rad.* **26**, 653 (2019).
- [17] R. A. Kirian, S. Awel, N. Eckerskorn, H. Fleckenstein, M. Wiedorn, L. Adriano, S. Bajt, M. Barthelmess, R. Bean, K. R. Beyerlein, L. M. G. Chavas, M. Domaracky, M. Heymann, D. A. Horke, J. Knoska, M. Metz, A. Morgan, D. Oberthuer, N. Roth, T. Sato, P. L. Xavier, O. Yefanov, A. V. Rode, J. Küpper, and H. N. Chapman, "Simple convergent-nozzle aerosol injector for single-particle diffractive imaging with x-ray free-electron lasers," *Struct. Dyn.* **2**, 041717 (2015).
- [18] M. Dole, L. Mack, R. Hines, R. Mobley, L. Ferguson, and M. d. Alice, "Molecular beams of macroions," *J. Chem. Phys.* **49**, 2240 (1968).
- [19] J. Burgener, "Enhanced parallel path nebulizer with a large range of flow rates," (2003), uS Patent 6,634,572.
- [20] B. J. Daurer, K. Okamoto, J. Bielecki, F. R. N. C. Maia, K. Mühlig, M. M. Seibert, M. F. Hantke, C. Nettelblad, W. H. Benner, M. Svenda, N. Timneanu, T. Ekeberg, N. D. Loh, A. Pietrini, A. Zani, A. D. Rath, D. Westphal, R. A. Kirian, S. Awel, M. O. Wiedorn, G. van der Schot, G. H. Carlsson, D. Hasse, J. A. Sellberg, A. Barty, J. Andreasson, S. Boutet, G. Williams, J. Koglin, I. Andersson, J. Hajdu, and D. S. D. Larsson, "Experimental strategies for imaging bioparticles with femtosecond hard x-ray pulses," *IUCrJ* **4**, 251 (2017).
- [21] G. Scoles, ed., *Atomic and molecular beam methods*, Vol. 1 & 2 (Oxford University Press, New York, NY, USA, 1988 & 1992).
- [22] A. Robinson, "On the motion of small particles in a potential field of flow," *Comm. Pure Appl. Math.* **9**, 69 (1956).
- [23] P. Liu, P. J. Ziemann, D. B. Kittelson, and P. H. McMurry, "Generating particle beams of controlled dimensions and divergence: I. theory of particle motion in aerodynamic lenses and nozzle expansions," *Aerosol Sci. Techn.* **22**, 293 (1995).
- [24] X. F. Zhang, K. A. Smith, D. R. Worsnop, J. Jimenez, J. T. Jayne, and C. E. Kolb, "A numerical characterization of particle beam collimation by an aerodynamic lens-nozzle system: Part I. An individual lens or nozzle," *Aerosol Sci. Techn.* **36**, 617 (2002).
-

-
- [25] X. Zhang, K. A. Smith, D. R. Worsnop, J. L. Jimenez, J. T. Jayne, C. E. Kolb, J. Morris, and P. Davidovits, "Numerical Characterization of Particle Beam Collimation: Part II Integrated Aerodynamic-Lens-Nozzle System," *Aerosol Sci. Techn.* **38**, 619 (2004).
- [26] X. Wang, A. Gidwani, S. L. Girshick, and P. H. McMurry, "Aerodynamic focusing of nanoparticles: II. numerical simulation of particle motion through aerodynamic lenses," *Aerosol Sci. Techn.* **39**, 624 (2005).
- [27] X. Wang and P. H. McMurry, "A design tool for aerodynamic lens systems," *Aerosol Sci. Technol.* **40**, 320 (2006).
- [28] K.-S. Lee, S.-W. Cho, and D. Lee, "Development and experimental evaluation of aerodynamic lens as an aerosol inlet of single particle mass spectrometry," *J. Aerosol. Sci.* **39**, 287 (2008).
- [29] J. Meinen, S. Khasminskaya, E. Rühl, W. Baumann, and T. Leisner, "The TRAPS apparatus: Enhancing target density of nanoparticle beams in vacuum for x-ray and optical spectroscopy," *Aerosol Sci. Techn.* **44**, 316 (2010).
- [30] S. Zherebtsov, T. Fennel, J. Plenge, E. Antonsson, I. Znakovskaya, A. Wirth, O. Herwerth, F. Süßmann, C. Peltz, I. Ahmad, S. A. Trushin, V. Pervak, S. Karsch, M. J. J. Vrakking, B. Langer, C. Graf, M. I. Stockman, F. Krausz, E. Rühl, and M. F. Kling, "Controlled near-field enhanced electron acceleration from dielectric nanospheres with intense few-cycle laser fields," *Nat. Phys.* **7**, 656 (2011).
- [31] M. R. Canagaratna, J. T. Jayne, J. L. Jimenez, J. D. Allan, M. R. Alfarra, Q. Zhang, T. B. Onasch, F. Drewnick, H. Coe, A. Middlebrook, A. Delia, L. R. Williams, A. M. Trimborn, M. J. Northway, P. F. DeCarlo, C. E. Kolb, P. Davidovits, and D. R. Worsnop, "Chemical and microphysical characterization of ambient aerosols with the aerodyne aerosol mass spectrometer," *Mass Spectrom. Rev.* **26**, 185 (2007).
- [32] L. Worbs, J. Lübke, N. Roth, A. K. Samanta, D. A. Horke, and J. Küpper, "Light-sheet imaging for the recording of transverse absolute density distributions of gas-phase particle-beams from nanoparticle injectors," *Opt. Exp.* **27**, 36580 (2019), arXiv:1909.08922 [physics].
- [33] S. Thoroddsen, T. Etoh, and K. Takehara, "High-speed imaging of drops and bubbles," *Annu. Rev. Fluid Mech.* **40**, 257 (2008).
- [34] M. Versluis, "High-speed imaging in fluids," *Exp. Fluids* **54**, 1 (2013).
- [35] C. J. Dasch, "One-dimensional tomography: a comparison of Abel, onion-peeling, and filtered backprojection methods," *Applied Optics* **31**, 1146 (1992).
- [36] E. Betzig, G. H. Patterson, R. Sougrat, O. W. Lindwasser, S. Olenych, J. S. Bonifacino, M. W. Davidson, J. Lippincott-Schwartz, and H. F. Hess, "Imaging intracellular fluorescent proteins at nanometer resolution," *Science* **313**, 1642 (2006).
- [37] R. Henriques, C. Griffiths, E. Hesper Rego, and M. M. Mhlanga, "Palm and storm: Unlocking live-cell super-resolution," *Biopolymers* **95**, 322 (2011).
- [38] B. P. Marsh, N. Chada, R. R. Sanganna Gari, K. P. Sigdel, and G. M. King, "The Hessian blob algorithm: Precise particle detection in atomic force microscopy imagery," *Sci. Rep.* **8**, 978 (2018).
-

- [39] R. B. Miles, W. R. Lempert, and J. N. Forkey, "Laser Rayleigh scattering," *Meas. Sci. Technol.* **12**, R33 (2001).
 - [40] T. Krüger, H. Kusumaatmaja, A. Kuzmin, O. Shardt, G. Silva, and E. M. Vigen, *The Lattice Boltzmann Method - Principles and Practice* (2016).
 - [41] E. Cunningham and J. Larmor, "On the velocity of steady fall of spherical particles through fluid medium," *Proc. Royal Soc. London A* **83**, 357 (1910).
 - [42] M. Knudsen and S. Weber, "Luftwiderstand gegen die langsame Bewegung kleiner Kugeln," *Ann. Phys.* **341**, 981 (1911).
 - [43] R. A. Millikan, "The isolation of an ion, a precision measurement of its charge, and the correction of Stokes's law," *Science* **32**, 436 (1910).
 - [44] R. A. Millikan, "The general law of fall of a small spherical body through a gas, and its bearing upon the nature of molecular reflection from surfaces," *Phys. Rev.* **22**, 1 (1923).
 - [45] Z. Li and H. Wang, "Drag force, diffusion coefficient, and electric mobility of small particles. I. Theory applicable to the free-molecule regime," *Phys. Rev. E* **68**, 061206 (2003).
 - [46] K. Willeke, "Temperature dependence of particle slip in a gaseous medium," *J. Aerosol. Sci.* **7**, 381 (1976).
 - [47] P. S. Epstein, "On the resistance experienced by spheres in their motion through gases," *Phys. Rev.* **23**, 710 (1924).
 - [48] Z. Li and H. Wang, "Drag force, diffusion coefficient, and electric mobility of small particles. II. Application," *Phys. Rev. E* **68**, 061207 (2003).
 - [49] H. Tammet, "Size and mobility of nanometer particles, clusters and ions," *J. Aerosol. Sci.* **26**, 459 (1995).
 - [50] D. Drosdoff, A. Widom, and Y. Srivastava, "Quantum drag forces on a sphere moving through a rarefied gas," *Phys. Rev. E* **71**, 051202 (2005).
 - [51] T. R. Marrero and E. A. Mason, "Gaseous diffusion coefficients," *jpocrd* **1**, 3 (1972).
 - [52] F. L. Wiseman, "An expression for the drag force of small spherical particles in an ideal-gas media analyzed using configuration-specific kinetic molecular theory," *Chem. Phys. Lett.* **465**, 175 (2008).
 - [53] C. Liu and H. Wang, "Nanoparticles in dilute gases: Fundamental equivalence between momentum accommodation and surface adsorption," *Phys. Rev. E* **99**, 042127 (2019).
 - [54] Z. Li and H. Wang, "Gas-nanoparticle scattering: A molecular view of momentum accommodation function," *Phys. Rev. Lett.* **95**, 014502 (2005).
 - [55] H. Wang, "Transport properties of small spherical particles," *Ann. N.Y. Acad. Sci.* **1161**, 484 (2009).
 - [56] Z. Li and H. Wang, "Thermophoretic force and velocity of nanoparticles in the free molecule regime," *Phys. Rev. E* **70**, 021205 (2004).
-

-
- [57] J. Wang and Z. Li, "Thermophoretic force on micro- and nanoparticles in dilute binary gas mixtures," *Phys. Rev. E* **84**, 021201 (2011).
- [58] I. S. Akhatov, J. M. Hoey, O. F. Swenson, and D. L. Schulz, "Aerosol flow through a long micro-capillary: collimated aerosol beam," *Microfluid. Nanofluid.* **5**, 215 (2007).
- [59] N. Liu and D. B. Bogy, "Forces on a spherical particle with an arbitrary axis of rotation in a weak shear flow of a highly rarefied gas," *Phys. Fluids* **21**, 047102 (2009).
- [60] I. Akhatov, J. Hoey, O. Swenson, and D. Schulz, "Aerosol focusing in micro-capillaries: Theory and experiment," *J. Aerosol. Sci.* **39**, 691 (2008).
- [61] D. S. Lemons and A. Gythiel, "Paul Langevin's 1908 paper "On the theory of Brownian motion"," *Am. J. Phys.* **65**, 1079 (1997), translation of "Sur la théorie du mouvement brownien" in *C. R. Acad. Sci. (Paris)* **146**, 530–533 (1908).
- [62] (), cOMSOL Multiphysics v. 5.3. <http://www.comsol.com>. COMSOL AB, Stockholm, Sweden.
- [63] J. Küpper, S. Stern, L. Holmegaard, F. Filsinger, A. Rouzée, A. Rudenko, P. Johnsson, A. V. Martin, M. Adolph, A. Aquila, S. Bajt, A. Barty, C. Bostedt, J. Bozek, C. Caleman, R. Coffee, N. Coppola, T. Delmas, S. Epp, B. Erk, L. Foucar, T. Gorkhover, L. Gumprecht, A. Hartmann, R. Hartmann, G. Hauser, P. Holl, A. Hömke, N. Kimmel, F. Krasniqi, K.-U. Kühnel, J. Maurer, M. Messerschmidt, R. Moshhammer, C. Reich, B. Rudek, R. Santra, I. Schlichting, C. Schmidt, S. Schorb, J. Schulz, H. Soltau, J. C. H. Spence, D. Starodub, L. Strüder, J. Thøgersen, M. J. J. Vrakking, G. Weidenspointner, T. A. White, C. Wunderer, G. Meijer, J. Ullrich, H. Stapelfeldt, D. Rolles, and H. N. Chapman, "X-ray diffraction from isolated and strongly aligned gas-phase molecules with a free-electron laser," *Phys. Rev. Lett.* **112**, 083002 (2014), arXiv:1307.4577 [physics].
- [64] J. C. H. Spence and H. N. Chapman, "The birth of a new field," *Phil. Trans. R. Soc. B* **369**, 20130309 (2014).
- [65] K. Pande, C. D. M. Hutchison, G. Groenhof, A. Aquila, J. S. Robinson, J. Tenboer, S. Basu, S. Boutet, D. P. DePonte, M. Liang, T. A. White, N. A. Zatsepin, O. Yefanov, D. Morozov, D. Oberthuer, C. Gati, G. Subramanian, D. James, Y. Zhao, J. Koralek, J. Brayshaw, C. Kupitz, C. Conrad, S. Roy-Chowdhury, J. D. Coe, M. Metz, P. L. Xavier, T. D. Grant, J. E. Koglin, G. Ketawala, R. Fromme, V. Šrajer, R. Henning, J. C. H. Spence, A. Ourmazd, P. Schwander, U. Weierstall, M. Frank, P. Fromme, A. Barty, H. N. Chapman, K. Moffat, J. J. van Thor, and M. Schmidt, "Femtosecond structural dynamics drives the trans/cis isomerization in photoactive yellow protein," *Science* **352**, 725 (2016).
- [66] T. Gorkhover, S. Schorb, R. Coffee, M. Adolph, L. Foucar, D. Rupp, A. Aquila, J. D. Bozek, S. W. Epp, B. Erk, L. Gumprecht, L. Holmegaard, A. Hartmann, R. Hartmann, G. Hauser, P. Holl, A. Hömke, N. Kimmel, K.-U. Kühnel, P. Johnsson, M. Messerschmidt, C. Reich, A. Rouzée, B. Rudek, C. Schmidt, J. Schulz, H. Soltau, S. Stern, G. Weidenspointner, B. White, J. Küpper, L. Strüder, I. Schlichting, J. Ullrich, D. Rolles, A. Rudenko, T. Möller, and C. Bostedt, "Femtosecond and nanometre visualization of structural dynamics in superheated nanoparticles," *Nat. Photon.* **10**, 93–97 (2016).
-

- [67] J. M. Glowacki, A. Natan, J. P. Cryan, R. Hartsock, M. Kozina, M. P. Minitti, S. Nelson, J. Robinson, T. Sato, T. van Driel, G. Welch, C. Weninger, D. Zhu, and P. H. Bucksbaum, "Self-referenced coherent diffraction x-ray movie of ångstrom- and femtosecond-scale atomic motion," *Phys. Rev. Lett.* **117**, 153003 (2016), arXiv:1608.03039 [physics].
- [68] B. Ziaja, H. N. Chapman, R. Fäustlin, S. Hau-Riege, Z. Jurek, A. V. Martin, S. Toleikis, F. Wang, E. Weckert, and R. Santra, "Limitations of coherent diffractive imaging of single objects due to their damage by intense x-ray radiation," *New J. Phys.* **14**, 115015 (2012).
- [69] U. Lorenz, N. M. Kabachnik, E. Weckert, and I. A. Vartanyants, "Impact of ultrafast electronic damage in single-particle x-ray imaging experiments," *Phys. Rev. E* **86**, 051911 (2012), arXiv:1206.6960 [physics].
- [70] R. Fung, V. Shneerson, D. Saldin, and A. Ourmazd, "Structure from fleeting illumination of faint spinning objects in flight," *Nat. Phys.* **5**, 64 (2009).
- [71] M. M. Seibert, T. Ekeberg, F. R. N. C. Maia, M. Svenda, J. Andreasson, O. Jönsson, D. Odić, B. Iwan, A. Rocker, D. Westphal, M. Hantke, D. P. Deponte, A. Barty, J. Schulz, L. Gumprecht, N. Coppola, A. Aquila, M. Liang, T. A. White, A. Martin, C. Caleman, S. Stern, C. Abergel, V. Seltzer, J.-M. Claverie, C. Bostedt, J. D. Bozek, S. Boutet, A. A. Miahnahri, M. Messerschmidt, J. Krzywinski, G. Williams, K. O. Hodgson, M. J. Bogan, C. Y. Hampton, R. G. Sierra, D. Starodub, I. Andersson, S. Bajt, M. Barthelmeß, J. C. H. Spence, P. Fromme, U. Weierstall, R. Kirian, M. Hunter, R. B. Doak, S. Marchesini, S. P. Hau-Riege, M. Frank, R. L. Shoeman, L. Lomb, S. W. Epp, R. Hartmann, D. Rolles, A. Rudenko, C. Schmidt, L. Foucar, N. Kimmel, P. Holl, B. Rudek, B. Erk, A. Hömke, C. Reich, D. Pietschner, G. Weidenspointner, L. Strüder, G. Hauser, H. Gorke, J. Ullrich, I. Schlichting, S. Herrmann, G. Schaller, F. Schopper, H. Soltau, K.-U. Kühnel, R. Andritschke, C.-D. Schröter, F. Krasniqi, M. Bott, S. Schorb, D. Rupp, M. Adolph, T. Gorkhover, H. Hirsemann, G. Potdevin, H. Graafsma, B. Nilsson, H. N. Chapman, and J. Hajdu, "Single mimivirus particles intercepted and imaged with an X-ray laser," *Nature* **470**, 78 (2011).
- [72] R. Xu, H. Jiang, C. Song, J. A. Rodriguez, Z. Huang, C.-C. Chen, D. Nam, J. Park, M. Gallagher-Jones, S. Kim, S. Kim, A. Suzuki, Y. Takayama, T. Oroguchi, Y. Takahashi, J. Fan, Y. Zou, T. Hatsui, Y. Inubushi, T. Kameshima, K. Yonekura, K. Tono, T. Togashi, T. Sato, M. Yamamoto, M. Nakasako, M. Yabashi, T. Ishikawa, and J. Miao, "Single-shot three-dimensional structure determination of nanocrystals with femtosecond X-ray free-electron laser pulses," *Nat. Commun.* **5**, 4061 (2014).
- [73] T. Ekeberg, M. Svenda, C. Abergel, F. R. N. C. Maia, V. Seltzer, J.-M. Claverie, M. Hantke, O. Jönsson, C. Nettelblad, G. van der Schot, M. Liang, D. P. Deponte, A. Barty, M. M. Seibert, B. Iwan, I. Andersson, N. D. Loh, A. V. Martin, H. Chapman, C. Bostedt, J. D. Bozek, K. R. Ferguson, J. Krzywinski, S. W. Epp, D. Rolles, A. Rudenko, R. Hartmann, N. Kimmel, and J. Hajdu, "Three-dimensional reconstruction of the giant mimivirus particle with an x-ray free-electron laser," *Phys. Rev. Lett.* **114**, 098102 (2015).
- [74] H. N. Chapman, P. Fromme, A. Barty, T. A. White, R. A. Kirian, A. Aquila, M. S. Hunter, J. Schulz, D. P. Deponte, U. Weierstall, R. B. Doak, F. R. N. C. Maia, A. V. Martin, I. Schlichting, L. Lomb, N. Coppola, R. L. Shoeman, S. W. Epp, R. Hartmann, D. Rolles, A. Rudenko, L. Foucar, N. Kimmel, G. Weidenspointner, P. Holl, M. Liang,
-

- M. Barthelmess, C. Caleman, S. Boutet, M. J. Bogan, J. Krzywinski, C. Bostedt, S. Bajt, L. Gumprecht, B. Rudek, B. Erk, C. Schmidt, A. Hömke, C. Reich, D. Pietschner, L. Strüder, G. Hauser, H. Gorke, J. Ullrich, S. Herrmann, G. Schaller, F. Schopper, H. Soltau, K.-U. Kühnel, M. Messerschmidt, J. D. Bozek, S. P. Hau-Riege, M. Frank, C. Y. Hampton, R. G. Sierra, D. Starodub, G. J. Williams, J. Hajdu, N. Timneanu, M. M. Seibert, J. Andreasson, A. Rocker, O. Jönsson, M. Svenda, S. Stern, K. Nass, R. Andritschke, C.-D. Schröter, F. Krasniqi, M. Bott, K. E. Schmidt, X. Wang, I. Grotjohann, J. M. Holton, T. R. M. Barends, R. Neutze, S. Marchesini, R. Fromme, S. Schorb, D. Rupp, M. Adolph, T. Gorkhover, I. Andersson, H. Hirsemann, G. Potdevin, H. Graafsma, B. Nilsson, and J. C. H. Spence, "Femtosecond x-ray protein nanocrystallography," *Nature* **470**, 73 (2011).
- [75] I. Schlichting, "Serial femtosecond crystallography: the first five years," *IUCr* **2**, 246 (2015).
- [76] K. Ayyer, O. M. Yefanov, D. Oberthür, S. Roy-Chowdhury, L. Galli, V. Mariani, S. Basu, J. Coe, C. E. Conrad, R. Fromme, A. Schaffer, K. Dörner, D. James, C. Kupitz, M. Metz, G. Nelson, P. L. Xavier, K. R. Beyerlein, M. Schmidt, I. Sarrou, J. C. H. Spence, U. Weierstall, T. A. White, J.-H. Yang, Y. Zhao, M. Liang, A. Aquila, M. S. Hunter, J. S. Robinson, J. E. Koglin, S. Boutet, P. Fromme, A. Barty, and H. N. Chapman, "Macromolecular diffractive imaging using imperfect crystals," *Nature* **530**, 202 (2016).
- [77] S. Stern, L. Holmegaard, F. Filsinger, A. Rouzée, A. Rudenko, P. Johnsson, A. V. Martin, A. Barty, C. Bostedt, J. D. Bozek, R. N. Coffee, S. Epp, B. Erk, L. Foucar, R. Hartmann, N. Kimmel, K.-U. Kühnel, J. Maurer, M. Messerschmidt, B. Rudek, D. G. Starodub, J. Thøgersen, G. Weidenspointner, T. A. White, H. Stapelfeldt, D. Rolles, H. N. Chapman, and J. Küpper, "Toward atomic resolution diffractive imaging of isolated molecules with x-ray free-electron lasers," *Faraday Disc.* **171**, 393 (2014), arXiv:1403.2553 [physics] .
- [78] G. Golovin, S. Banerjee, J. Zhang, S. Chen, C. Liu, B. Zhao, J. Mills, K. Brown, C. Petersen, and D. Umstadter, "Tomographic imaging of nonsymmetric multicomponent tailored supersonic flows from structured gas nozzles," *Appl. Opt.* **54**, 3491 (2015).
- [79] B. Landgraf, M. Schnell, A. Sävert, M. C. Kaluza, and C. Spielmann, "High resolution 3D gas-jet characterization," *Rev. Sci. Instrum.* **82**, 083106 (2011).
- [80] L. Strüder, S. Epp, D. Rolles, R. Hartmann, P. Holl, G. Lutz, H. Soltau, R. Eckart, C. Reich, K. Heinzinger, C. Thamm, A. Rudenko, F. Krasniqi, K. Kühnel, C. Bauer, C.-D. Schroeter, R. Moshhammer, S. Techert, D. Miessner, M. Porro, O. Haelker, N. Meidinger, N. Kimmel, R. Andritschke, F. Schopper, G. Weidenspointner, A. Ziegler, D. Pietschner, S. Herrmann, U. Pietsch, A. Walenta, W. Leitenberger, C. Bostedt, T. Moeller, D. Rupp, M. Adolph, H. Graafsma, H. Hirsemann, K. Gaertner, R. Richter, L. Foucar, R. L. Shoeman, I. Schlichting, and J. Ullrich, "Large-format, high-speed, x-ray pncdcs combined with electron and ion imaging spectrometers in a multipurpose chamber for experiments at 4th generation light sources," *Nucl. Instrum. Meth. A* **614**, 483 (2010).
- [81] F. Filsinger, G. Meijer, H. Stapelfeldt, H. Chapman, and J. Küpper, "State- and conformer-selected beams of aligned and oriented molecules for ultrafast diffraction studies," *Phys. Chem. Chem. Phys.* **13**, 2076 (2011), arXiv:1009.0871 [physics] .
-

- [82] Y.-P. Chang, D. A. Horke, S. Trippel, and J. Küpper, "Spatially-controlled complex molecules and their applications," *Int. Rev. Phys. Chem.* **34**, 557 (2015), arXiv:1505.05632 [physics] .
- [83] M. J. Bogan, S. Boutet, H. N. Chapman, S. Marchesini, A. Barty, W. H. Benner, U. Rohner, M. Frank, S. P. Hau-Riege, S. Bajt, B. Woods, M. M. Seibert, B. Iwan, N. Timneanu, J. Hajdu, and J. Schulz, "Aerosol imaging with a soft x-ray free electron laser," *Aerosol Sci. Techn.* **44**, i (2010).
- [84] D. K. Hutchins, M. H. Harper, and R. L. Felder, "Slip correction measurements for solid spherical particles by modulated dynamic light scattering," *Aerosol Sci. Techn.* **22**, 202 (1995).
- [85] A. Li and G. Ahmadi, "Dispersion and deposition of spherical particles from point sources in a turbulent channel flow," *Aerosol Sci. Techn.* **16**, 209 (1992).
- [86] K. R. Beyerlein, L. Adriano, M. Heymann, R. Kirian, J. Knoska, F. Wilde, H. N. Chapman, and S. Bajt, "Ceramic micro-injection molded nozzles for serial femtosecond crystallography sample delivery," *Rev. Sci. Instrum.* **86**, 125104 (2015).
- [87] J. Bielecki, private communication (2017).
- [88] G. A. Petrucci, P. B. Farnsworth, P. Cavalli, and N. Omenetto, "A differentially pumped particle inlet for sampling of atmospheric aerosols into a time-of-flight mass spectrometer: Optical characterization of the particle beam," *Aerosol Sci. Techn.* **33**, 105 (2000).
- [89] J. M. Headrick, P. E. Schrader, and H. A. Michelsen, "Radial-profile and divergence measurements of combustion-generated soot focused by an aerodynamic-lens system," *J. Aerosol. Sci.* **58**, 158 (2013).
- [90] D. A. Horke, N. Roth, L. Worbs, and J. Küpper, "Characterizing gas flow from aerosol particle injectors," *J. Appl. Phys.* **121**, 123106 (2017), arXiv:1609.09020 [physics] .
- [91] F. Filsinger, U. Erlekam, G. von Helden, J. Küpper, and G. Meijer, "Selector for structural isomers of neutral molecules," *Phys. Rev. Lett.* **100**, 133003 (2008), arXiv:0802.2795 [physics] .
- [92] K. Ayyer, A. J. Morgan, A. Aquila, H. DeMirici, B. G. Hogue, R. A. Kirian, P. L. Xavier, C. H. Yoon, H. N. Chapman, and A. Barty, "Low-signal limit of x-ray single particle diffractive imaging," *Opt. Exp.* **27**, 37816 (2019).
- [93] K. Ayyer, P. L. Xavier, J. Bielecki, Z. Shen, B. J. Daurer, A. K. Samanta, S. Awel, R. Bean, A. Barty, M. Bergemann, T. Ekeberg, A. D. Estillore, H. Fangohr, K. Giewekemeyer, M. S. Hunter, M. Karnevskiy, R. A. Kirian, H. Kirkwood, Y. Kim, J. Koliyadu, H. Lange, R. Letrun, J. Lübke, T. Michelat, A. J. Morgan, N. Roth, T. Sato, M. Sikorski, F. Schulz, J. C. H. Spence, P. Vagovic, T. Wollweber, L. Worbs, O. Yefanov, Y. Zhuang, F. R. N. C. Maia, D. A. Horke, J. Küpper, N. D. Loh, A. P. Mancuso, and H. N. Chapman, "3D diffractive imaging of nanoparticle ensembles using an x-ray laser," *Optica* **8**, 15 (2021), arXiv:2007.13597 [physics] .
- [94] N. Roth, S. Awel, D. A. Horke, and J. Küpper, "Optimizing aerodynamic lenses for single-particle imaging," *J. Aerosol. Sci.* **124**, 17 (2018), arXiv:1712.01795 [physics] .
-

-
- [95] B. Erk, J. P. Müller, C. Bomme, R. Boll, G. Brenner, H. N. Chapman, J. Correa, S. Düsterer, S. Dziarzhytski, S. Eisebitt, H. Graafsma, S. Grunewald, L. Gumprecht, R. Hartmann, G. Hauser, B. Keitel, C. von Korff Schmising, M. Kuhlmann, B. Manschwetus, L. Mercadier, E. Müller, C. Passow, E. Plönjes, D. Ramm, D. Rompotis, A. Rudenko, D. Rupp, M. Sauppe, F. Siewert, D. Schlosser, L. Strüder, A. Swiderski, S. Techert, K. Tiedtke, T. Tilp, R. Treusch, I. Schlichting, J. Ullrich, R. Moshhammer, T. Möller, and D. Rolles, "CAMP@FLASH: an end-station for imaging, electron- and ion-spectroscopy, and pump-probe experiments at the flash free-electron laser," *J. Synchrotron Rad.* **25**, 1529 (2018).
- [96] J. Feldhaus, "FLASH – the first soft x-ray free electron laser (FEL) user facility," *J. Phys. B* **43**, 194002 (2010).
- [97] M. O. Wiedorn, S. Awel, A. J. Morgan, M. Barthelmess, R. Bean, K. R. Beyerlein, L. M. G. Chavas, N. Eckerskorn, H. Fleckenstein, M. Heymann, D. A. Horke, J. Knoška, V. Mariani, D. Oberthür, N. Roth, O. Yefanov, A. Barty, S. Bajt, J. Küpper, A. V. Rode, R. A. Kirian, and H. N. Chapman, "Post-sample aperture for low background diffraction experiments at x-ray free-electron lasers," *J. Synchrotron Rad.* **24**, 1296 (2017).
- [98] S. Prahl, "miepython," Website, URL: <https://github.com/scottprahl/miepython> (2019), accessed on 2019-10-05.
- [99] A. Thompson, I. Lindau, D. Attwood, Y. Liu, E. Gullikson, P. Pianetta, M. Howells, A. Robinson, K.-J. Kim, J. Scofield, J. Kirz, J. Underwood, J. Kortright, G. Williams, and H. Winick, *X-Ray Data Booklet* (Center for X-Ray Optics and Advanced Light Source, Lawrence Berkeley National Laboratory, Berkeley, CA, 2009).
- [100] L. Worbs, N. Roth, J. Lübke, A. Estillore, P. L. Xavier, A. K. Samanta, and J. Küpper, "Optimizing the geometry of nanoparticle injectors," (2020), in preparation.
- [101] D. Raoult and P. Forterre, "Redefining viruses: lessons from Mimivirus," *Nat. Rev. Microbiol.* **6**, 315 (2008).
- [102] H. Shen, Q. Gao, Y. Zhang, Y. Lin, Q. Lin, Z. Li, L. Chen, Z. Zeng, X. Li, Y. Jia, S. Wang, Z. Du, L. S. Li, and Z. Zhang, "Visible quantum dot light-emitting diodes with simultaneous high brightness and efficiency," *Nat. Photon.* **13**, 192 (2019).
- [103] G. Bao, S. Mitragotri, and S. Tong, "Multifunctional nanoparticles for drug delivery and molecular imaging," *Annu. Rev. Biomed. Eng.* **15**, 253 (2013).
- [104] A. Hosseinizadeh, G. Mashayekhi, J. Copperman, P. Schwander, A. Dashti, S. Sepehr, R. Fung, M. Schmidt, C. H. Yoon, B. G. Hogue, G. J. Williams, A. Aquila, and A. Ourmazd, "Conformational landscape of a virus by single-particle x-ray scattering," *Nat. Meth.* **14**, 877 (2017).
- [105] R. Fernandez and S. H. W. Scheres, "Unravelling biological macromolecules with cryo-electron microscopy," *Nature* **537**, 339 (2016).
- [106] Y. Sugita, H. Matsunami, Y. Kawaoka, T. Noda, and M. Wolf, "Cryo-em structure of the ebola virus nucleoprotein-rna complex at 3.6 Å resolution," *Nature* **563**, 137 (2018).
-

-
- [107] I. Drulyte, R. M. Johnson, E. L. Hesketh, D. L. Hurdiss, C. A. Scraff, S. A. Porav, N. A. Ranson, S. P. Muench, and R. F. Thompson, "Approaches to altering particle distributions in cryo-electron microscopy sample preparation," *Acta Cryst.* **74**, 560 (2018).
- [108] V. Singh, A. K. Samanta, N. Roth, D. Gusa, T. Ossenbrüggen, I. Rubinsky, D. A. Horke, and J. Küpper, "Optimized cell geometry for buffer-gas-cooled molecular-beam sources," *Phys. Rev. A* **97**, 032704 (2018), arXiv:1801.10586 [physics] .
- [109] N. Teschmit, D. A. Horke, and J. Küpper, "Spatially separating the conformers of a dipeptide," *Angew. Chem. Int. Ed.* **57**, 13775 (2018), arXiv:1805.12396 [physics] .
- [110] G. von Helden, T. Wyttenbach, and M. T. Bowers, "Conformation of macromolecules in the gas-phase: Use of matrix-assisted laser desorption methods in ion chromatography," *Science* **267**, 1483 (1995).
- [111] F. Lanucara, S. W. Holman, C. J. Gray, and C. E. Eyers, "The power of ion mobility-mass spectrometry for structural characterization and the study of conformational dynamics," *Nat. Chem.* **6**, 281 (2014).
- [112] J. C. H. Spence and R. B. Doak, "Single molecule diffraction," *Phys. Rev. Lett.* **92**, 198102 (2004).
- [113] L. Holmegaard, J. H. Nielsen, I. Nevo, H. Stapelfeldt, F. Filsinger, J. Küpper, and G. Meijer, "Laser-induced alignment and orientation of quantum-state-selected large molecules," *Phys. Rev. Lett.* **102**, 023001 (2009), arXiv:0810.2307 [physics] .
- [114] N. Eckerskorn, R. Bowman, R. A. Kirian, S. Awel, M. Wiedorn, J. Küpper, M. J. Padgett, H. N. Chapman, and A. V. Rode, "Optically induced forces imposed in an optical funnel on a stream of particles in air or vacuum," *Phys. Rev. Appl.* **4**, 064001 (2015).
- [115] Z. Li, L. Shi, L. Cao, Z. Liu, and J. Küpper, "Acoustic funnel and buncher for nanoparticle injection," *Phys. Rev. Appl.* **11**, 064036 (2019), arXiv:1803.07472 [physics] .
- [116] N. R. Hutzler, H.-I. Lu, and J. M. Doyle, "The buffer gas beam: An intense, cold, and slow source for atoms and molecules," *Chem. Rev.* **112**, 4803 (2012), arXiv:1111.2841 [physics] .
- [117] J. Piskorski, D. Patterson, S. Eibenberger, and J. M. Doyle, "Cooling, spectroscopy and non-sticking of trans-stilbene and Nile Red," *Chem. Phys. Chem.* **15**, 3800 (2014).
- [118] M. Z. Kamrath and T. R. Rizzo, "Combining ion mobility and cryogenic spectroscopy for structural and analytical studies of biomolecular ions," *Acc. Chem. Res.* **51**, 1487 (2018).
- [119] C. Gati, D. Oberthuer, O. Yefanov, R. D. Bunker, F. Stellato, E. Chiu, S.-M. Yeh, A. Aquila, S. Basu, R. Bean, K. R. Beyerlein, S. Botha, S. Boutet, D. P. DePonte, R. B. Doak, R. Fromme, L. Galli, I. Grotjohann, D. R. James, C. Kupitz, L. Lomb, M. Messerschmidt, K. Nass, K. Rendek, R. L. Shoeman, D. Wang, U. Weierstall, T. A. White, G. J. Williams, N. A. Zatsepin, P. Fromme, J. C. H. Spence, K. N. Goldie, J. A. Jehle, P. Metcalf, A. Barty, and H. N. Chapman, "Atomic structure of granulins determined from native nanocrystalline granulovirus using an x-ray free-electron laser," *Proc. Natl. Acad. Sci. U.S.A.* **114**, 2247 (2017), <http://www.pnas.org/content/114/9/2247.full.pdf> .
-

-
- [120] (), cOMSOL Multiphysics v. 5.5. <http://www.comsol.com>. COMSOL AB, Stockholm, Sweden.
- [121] P. Virtanen, R. Gommers, T. E. Oliphant, M. Haberland, T. Reddy, D. Cournapeau, E. Burovski, P. Peterson, W. Weckesser, J. Bright, S. J. van der Walt, M. Brett, J. Wilson, K. Jarrod Millman, N. Mayorov, A. R. J. Nelson, E. Jones, R. Kern, E. Larson, C. Carey, Í. Polat, Y. Feng, E. W. Moore, J. VanderPlas, D. Laxalde, J. Perktold, R. Cimrman, I. Henriksen, E. A. Quintero, C. R. Harris, A. M. Archibald, A. H. Ribeiro, F. Pedregosa, P. van Mulbregt, and SciPy 1.0 Contributors, "SciPy 1.0: fundamental algorithms for scientific computing in Python," *Nat. Meth.* **17**, 261 (2020).
- [122] S. Whitaker, "Forced convection heat transfer correlations for flow in pipes, past flat pipes, single cylinders, single spheres, and for flow in packed beds and tube bundles," *AIChE J.* **18**, 361 (1972).
- [123] L. L. Kavanau and J. R. M. Drake, "Heat transfer from spheres to a rarefied gas in subsonic flow," *Trans. ASME* **77**, 617 (1955).
- [124] S. C. Garrick, K. E. J. Lehtinen, and M. R. Zachariah, "Nanoparticle coagulation via a navier-stokes/nodal methodology: Evolution of the particle field," *J. Aerosol. Sci.* **37**, 555 (2006).
- [125] M. O. Wiedorn, D. Oberthür, R. Bean, R. Schubert, N. Werner, B. Abbey, M. Aepfelbacher, L. Adriano, A. Allahgholi, N. Al-Qudami, J. Andreasson, S. Aplin, S. Awel, K. Ayyer, S. Bajt, I. Barák, S. Bari, J. Bielecki, S. Botha, D. Boukhelef, W. Brehm, S. Brockhauser, I. Cheviakov, M. A. Coleman, F. Cruz-Mazo, C. Danilevski, C. Darmanin, R. B. Doak, M. Domaracky, K. Dörner, Y. Du, H. Fangohr, H. Fleckenstein, M. Frank, P. Fromme, A. M. Gañán Calvo, Y. Gevorkov, K. Giewekemeyer, H. M. Ginn, H. Graafsma, R. Graceffa, D. Greiffenberg, L. Gumprecht, P. Göttlicher, J. Hajdu, S. Hauf, M. Heymann, S. Holmes, D. A. Horke, M. S. Hunter, S. Imlau, A. Kaukher, Y. Kim, A. Klyuev, J. Knoska, B. Kobe, M. Kuhn, C. Kupitz, J. Küpper, J. M. Lahey-Rudolph, T. Laurus, K. Le Cong, R. Letrun, P. L. Xavier, L. Maia, F. R. N. C. Maia, V. Mariani, M. Messerschmidt, M. Metz, D. Mezza, T. Michelat, G. Mills, D. C. F. Monteiro, A. Morgan, K. Mühligh, A. Munke, A. Münnich, J. Nette, K. A. Nugent, T. Nuguid, A. M. Orville, S. Pandey, G. Pena, P. Villanueva-Perez, J. Poehlsen, G. Previtali, L. Redecke, W. M. Riekehr, H. Rohde, A. Round, T. Safenreiter, I. Sarrou, T. Sato, M. Schmidt, B. Schmitt, R. Schönherr, J. Schulz, J. A. Sellberg, M. M. Seibert, C. Seuring, M. L. Shelby, R. L. Shoeman, M. Sikorski, A. Silenzi, C. A. Stan, X. Shi, S. Stern, J. Sztuk-Dambietz, J. Szuba, A. Tolstikova, M. Trebbin, U. Trunk, P. Vagovic, T. Ve, B. Weinhausen, T. A. White, K. Wrona, C. Xu, O. Yefanov, N. Zatsepin, J. Zhang, M. Perbandt, A. P. Mancuso, C. Betzel, H. N. Chapman, and A. Barty, "Megahertz serial crystallography," *Nat. Commun.* **9**, 4025 (2018).
- [126] J. Dubochet, M. Adrian, J.-J. Chang, J.-C. Homo, J. Lepault, A. W. McDowell, and P. Schultz, "Cryo-electron microscopy of vitrified specimens," *Q. Rev. Biophys.* **21**, 129 (1988).
- [127] W. F. Tivol, A. Briegel, and G. J. Jensen, "An improved cryogen for plunge freezing," *Microsc. Microanal.* **14**, 375 (2008).
- [128] M. M. Gebhardt, K. E. Eberle, P. Radtke, and J. A. Jehle, "Baculovirus resistance in codling moth is virus isolate-dependent and the consequence of a mutation in viral gene pe38," *PNAS* **111**, 15711 (2014).
-

- [129] H. Stapelfeldt and T. Seideman, "Colloquium: Aligning molecules with strong laser pulses," *Rev. Mod. Phys.* **75**, 543 (2003).
- [130] S. Trippel, M. Johny, T. Kierspel, J. Onvlee, H. Bieker, H. Ye, T. Mullins, L. Gumprecht, K. Długołęcki, and J. Küpper, "Knife edge skimming for improved separation of molecular species by the deflector," *Rev. Sci. Instrum.* **89**, 096110 (2018), arXiv:1802.04053 [physics].
- [131] S. Trippel, J. Wiese, T. Mullins, and J. Küpper, "Communication: Strong laser alignment of solvent-solute aggregates in the gas-phase," *J. Chem. Phys.* **148**, 101103 (2018), arXiv:1801.08789 [physics].
- [132] M. Amin, H. Samy, and J. Küpper, "Robust and accurate computational estimation of the polarizability tensors of macromolecules," *J. Phys. Chem. Lett.* **10**, 2938 (2019), arXiv:1904.02504 [physics].
- [133] M. N. Ali, J. Xiong, S. Flynn, J. Tao, Q. D. Gibson, L. M. Schoop, T. Liang, N. Hal-dolaarachchige, M. Hirschberger, N. P. Ong, and R. J. Cava, "Large, non-saturating magnetoresistance in WTe_2 ," *Nature* **514**, 205 (2014).
- [134] M. Mitrano, A. Cantaluppi, D. Nicoletti, S. Kaiser, A. Perucchi, S. Lupi, P. D. Pietro, D. Pontiroli, M. Riccò, S. R. Clark, D. Jaksch, and A. Cavalleri, "Possible light-induced superconductivity in K_3C_{60} at high temperature," *Nature* **530**, 461 (2016).
- [135] S. Eibenberger, S. Gerlich, M. Arndt, M. Mayor, and J. Tüxen, "Matter-wave interference of particles selected from a molecular library with masses exceeding 10 000 u," *Phys. Chem. Chem. Phys.* **15**, 14696 (2013).
- [136] E. Sobolev, S. Zolotarev, K. Giewekemeyer, J. Bielecki, K. Okamoto, H. K. N. Reddy, J. Andreasson, K. Ayyer, I. Barak, S. Bari, A. Barty, R. Bean, S. Bobkov, H. N. Chapman, G. Chojnowski, B. J. Daurer, K. Dörner, T. Ekeberg, L. Flückiger, O. Galzitskaya, L. Gelisio, S. Hauf, B. G. Hogue, D. A. Horke, A. Hosseinizadeh, V. Ilyin, C. Jung, C. Kim, Y. Kim, R. A. Kirian, H. Kirkwood, O. Kulyk, R. Letrun, D. Loh, M. Messerschmidt, K. Mühlig, A. Ourmazd, N. Raab, A. V. Rode, M. Rose, A. Round, T. Sato, R. Schubert, P. Schwander, J. A. Sellberg, M. Sikorski, A. Silenzi, C. Song, J. C. H. Spence, S. Stern, J. Sztuk-Dambietz, A. Teslyuk, N. Timneanu, M. Trebbin, C. Uetrecht, B. Weinhausen, G. J. Williams, P. L. Xavier, C. Xu, I. Vartanyants, V. Lamzin, A. Mancuso, and F. R. N. C. Maia, "Megahertz single-particle imaging at the European XFEL," *Comm. Phys* **3**, 97 (2020), arXiv:1912.10796 [physics].
- [137] J. Bielecki, M. F. Hantke, B. J. Daurer, H. K. N. Reddy, D. Hasse, D. S. D. Larsson, L. H. Gunn, M. Svenda, A. Munke, J. A. Sellberg, L. Flueckiger, A. Pietrini, C. Nettelblad, I. Lundholm, G. Carlsson, K. Okamoto, N. Timneanu, D. Westphal, O. Kulyk, A. Higashiura, G. van der Schot, N.-T. D. Loh, T. E. Wysong, C. Bostedt, T. Gorkhover, B. Iwan, M. M. Seibert, T. Osipov, P. Walter, P. Hart, M. Bucher, A. Ulmer, D. Ray, G. Carini, K. R. Ferguson, I. Andersson, J. Andreasson, J. Hajdu, and F. R. N. C. Maia, "Electrospray sample injection for single-particle imaging with x-ray lasers," *Science Advances* **5**, eaav8801 (2019).
- [138] A. K. Samanta, M. Amin, A. D. Estillore, N. Roth, L. Worbs, D. A. Horke, and J. Küpper, "Controlled beams of shockfrozen, isolated, biological and artificial nanoparticles," *Struct. Dyn.* **7**, 024304 (2020), arXiv:1910.12606 [physics].
-

- [139] G. A. Bird, *Molecular gas dynamics and the direct simulation of gas flows* (Clarendon Press, Oxford, UK, 1994).
- [140] G. G. Stokes, "On the effect of the internal friction of fluids on the motion of pendulums," *Trans. Cambridge Phil. Soc.* **9**, 8 (1851).
-

Acknowledgments

The work I did in the last years consists of much more than the scientific results I presented here. It was a journey in my life, that shaped me and which I will never forget. And as often in life it is the people I met and the people which accompanied me that allowed my scientific and personal growth. Of course I thank Jochen Küpper for the opportunity to graduate in his Controlled Molecule Imaging group in such a vivid and exiting research environment at the Center for Free-Electron Laser Science - CFEL and the Deutsches Elektronen-Synchrotron DESY. Jochen not only supervised me scientifically, but also influenced me as a person. I gained a lot of experience and confidence while working with him, was able to sharpen my scientific and computational skills and can state with proud that I have grown over the last years. And for that I am thankful. Every person in the CMI group contributed in one way or the other to this work and I want to thank all of them as well as all collaborators I worked with, especially the group of Henry Chapman. Within the CMI group my special thanks belong to the COMOTION team and its members throughout the years. It was fun and exciting working with you guys. I thank Daniel Horke for his very helpful supervision within my first years. He was always creating a positive and motivating working atmosphere, was a great team lead and his input increased my scientific writing capabilities a lot. Also he restored my believe, that well prepared and successful beam times are a matter of possibility. I thank Amit Kumar Samanta for the support especially in the last parts of this work, providing a lot of productive scientific feedback and always answered late night last minute questions. A lot of thanks also belong to Jannik Lübke and Lena Worbs for bringing fresh blood and fun to the team. You overtaking inferior work such as writing blog posts made me feel like a true senior. I thank Salah Awel, especially in the first years I learnt everything I know about aerosol injection from him and I still have the impression he is full of hidden knowledge. Working with you was always a pleasure and even long beam time shifts were not able to change that. Daniel Gusa, Helen Bieker, Joss Wiese, Pau González Caminal and Thomas Kierspel helped me with scientific discussions and provided additional point of views for my work, when thinking out of the box was necessary. Also these guys made sure that the work did not feel like it. In this context I want to thank especially Joss and Helen. Our two hour plus lunch breaks were an important ingredient for me to persist my positive attitude and to stay productive. Helen with you I learned, that it is possible to be motivated, while being unmotivated as long as you are not alone with it. Thank you for that. My final thanks belong to my family and here I have to name my wife Verena Roth. You always encouraged me and made me stay on track. Being with you is the home I need to switch off and recover. With you at my side I can tackle any challenge in my life.

Eidesstattliche Versicherung / Declaration on oath

Hiermit versichere ich an Eides statt, die vorliegende Dissertationschrift selbst verfasst und keine anderen als die angegebenen Hilfsmittel und Quellen benutzt zu haben.

Die eingereichte schriftliche Fassung entspricht der auf dem elektronischen Speichermedium.

Die Dissertation wurde in der vorgelegten oder einer ähnlichen Form nicht schon einmal in einem früheren Promotionsverfahren angenommen oder als ungenügend beurteilt.

Hamburg, den _____ Unterschrift: _____
Nils Roth